Dynamic wake meandering modeling

Larsen, Gunner Chr.; Aagaard Madsen , Helge; Bingöl, Ferhat; Mann, Jakob; Ott, Søren; Sørensen, J.N.; Okulov, V.; Troldborg, N.; Nielsen, Morten; Thomsen, Kenneth; Larsen, Torben J.; Mikkelsen, R.

Publication date:
2007

Document Version
Publisher's PDF, also known as Version of record

RISØ

Dynamic wake meandering modeling

Gunner C. Larsen, Helge Aa. Madsen, Ferhat Bingöl, Jakob Mann, Søren Ott, Jens N. Sørensen, Valery Okulov, Niels Troldborg, Morten Nielsen, Kenneth Thomsen, Torben J. Larsen, and Robert Mikkelsen

Risø-R-1607(EN)

Risø National Laboratory
Technical University of Denmark
Roskilde, Denmark
June 2007

DTU

Risø-R-Report

Author: Gunner C. Larsen, Helge Aa. Madsen, Ferhat Bingöl, Jakob Mann, Søren Ott, Jens N. Sørensen, Valery Okulov, Niels Troldborg, Morten Nielsen, Kenneth Thomsen, Torben J. Larsen, and Robert Mikkelsen,
Title: Dynamic wake meandering modeling
Department: Wind Energy Department

Abstract (max. 2000 char.): We present a consistent, physically based theory for the wake meandering phenomenon, which we consider of crucial importance for the overall description of wind turbine loadings in wind farms. In its present version the model is confined to single wake situations. The model philosophy does, however, have the potential to include also mutual wake interaction phenomenons.

The basic conjecture behind the dynamic wake meandering model is that wake transportation in the atmospheric boundary layer is driven by the large scale lateral- and vertical turbulence components. Based on this conjecture a stochastic model of the downstream *wake meandering* is formulated. In addition to the kinematic formulation of the dynamics of the "meandering frame of reference", models characterizing the *mean wake deficit* as well as the *added wake turbulence*, described in the meandering frame of reference, are an integrated part the model complex. For design applications, the computational efficiency of wake deficit prediction is a key issue. Two computationally low cost models are developed for this purpose. The character of the added wake turbulence, generated by the up-stream turbine in the form of shed and trailed vorticity, has been approached by analytical as well as by numerical studies.

The dynamic wake meandering philosophy has been verified by comparing model predictions with extensive full-scale measurements. These comparisons have demonstrated good agreement, both qualitatively and quantitatively, concerning both flow characteristics and turbine load characteristics.

Contrary to previous attempts to model wake loading, the dynamic wake meandering approach opens for a *unifying* description in the sense that turbine power– and load aspects can be treated simultaneously. This capability is a direct and attractive consequence of the model being based on the underlying physical process, and it potentially opens for *optimization* of wind farm topology, of wind farm operation as well as of control strategies for the individual turbine.

Implementation of the methodology with aeroelastic codes is straight forward and performed simply by replacing traditional turbulence input files with wind field files containing the combined effect of atmospheric turbulence and wake meandering.

Risø-R-1607(EN)
June 2007

ISSN 0106-2840
ISBN 978-87-550-3602-4

Contract no.:
ENS 33030-0004.

Group's own reg. no.:
1110045-01

Sponsorship:
Energistyrelsen
Amaliegade 44
1256 København K

Cover :

Pages: 84
Tables: 3
References: 83

Information Service Department
Risø National Laboratory
Technical University of Denmark
P.O.Box 49
DK-4000 Roskilde
Denmark
Telephone +45 46774004
bibl@risoe.dk
Fax +45 46774013
www.risoe.dk

Contents

Preface

This report constitutes a summary reporting of the EFP project entitled “Dynamic wake model for detailed aeroelastic simulation of turbines in wind farms”; J. nr. 33030-0004. In addition to the present summary report, the project has resulted in a large number of publications in journals and proceedings as well as in report form. References to these publications are given in the summary report to guide the reader to more detailed information on the subjects described in this report. Moreover a full list of the publications resulting from the project is supplied at the end of the report.

1 Introduction

The motivation for the study of wind turbine wakes is that wind turbines located in wind farms experience a wind field that is substantially modified compared to the ambient wind field that apply for stand-alone wind turbines. This drastic change of the environmental conditions has implications not only for the power production of a wind farm, but also for the loading conditions. Whereas previous attempts to describe the effects associated with wind farm siting typically has focused *either* on production aspects *or* on loading aspects, the model developed in this project offers a *unifying* approach covering both aspects within the same model. This attractive capability is a direct consequence of the model, contrary to alternative models, being based on the underlying physical processes, and thereby also potentially opens for *optimization* of wind farm topology, of wind farm operation as well as of control strategies for the individual turbine.

Apart from producing reliable results, that reflects the environmental reality for a wind turbine sited in wind farm conditions, the developed wake wind field model is straight forward to interface with existing state-of-the-art aeroelastic simulation packages. This feature substantially eases the deployment/dissemination of the obtained results into the wind turbine community.

Basically, the activities within the project fall in two phases. Phase 1 encompasses model development, whereas phase 2 deals with verification of the resulting model. The structure of the present report reflects this split in activities. The first part of the report is devoted to a description of the modeling efforts, whereas the setup and subsequent analysis of conducted experimental activities are described in the second part.

The *modeling part* encompasses descriptions of a stochastic wake meandering model, two (computationally low cost) models of quasi-steady wake deficits, a model of tip vortex instability, CFD based analyses of wake turbulence issues described in the wake moving frame of reference, and associated algorithms for generation of (wake) turbulence with inhomogeneous and in-stationary characteristics.

The *experimental part* includes detailed description of a dedicated full-scale experimental activity, primary aiming at verifying the basic conjecture behind the stochastic wake meandering model, as well as various analyses of wake data, arising from a full-scale measuring campaign conducted in a different context, with the aspects considered ranging from wake wind field characteristics to wake loading characteristics.

2 Modeling

Wind turbines located in wind farms experience a wind field that is modified compared to the ambient wind field. This modification is caused by the presence of upstream turbines that "emit" wakes that significantly modify the downstream wind field properties compared to the undisturbed ambient wind field.

A *wake* is characterized by a mean wind decrease (i.e. wake deficit) and turbulence increase behind a turbine. The downstream advection of a wake from the emitting turbine describes a stochastic pattern known as *wake meandering*. It appears as an *intermittent phenomenon*, where winds at downwind positions may be undisturbed for part of the time, but interrupted by episodes of intense turbulence and reduced mean velocity as the wake hits the observation point. Although different in nature compared to traditional turbulence, the resulting wind field may be considered as a turbulence field with intermittent characteristics, with a significantly modified turbulence *structure* and with increased "apparent" turbulence *intensity*. The notation "apparent" turbulence intensity indicates that the turbulence intensity contains contribution from both traditionally generated turbulence and from the wind speed variation caused by the instantaneous transversal- and vertical movements of the wake "emitted" from the upstream turbine.

A correct wind turbine load prediction requires both turbulence *intensity* and turbulence *structure* correctly described which is ensured by the Dynamic Wake Meandering (DWM) model complex resulting from this project. The approach taken in this model is believed to capture the essential physics of the wake problem, and it is completely different from traditional more empirically oriented approaches. Because the essential physics is captured, both load- and production aspects can be predicted, which is contrary to the traditional methods that typically focus on *either* load- *or* power prediction. As a consequence the proposed formulation opens for *optimization* of wind farm topology, of wind farm operation, as well as of control strategies for the individual turbine.

The philosophy behind the DWM model is schematically illustrated in Figure 2-1.

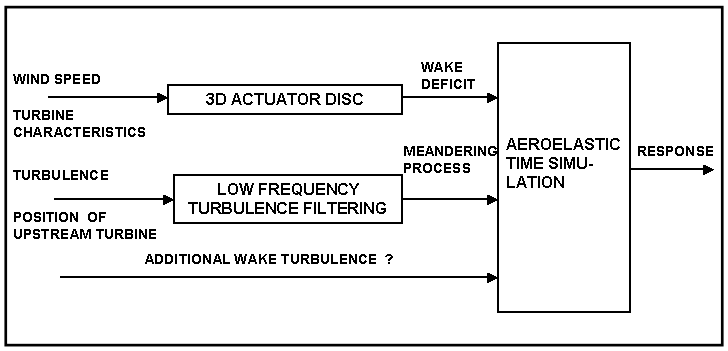

Figure 2-1 The main elements in the DWM model. From [8].

The *fundamental conjecture* behind the DWM approach is that the transport of a wake in the atmospheric boundary layer can be modeled, as if the wake acts as a passive tracer driven by the large-scale turbulence structures in the atmospheric boundary layer. This conjecture will be studied in detail in the experimental part of this report, and it will turn out to be in close agreement with full-scale experimental observations.

The approach described by the conjecture results in the need for modeling of the quasi-steady wake deficits, the wake meandering processes, and the turbulence effects caused by a wind turbine rotor. The *quasi-steady wake deficit* is the wake deficit formulated in the moving (meandering) frame of reference, and it includes the wake expansion as function of downstream transportation time caused partly by turbulence diffusion and partly by the rotor pressure field. The *wake meandering model* describes the stochastic downstream transport of the upstream emitted wakes by large scale turbulence structures, which are assumed not to be significantly affected by the presence a wind turbine. The *turbulence effects* caused by an upstream located turbine concern small-scale turbulence with characteristic eddy seizes up to approximately one rotor diameter, and include contributions from conventional mechanically generated turbulence, caused by the wake shear, as well as from the blade bound vorticity, consisting mainly of tip and root vortices. The tip vortices will initially take the form of organized coherent flow structures, but later, due to instability phenomenons, gradually break down and approach the characteristics of conventional isotropic turbulence with a length scale shorter than that of atmospheric turbulence.

The structure of the modeling part in this report closely reflects the above defined model categories. It thus contains three sub-sections on the modeling of (quasi-steady) wake deficits, wake meandering and wake turbulence effects, respectively.

2.1 Wake deficits

The wake deficits are caused by extraction of axial momentum by the upstream turbine(s). Close to the upstream turbine (i.e. the near wake region) the pressure field around the turbine is important for the development of the wake deficit but further downstream, the turbulent mixing caused by the velocity gradients of the deficit itself is the main driver for development of the deficit.

In the first implementations of the DWM model, the deficits have been computed with an CFD based actuator disc model coupled to an aeroelastic model of the rotor [28]. However, in the present context computational efficiency is a key issue for the modeling of quasi-steady wake deficits, because we are aiming at a fully integrated simulation of the deficits in the DWM framework. Therefore the original CFD approach has been replaced with more engineering types of models.

Two models, both characterized by very low computational costs, have been considered/developed – one based on the boundary layer equations, and the other based on a vorticity formulation. As a prelude to the treatment of these models, the computation of wake deficits as based on the actuator disc approach is summarized, because it is at present used to provide a requested initial wake deficit (i.e. a velocity deficit at some downstream distance close to the wake generating rotor) for the boundary layer approach. Then follows a description of the model for downstream development of the wake deficits based on the boundary layer equations, and finally the vorticity-based wake deficit model is outlined.

2.1.1 Wake deficits computed with an Actuator disc model

As described in [28] the aeroelastic model HAWC has been coupled with a 3-D actuator disc (AD) model. For specified operational conditions, the rotor loading is computed with HAWC, and then the load coefficients in the form of non-dimensional local thrust and torque coefficients are imported into the actuator disc model. The flow field corresponding to this loading is computed, and the flow field is then subsequently imported into the HAWC model. A new loading is computed, and a new computation with the actuator disc

model is performed. After a few iterations the loading and the flow field is in balance, and the actuator disc solution provides the whole flow field downstream of the turbine.

An example of computed deficits with this model is shown in Figure 2-2. In this case a constant loading, corresponding to a rotor thrust coefficient of 0.89, was applied. The strong variation in the deficit from the rotor disc and 1-2 rotor diameters downstream is due to the local pressure field around the rotor disc. Further downstream the variation of the deficits is much less and now mainly due to the turbulent mixing.

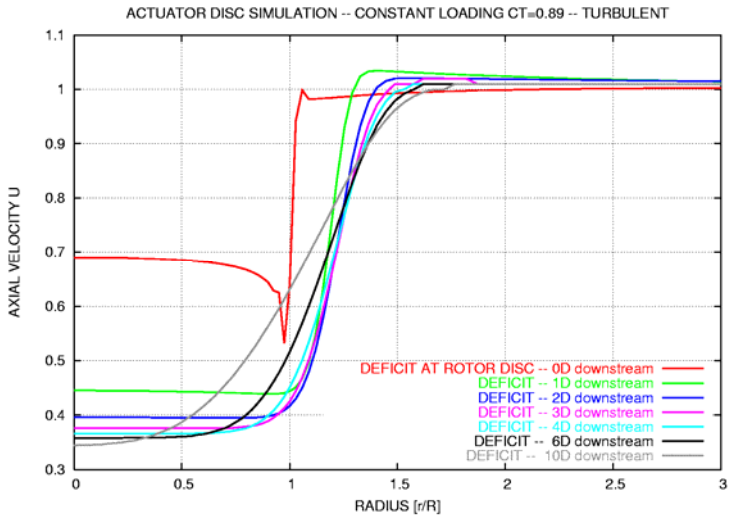

Figure 2-2 Computed wake deficit profiles in steady flow with an axi-symmetric actuator disc model using a $k-\varepsilon$ turbulence model. Constant loading with a thrust coefficient of 0.89.

Apart from illuminating the physical characteristics of the wake deficit, the AD model presently also provides the initial wake deficit requested by the boundary layer approach. In a later stage, this initial condition is planned to be provided by an adapted version of the much simpler blade element momentum (BEM) model.

2.1.2 Wake deficit model based on boundary layer equations

The present modeling is strongly inspired by the work of J.F. Ainsly who developed a similar wake model in the period from 1984 to 1988 [29], [30], and [31]. As noted above, turbulence mixing is the main driver for the wake deficit development, when we are outside the near wake region, and we can thus disregard the pressure terms in the Navier-Stokes equations. Further, the gradients of mean quantities are very much bigger in radial direction (denoted by r) than in the axial direction (denoted by x) which leads to the thin shear layer approximation of the Navier-Stokes equations. Assuming further steady and axi-symmetric flow we have the governing equation

$$U\frac{\partial U}{\partial x}+V\frac{\partial U}{\partial r}=-\left(\frac{1}{r}\right)\frac{\partial}{\partial r}\left(r\overline{uv}\right) \qquad (2\text{-}1)$$

where U and V denote the mean velocity in the axial- and radial directions, respectively, u and v denote the respective fluctuating velocity components in these directions, and an upper bar denotes temporal averaging.

Introducing the eddy viscosity concept, the Reynolds stresses are expressed as

$$-\overline{uv} = \upsilon_T \frac{\partial U}{\partial r} \ , \tag{2-2}$$

with the eddy viscosity given by

$$\upsilon_T(x) = l_m(x) U_m(x) \ , \tag{2-3}$$

where U_m and l_m are suitable velocity- and length scales of the turbulence that in general will vary with the downstream distance *x*, but assumed independent of the radial coordinate.

The length- and velocity scales are taken to be proportional to the instantaneous wake half width, *b*, and the velocity deficit difference, $U_0 - U_c$, across the shear layer, respectively, where U_0 and U_c denote the ambient velocity and the centre wake velocity. Introducing (2-2) into (2-1) the governing equation is reformulated as

$$U\frac{\partial U}{\partial x} + V\frac{\partial U}{\partial r} = \left(\frac{\upsilon_T}{r}\right)\frac{\partial}{\partial r}\left(r\frac{\partial U}{\partial r}\right) \ , \tag{2-4}$$

with

$$\upsilon_T = k_2 b\left(U_0 - U_c\right) \ , \tag{2-5}$$

where k_2 is a constant for the entire flow field.

In addition to the momentum equation (2-4) the flow must fulfill the continuity equation given by

$$\frac{1}{r}\frac{\partial}{\partial r}(rV) + \frac{\partial U}{\partial x} = 0 \ . \tag{2-6}$$

The flow problem defined by equations (2-4) and (2-6) are solved using a finite difference scheme.

In the following this model will be referred to as the BLE model, and a few results from initial tests of the model will be shown.

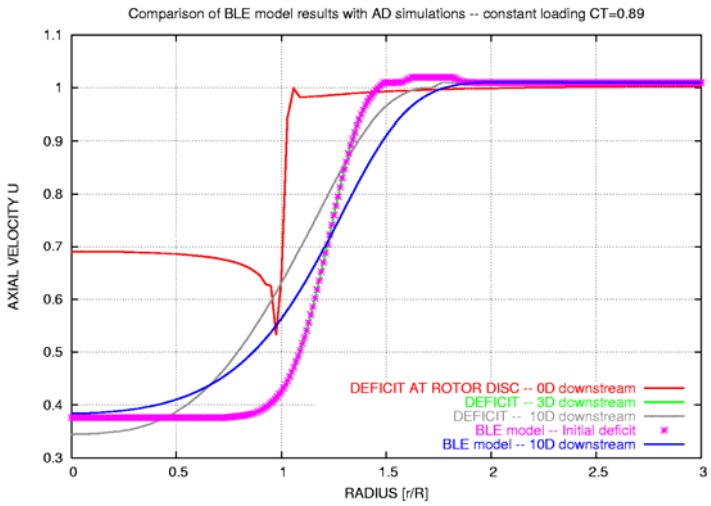

Figure 2-3 Comparison of the deficits computed by the AD and the BLE model respectively. The deficit at 3D downstream distance computed with the AD model is used as initial deficit in the BLE model.

The BLE model requires, as noted, an initial deficit as a starting point. In the first test cases of the BLE model we use the deficit computed by the AD model in a downstream distance of 3 rotor diameters (in the following abbreviated as 3D), cf. Figure 2-3. At this distance, the influence from the pressure field has decreased considerably, and it is therefore relevant to compare the results of the two models for positions further downstream in the wake. In Figure 2-3 the deficits at a downstream distance equal to 10D are compared, but as the initial deficit in the BLE model is associated with the 3D distance, the development over a distance of 7D is consequently specified for the BLE model. A reasonable good correlation between the two deficits at 10D computed by the AD and the BLE model, respectively, are seen in Figure 2-3. The BLE model computes, however, a slightly wider deficit. The computations with the BLE model were run with a value of the global wind field constant, k_2, equal to 0.009. This constant is an *empirical constant*, and it may be fine-tuned to achieve an even better agreement between the AD- and BLE models.

As noted by Ainslie [30] the turbulence in the ambient flow plays an important role in the development of the deficits and contributes often more to the total turbulent mixing than the mixing contribution originating from the wake mean shear itself. Ainslie proposes the following equation for the total eddy viscosity

$$\upsilon_T = k_2\, b\left(U_0 - U_c\right) + \upsilon_{Ta}\ , \tag{2-7}$$

where υ_{Ta} is the eddy viscosity contribution originating from the ambient turbulence, which will depend on the specific conditions of the atmospheric boundary layer as well as on the level of turbulence directly generated by the upstream turbine (i.e. the part of the added wake turbulence caused by blade bound vorticity effects). The ambient turbulence contribution has not yet been implemented in the model, but to illustrate the over-all influence of increased turbulent mixing results from variation of the constant k_2 are shown in Figure 2-4. The effect of increasing the constant k_2, and in this way the turbulent mixing, is that the deficit recovers more rapidly but also, at the same time, expands much more.

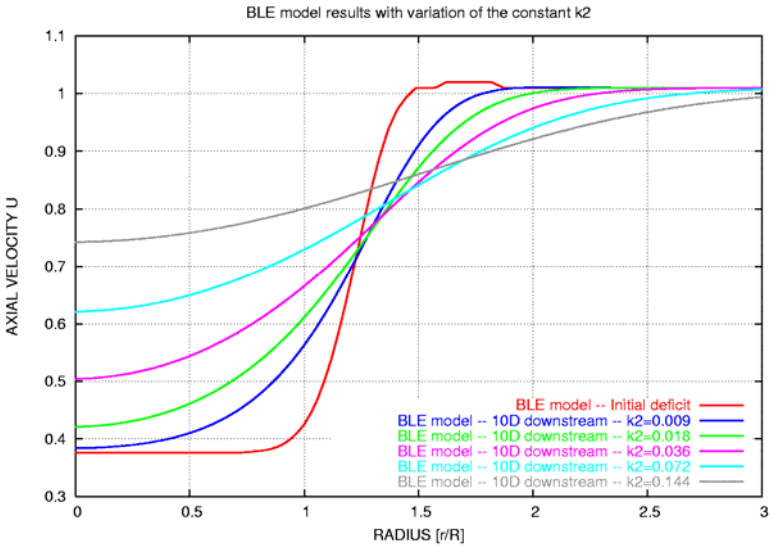

Figure 2-4 Influence of varying the constant k_2 in the BLE model and thus a qualitative illustration of increasing the ambient turbulence in the flow.

In the future, the BLE model will be further developed to facilitate description of a 2-D flow situation. The 2-D extension will provide the necessary generalization to handle wake

deficits resulting from arbitrary interaction between different wakes as well as to include effects caused by the mean velocity profile (i.e. the variation of the horizontal mean wind speed with altitude). In addition, the BLE model will be coupled to an aerodynamic model of the rotor to facilitate a computation of the required the initial velocity deficit by means of a BEM model.

2.1.3 Vorticity formulation

An alternative way of achieving a computationally efficient numerical scheme is to adopt a vorticity formulation. Such a model was developed and implemented. The work is described in detail in [27], while a brief account of the model is given below.

The vorticity approach seems particularly promising for wind turbine wakes which are dominated by a relatively simple vortex system. Each rotor blade sheds a vorticity sheet that quickly rolls up forming two distinct vortices, one at the tip and one at the root. The vortices are lines of concentrated axial (along the line) vorticity that induce a spinning motion in the neighbouring fluid. For constant density, inviscid fluids classical results of Helmholz and Kelvin show that vortices are material lines thus following the flow. The velocity field can be determined from the vortex system by the Biot-Savart law. We can therefore calculate the motion of the vortices directly without having to calculate velocities all over a space filling grid. This is the main advantage with method. The main disadvantage is the non-locality of the Biot-Savart law which makes all vortex segments in the fluid interact.

Vorticity is generated by external forces. In the special case where the force is concentrated on a surface and has constant strength pointing normal to the surface a vortex tube, a continuous trail of vortex rings is shed from the edge of the surface. This could emulate the reaction of a blade element to fluid pressure. In the actuator disk model thrust forces are evenly distributed over the rotor plane resulting in vortex sheet streaming from the rotor edge. If the force has the form of an impulse, varying like a δ-function in time, a single, closed vortex is created. If we wish we can make a hole in the middle of the disk and get a root vortex.

Vortex methods come in a wealth of varieties. A comprehensive literature survey with more than 400 references can be found in [81]. Some methods aim at a complete representation of the vorticity field and can thus be used for direct numerical simulations. Here the vorticity can be represented by mollified (slightly smeared out) multi-poles. Other methods use vortex sheets and lines and aim, like CFD, at a coarse-grained representation of the flow field. The level of detail, that can be obtained by a model, is dictated by the number of parameters used to represent the vorticity field. It also depends on how clever the parameterization is. The purpose of the vortex model which we have developed has not been to compete with the realism of neither DNS or CFD. The aim is to make a model which is simple and fast enough to run on a PC, yet complex enough to reflect basic physics. In particular the model should be able to handle situations such as turbines in yaw, the merger of turbine wakes, effects of shear, meandering of the ambient field and wake instabilities and possibly also canopy effects in wind farms. Such a model would be useful as a scanning tool, e.g. for comparative studies, yielding fast, approximate, but still physically sound results. This could be supplemented by more accurate CFD calculations for critical cases.

The model we have made is based on a pulsating actuator disk model. The axial momentum (thrust) transferred to the fluid is represented by a pulse train. Each pulse represents the total momentum transfer to the fluid during the time it takes for the rotor to sweep the entire rotor plane. An n-bladed rotor thus emits n pulses per revolution. Assuming constant thrust per area each pulse will produce a circular tip-vortex ring and an optional root-vortex ring. The

pulsating actuator disk was preferred to the conventional continuous actuator disk, because vortex rings are easier to handle than vortex sheets, and also because the distinct vortices it produces seem to emulate distinct, helical vortices better.

The model represents vortices by means of piecewise *linear* curves with circulation Γ and core width parameter b[1]. Γ and b are constant along the vortex as well as in time. Piecewise linear vortices have the advantage that the curve integrals in the Biot-Savart law can be done analytically. In a first version the motion was determined by advecting each elbow with the velocity at that point. Although a seemingly natural choice it suffers from a too literal interpretation. The vortices, created initially as circles, should be interpreted as circles even if they are represented regular polygons. Generally the discrete elbow points should therefore somehow represent a smooth curve. This can be achieved in any number of ways, but it is hard to find one that yield analytical expressions for the Biot-Savart integrals. We have therefore chosen to stick to piecewise linear vortices. However, instead of evaluating the self induced part of the elbow velocity at the elbow itself, it is evaluated as the average of the velocities at the two points on the joining segments located one third the distance to a neighbouring elbow. In this way the motion of the elbow better reflects the collective motion of the two joining segments. The one-third rule was found by comparing self induced velocities of regular polygons to the exact value for a circle. The improvement is rather marked. Using the one third rule hexagons actually do better in the test than 48-sided polygons did with the original approach.

Helical vortices instead of rings could be obtained using actuator sticks instead of a plate. Each stick resembles a blade and sheds a vortex continuously from the root and the tip (the two joining downwind). In case the trust changes in time, the vortex is closed and a new is initiated (with root and tip part closed). This variant could be useful in simulations of a turbine standing partly in the wake of another turbine, since it would be able to handle different, time varying thrusts on the blades. However, it would come at a computational cost due to the larger number of vortex segments being generated.

Ambient shear can also be simulated. A crude way of doing this is simply to replace the uniform ambient fields by a sheared field. The effect of this is that the ring vortices get extruded in the axial direction and begin to lean forward. This squeezes the wake and makes it drift upwards (towards higher ambient velocity). This may lead to an early quenching of the wake by instability. However, the approach is over-simplified because it neglects *feed-back* to the vorticity of the ambient flow. In a uniformly sheared flow the vorticity resides on straight lines running perpendicular to the flow. When a line hits the wake the part inside the wake will travel slower than the rest so that the line runs axially at the wake edge. This axial vorticity in turn induces a downward drift on the wake. Most likely, this cancels the upward drift which is therefore probably a spurious effect. The squeezing and possible quenching could, on the other hand, be a real and important phenomena. In any case these arguments show that the *ambient vorticity* should be explicitly represented in the model in order to get the physics right. This is done by releasing linear vortices upwind of the rotor, again at the expense of extra computation time.

The implementation of such refinements as mentioned above was not been made, since the simpler ring model should be tried first. However, the code can relatively easily be adapted.

1 The core width parameter b is not resulting from the model, but has to be specified initially. The model performance is, however, not considered to depend significantly on the particular specification of this parameter.

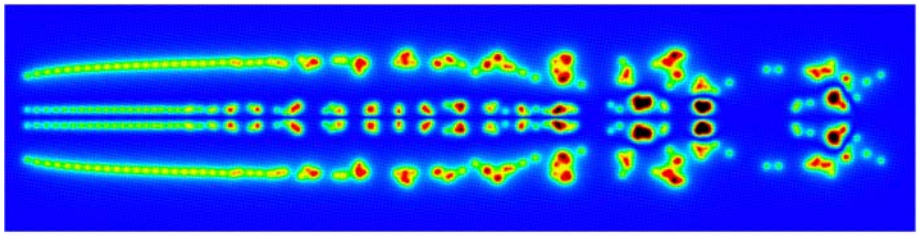

Figure 2-5 Plot of $|\omega|$ in a plane through the wake with perfect octagonal symmetry. The rotor is located to the left and conditions are as for case B, see text.

Since the model resolves time it can be used to study instabilities. We have observed two kinds: Kelvin-Helmholz like instabilities and a chaotic development of shapes. The first kind is illustrated in Figure 2-5 which shows the magnitude of vorticity, $|\omega|$, in a plane through the wake. In these calculations the vortices were initiated as perfectly symmetric octagons, and this symmetry is preserved extremely well by the solver. Close to the rotor the vortices form a smooth sheet, but at some distance the sheet breaks up into separate groups of vortices that revolve each other. This induces structures similar to Kelvin-Helmholz billows. In this particular case the instability sets in first for the root system and shortly after also for the tip system. It grows down the wake where the two systems eventually merge. In other cases, with larger thrust coefficient, C_t, the tip and root systems merge immediately as the instability sets in.

In CFD, where the calculations are much more complicated than here, rotational symmetry can be spontaneously broken by small numerical errors exciting eddies at the smallest scale which the model is able to resolve. Our model is too simple for this, so symmetry is preserved. In reality the symmetry is broken by the slightest non-uniformity of the ambient flow. In order to get more realistic, asymmetric solutions we must put in asymmetry in some way. An easy way is to introduce some jitter in the initial shapes of the vortices. Distorting the octagons by tiny, randomly chosen displacements of their corners has dramatic effects. The imperfections in shape tends to grow more and more as the vortices travel downwind, and it does not seem to matter how small the initial imperfection is. We can even turn on the jitter only for a short while, e.g. distorting vortices covering about one or two rotor diameter, and then continue emitting perfect octagons. In some cases, when C_t is very low, the system will return to symmetry as the asymmetric vortices disappear downwind. Most often, however, the distorted vortices are able to transfer enough distortions backwards in the wake to keep a self sustained chaos.

The model was tested against CFD calculations, in particular the three Tjæreborg cases which are discussed in Section 2.3.2 of this report. We will refer to them as A, B and C. In case A the ambient wind speed is U_a = 6 m/s and thrust coefficient C_t = 1.14. Case B has U_a = 10 m/s and C_t = 0.86, and case C has U_a = 14 m/s and C_t = 0.74.

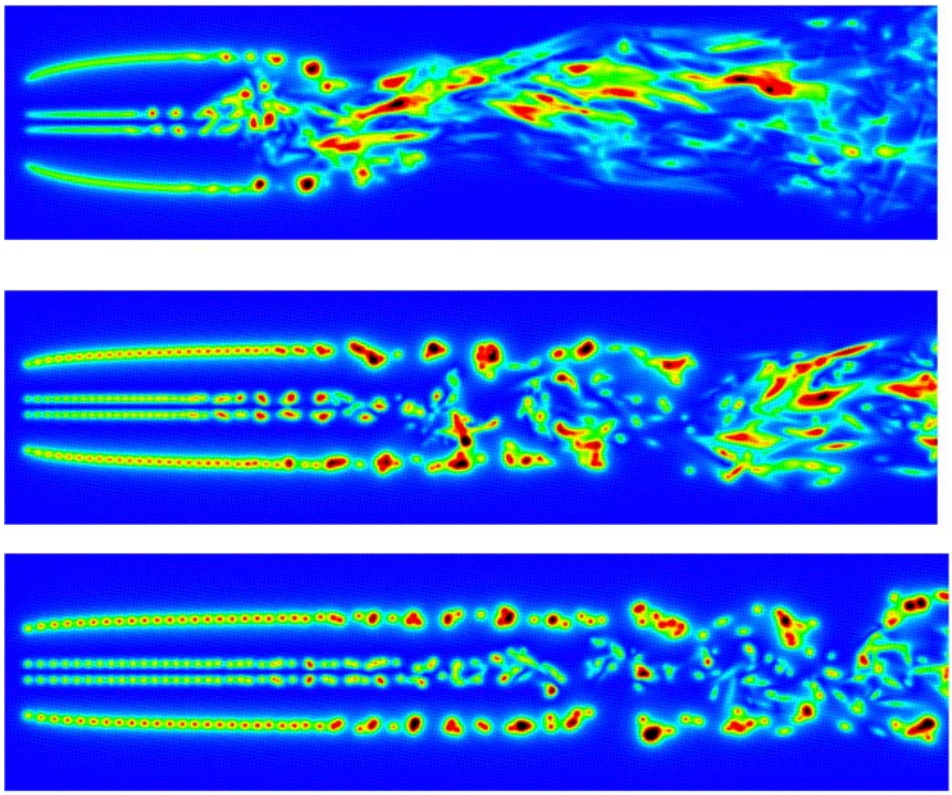

Figure 2-6 Plots of $|\omega|$ in a plane through the wake. The wakes are in the self sustained chaotic state. Upper: case A. Middle: case B. Lower: case C. Figure 2-14 shows similar plots for CFD calculations.

All the three cases exhibit self sustained chaos. Figure 2-6 shows results of recalculation where the chaos was tripped by a short train of vortices with slightly (less than 1%) imperfect shapes. The plots refer to late times where these vortices are too far downwind to have any direct influence, so all vortices shown were in fact born symmetric. For Case C the symmetry breaking is not very pronounced for the tip vortices where Kelvin-Helmholz structures are still prominent. The root system, on the other hand, dissolves after about 6 rotor diameters. In case B the root system dissolves even more rapidly, and the tip system is also dissolved. In case A both system dissolve rapidly starting about 2 rotor diameters downwind, while instability of the tip system sets in slightly earlier. The results are in fair agreement with the corresponding CFD calculations shown in Figure 2-14. In case B and C the development of Kelvin-Helmholz instabilities of the tip vortex system occur more or less as in CFD. The root vortex system generally gets unstable earlier than the tip system in the vortex model, while it is the other way around with CFD. In case A there is a sudden, early onset of instability of the whole wake just as with CFD, although the instability sets in somewhat later than in CFD.

In the vortex model the vortices can end up being heavily stretched in the axial direction. As a result the vorticity tends to align with the wind instead of being perpendicular to it. The induced velocity field therefore changes character. Instead of inducing a well defined wake the vortices begin to induce radial motion, in and out of the wake, thus mixing the wake with the ambient flow. This behaviour does not sound unreasonable, and the model seems to make some kind of sense, even when the vortices become heavily zig-zagged and extruded.

However, the extremely long segments, stretching over many wake diameters, and with needle sharp elbows that occur for case A seem rather bizarre. A more correct treatment would be to add elbow points to vortices that begin to develop complex shapes, but there would be a severe penalty in terms of extra computation time.

Figure 2-7 shows the radial distribution of the axial velocity for the three cases. The results should be compared with corresponding CFD calculations shown in Figure 2-15.

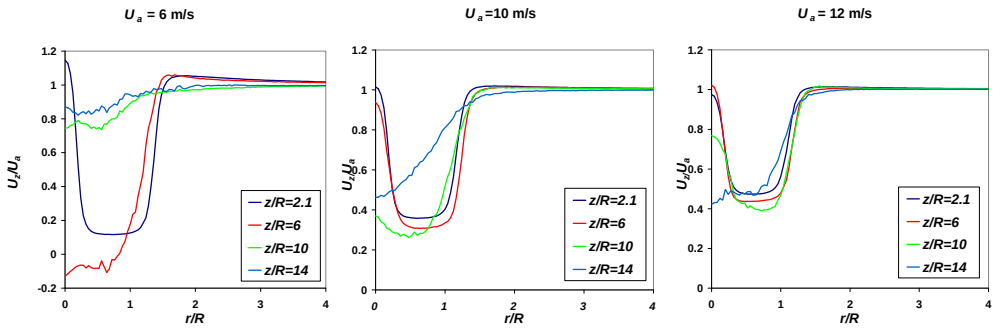

Figure 2-7 Velocity profiles for the three runs A, B and C. The wakes are in the self sustained chaotic state. Figure 2-15 shows similar plots for CFD calculations.

As long as the tip and root vortex systems are intact the agreement is fair. In case B we see some qualitative agreement even in the unstable region. The stretched vortices therefore seem to produce a quite realistic wake. Case A is by far the toughest one. For z/R=2.1 the idealised thrust distributions produces a rather more flat plateau of constant deficit, whereas the thrust distribution in CFD is more concentrated at the tip. At z/R=6, well into the chaotic zone, the vortex model predicts slightly negative velocities, which are not seen in CFD. The recirculation is probably not a healthy feature. Further down the wake the vortex model predicts considerably less velocity deficit than CFD. This is most probably due to exaggerated axial stretching of vortices, happening when parts of vortices are trapped in a recirculation zone. The indication of these tests is that the vortex model works quite well in the near part of the wake before the vortices gets chaotic. It also does fairly well with respect to predicting the chaotic transition, but there are some problems in the chaotic zone when C_t is too large.

An attempt was made to cast the simple vortex model in a more satisfactory mathematical setting using Hamiltonian mechanics. It turns out that equations of motion of a system of vortices can be derived from a Lagrangian using Hamilton's principle (also known as the principle of least action). The Lagrangian was discovered by [82] who needed it in order to apply quantum mechanics to super fluid Helium. The system also has a Hamiltonian, which is conserved, but is otherwise of little use since Hamilton's equations do not apply. The idea is now to replace the continuous curves with curves specified by a finite number of parameters acting as *generalized coordinates*, and minimize the action integral with respect to the parameters. If we use piecewise linear curves the elbow points are the parameters, and the procedure results in equations for the velocities of the elbows. The equations are implicit, but linear and only couple nearest neighbours on vortices, so they are probably not that difficult to solve. The inhomogeneous part involves integrals over segments that average the Biot-Savart velocity. In this way the resulting motion of the vortices becomes a best compromise, since it describes a system of vortices which are being kept piecewise linear by some kind of internal interactions. Such a scheme would probably improve the

model, but it may not entirely cure the problems with stretched and partly trapped vortices that was encountered in case A.

The effect of vortex stretching on the core width *b* was analyzed in the framework of Hamiltonian mechanics. To our knowledge this has not been done before. In the simple version of the model we choose to let *b* stay constant since this ensures conservation of kinetic energy. However, for inviscid flow it can be shown that the core volume is constant, so vortices should get thinner when they are stretched. A simple approach would be to redistribute the core volume evenly over the vortex after each time step, but that would add kinetic energy to the system whenever vortices are stretched. A more correct way is to include *b* as generalized coordinate that varies along the vortex. That, however, leads to a rather complicated model, because it would be capable of supporting Kelvin modes (vorticity waves that can travel on vortices). In order to simplify things the conservation of core volume was treated as a geometric constraint. This is analogous to treating a fluid as incompressible in order to avoid having to deal with sound waves. Thus the equations of motion were derived by applying calculus of variations to the action integral with the conservation of core volume as a constraint. The result is that the centerline moves with the usual Biot-Savart velocity plus an extra term. The extra term is a self induced velocity that depends on the local width and curvature. Moreover, the distribution of core volume is such that it always minimizes the kinetic energy for the given centerline. In other words, a time step can be split in two. First the centerline is moved using the Biot-Savart law and the extra term, and then the core volume is redistributed on the centerline so that the kinetic energy is minimized. We have been able to prove that this in fact leads to conservation of kinetic energy. A model of this kind is still rather too complex, because it requires quite a large number of elbow points (or Fourier modes) to be able to resolve the curvature accurately enough. We may also not have got rid of Kelvin modes. The model implies that vortices become thinnest where the curvature is largest. The self induced velocity increases as the vortex gets thinner, so a sharp bend on a vortex will tend to circle and make coils next to it. This probably only increases the curvature and speeds up the process. The helical shape of the coils then induces a velocity field that tries to empty the coil, and the disturbance spreads along the vortex. This mechanism is precisely what drives a Kelvin mode. On the other hand, from a distance the coiled up vortex would effectively look like a thick vortex, the width being determined by the diameter of the coils. In order for the model to be useful it should therefore be renormalized in some way so that coiling is prevented. That problem was left for future studies.

Comparing the boundary layer formulation with the present vorticity formulation, the main disadvantage with the vorticity formulation is the non-locality of the Biot-Savart law, which makes the computational requirements increase drastically for large downstream distances. The main disadvantages with the boundary layer formulation are that it requires determination of an initial wake deficit, that a procedure for an appropriate determination of the constant k_2 is not obvious, and that the present formulation is 1D only. However, with the mentioned straight forward forthcoming extension of the boundary layer formulation to 2D, there is an obvious potential for the two approaches to complement each other by computing the near field wake behaviour with the vorticity model, and subsequently use the resulting near field wake deficit as input to the 2D boundary layer model for simulation of the far field wake behaviour.

2.2 Wake meandering

The wake meandering model is based on a *fundamental presumption* stating that the transport of wakes in the atmospheric boundary layer can be modeled by considering the wakes to act as *passive tracers* driven by the *large-scale* turbulence structures. Modeling of the meandering process consequently includes considerations of a suitable description of the "carrier" stochastic transport media as well as of a suitable definition of the cut-off frequency defining large-scale turbulence structures in this context.

For the stochastic modeling of wake meandering, we imagine a wake as constituted by a *cascade* of wake deficits, each "emitted" at consecutive time instants in agreement with the passive tracer analogy [1]. We then subsequently describe the propagation of *each* of the "emitted" wake deficit, and the collective description of these thus constitutes the wake meandering model.

Adopting Taylor's hypothesis, the *downstream advection* of these is assumed to be controlled by the mean wind speed of the ambient wind field. With this formulation the wake momentum in the direction of the mean flow is invariant with respect to the prescribed longitudinal wake displacement. This is a considerable simplification allowing for a straight forward decoupling of the wake along wind deficit profile (and its expansion) and the wake transportation process.

As for the dynamics in the *lateral- and vertical directions*, each considered wake cascade-element is displaced according to the large-scale lateral- and vertical turbulence velocities at the position of the particular wake cascade element at each time instant. Thus (in agreement with the description of the downstream wake displacement), the potential mutual interaction of wake momentum- and wake displacement in these directions is implicitly neglected. This is justified by the fact that the wake momentum in the lateral- and vertical directions are insignificant compared to the wake momentum in the along wind direction, and further by the fact that wind turbine power production as well as wind turbine loading are far more sensitive to along wind speed fluctuations.

In mathematical terms, the wake deficit dynamics in the lateral direction, y, and the vertical direction, z, is thus assumed described by the following differential equation system

$$\frac{dy(t,t_0)}{dt} = v_c(y,z,t,t_0) \ , \tag{2-8}$$

$$\frac{dz(t,t_0)}{dt} = w_c(y,z,t,t_0) \ , \tag{2-9}$$

where v_c and w_c are the spatially dependent large-scale turbulent velocities, and t_0 denotes the time instant at which the considered cascade element is emitted. The total dynamics of a particular wake deficit (i.e. a particular cascade-element) is illustrated in Figure 2-8, where the red element symbolizes the meandering wake, the black element shows the wake position in the absence of meandering, and the black box is the limit of the regime, in which the large-scale turbulence structures, causing the wake dynamics, are modeled. The figure illustrates only the wake dynamics in *one* dimension perpendicular to the mean wind direction, but the model obviously includes the dynamics both in the lateral- and the vertical directions as described above.

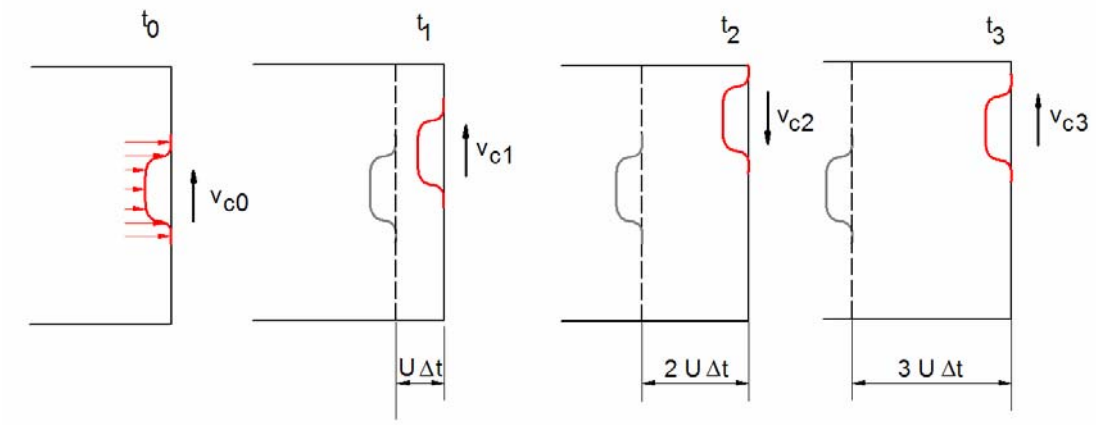

Figure 2-8 Illustration of wake dynamics for a wake deficit "emitted" at time t_0. U is the mean wind speed and v_{ci} is the wake transportation velocity at t_i.

Since the large-scale structure of turbulence is dominating the meandering process, it seems to be a reasonable approximation to consider the lateral- and vertical turbulence spatial homogeneous for each cascade element for *small to moderate downstream distances*. This means that the displacement of the wake center is mainly affected by the large-scale lateral- and vertical velocities over the rotor disc at the release time, and the differential equation system defined by (2-8) and (2-9) may in this case be simplified as [1], [24]

$$\frac{dy(t,t_0)}{dt} = v_r(t_0) \ , \tag{2-10}$$

$$\frac{dz(t,t_0)}{dt} = w_r(t_0) \ , \tag{2-11}$$

where v_r and w_r, in the present context, denote the large-scale turbulent velocities at the position of the rotor disc. For an illustration of this simplified model, the instantaneous cascade element velocities, v_{ci}, should be identical for all time steps, t_i, in Figure 2-8, and the figure thus clearly illustrates the more complex transportation modeling given by equations (2-8) and (2-9).

The choice of a suitable stochastic turbulence field, that in turn defines the stochastic wake transport process, is not mandatory, but may be guided by the characteristics of the atmospheric turbulence at the site of relevance. These characteristics encompass in principle not only turbulence standard parameters such as turbulence intensity, turbulence length scale and coherence properties, but also features like degree of isotropy, homogeneity of the turbulence, Gaussianity of the turbulence etc.. In agreement with conventional practice for turbulence load quantification, the Mann turbulence model [33] is in most cases a proper choice. However, contrary to conventional turbulence loading, only the large-scale turbulence eddies is of relevance for the meandering dynamics, and the physical size (perpendicular to the mean wind direction) of the required turbulence field for this application is thus increased to multiples of the rotor diameter, in order to be able to contain the resulting lateral- and vertical wake movements (cf. Figure 2-8).

In order to obtain the requested stochastic transportation field, we need a consistent definition of what is specifically meant by large-scale turbulence eddies. This is achieved by introducing a low pass filter in the turbulence description, thus extracting the transport

velocities associated with the large scale turbulent eddies only. The cut-off frequency (in Hz), f_c, of the filtering may be specified as

$$f_c = \frac{U}{2D_w}, \tag{2-12}$$

with U being the mean wind speed and D_w denoting the (instantaneous) wake diameter. The motivation for this choice is the following: A displacement wave with period T_p has, due to the Taylor hypothesis, a spatial extend equal to UT_p. Thus half of the spatial extend is associated with positive displacements, and the other half is associated with negative displacements. For a spatial structure, with a characteristic extend equal to a wake deficit diameter D_w, the minimum wave period that allow for a constant sign displacement of all points on the spatial structure is consequently given by

$$D_w = \frac{UT_p}{2}, \tag{2-13}$$

from which the suggested cut-off frequency directly appears. The selected cut-off frequency corresponds to a spatial scale equal to $2D_w$, and the described filtering is thus equally well obtained by averaging the (spatial) turbulence field over a circular area with the characteristic diameter $2D_w$.

It is, however, obvious that the cut-off frequency specifying the large-scale turbulence structures in the present context is not uniquely defined. The "limit" between turbulence structures contributing mainly the wake displacement and mainly to the wake turbulent expansion, respectively, is rather a *frequency range* than a distinct frequency. The suggested cut-off frequency is, however, considered a logically founded choice, and it has further proved to result in convincing correlation between meandering model predictions and direct full-scale measurements (cf. the experimental part of this report).

The described large-scale eddy transport of the wake deficit may, at sufficiently large transportation times, result in a "collision", and subsequent reflection, of part of the wake deficit from the ground surface. In order to fully utilize the convenient and aimed decoupling of the wake deficit modeling and the wake meandering transportation, as described above, a simple model of the reflecting phenomenon is derived based on momentum balance considerations [1]. The derived model predicts a modified wake deficit profile near the reflecting ground under these circumstances. Note in this respect, that despite the analogy between the large-scale driven meandering wake transport and traditional passive tracer modeling, the ground reflection modeling of these two physical mechanisms differ. This is due to the variation in momentum inside a wake deficit compared to the flow conditions associated with dispersal of a passive tracer, where momentum is unaltered by the presence of the tracer. However, in the asymptotic limit of small wake deficits, the two models can be shown to converge.

2.3 Wake turbulence effects

Wind turbine generated *wake turbulence* is a complex phenomenon. The velocity perturbations in a wind turbine wake are thus the combined result of conventional atmospheric background turbulence, blade bound vorticity effects, a turbulence contribution originating from the wake generated shear, and finally the meandering movement of the wake implying that an observer, fixed in space, is intermittently exposed to either wake conditions or free flow. In the present treatment we exclude modeling of the atmospheric turbulence.

The study is divided into three parts dealing with stability of tip vortices, characterization of the wake turbulence fields as resulting from the combined effect of blade bound vorticity and wake generated shear and, finally, engineering types of algorithms for generating such fields. Whereas the first topic is analyzed by means of analytical tools, the treatment of the latter two topics relay heavily on numerical methods.

2.3.1 Stability of tip vortices

The tip vortices will initially be described by a relatively simple flow field consisting of *organized structures*, but later, due to instability phenomenons, they may gradually break down and approach the characteristics of conventional turbulence. This matter has been studied in detail, and two analytical models for tip vortex instability have been derived – one based on the Joukowski approach [7], which is the simplest possible way of describing the far wake behind a wind turbine, and a more detailed approach [5] in which Joukowski's wake model is generalized by including the effect of an axi-symmetric helical vortex field formed from the circulation of the rotor blades.

When regarding wakes, a distinct division can be made between the near and the far wake region. The near wake is normally taken as the area just behind the rotor, where the properties of the rotor can be discriminated, which is approximately up to one rotor diameter downstream. In this regime, the presence of the rotor is apparent by the number of blades and blade aerodynamics, including stalled flow, 3-D effects and the tip vortices. The far wake is the region beyond the near wake, where the focus is put on the influence of wind turbines in park situations, hence modelling the actual rotor is less important. The near wake research is focussed on performance and the physical process of power extraction, while the far wake research is more focussed on the mutual influence when wind turbines are placed in clusters or wind farms.

As for the work reported in this subsection, main attention is put on the *intermediate region* between the near wake and the far wake in order to study the *stability* and development of a fully developed wake vortex structure. The presented results are restricted to *uniform*, *steady* and *parallel* inflow conditions, thereby excluding wind shear, tower interference and dynamic inflow.

The approach taken to investigate tip vortex stability is a *linear stability analysis* based on an analytical formulation of the wind turbine wake. As previously mentioned two analytical wake models, of various complexities, form the basis for this analysis.

Analytical wake models

This section presents the analytical vortex models of wind turbine wakes in question. Basically, the true/physical wake vortex system is simplified by being replaced by N helical tip vortices of strength (circulation) Γ embedded in an inner vortex structure representing the vortices emanating from the inner part of the blades and the hub. As for the simplest of the considered models, the inner vortex structure is reduced to one concentrated vortex structure, located at the symmetry axis, with its circulation equal to the sum of the relevant tip vortex circulations in order to balance those.

The two models in question will in the following be referred to as the J-model (the simple model) and the O-model (the more detailed model), respectively. As the O-model can be considered a generalization of the J-model, we first describe the J-model and then subsequently the O-model. A basic hypothesis for both models is that the wake is assumed fully developed, i.e. that the wake description is restricted to downstream distances, where the wake expansion can be considered independent of the pressure drop over the rotor.

The J-model was originally proposed by Joukowski [34] for a *two-bladed* propeller. Adopting the same principles, this model is in the present context generalized to an *N*-bladed rotor. We imagine the wake vorticity to be concentrated in *N* helical tip vortices supplemented by a hub (or root) vortex lying along the system axis. This (*N*+1)-vortex system, consists of an array of infinitely long helical vortex lines with *constant pitch and radius* (see Figure 2-9-a). This model is the simplest way of describing the fully developed wake behind a wind turbine (or a propeller).

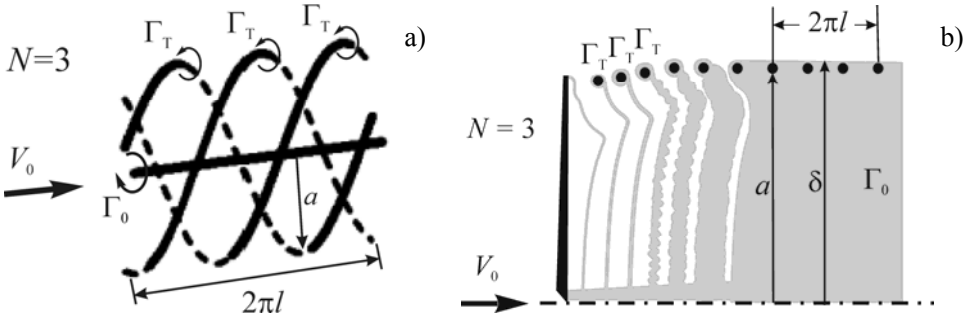

Figure 2-9 Sketch of the vortices in a far wake behind a rotor: (a) model proposed originally by Joukowski (1912); (b) vorticity distribution in meridional cross-section of the wake behind a wind turbine rotor.

We denote the ambient undisturbed axial flow velocity by V_0, the along axis coordinate by z, and constant pitch of the helices by l (cf. Figure 2-9). The resulting axial velocity of the vortex system is thus defined in helical variables $\left(r, \chi = \theta \mp z/l\right)$ by the formula

$$u_z\left(r,\chi\right) = V_0 - w_z\left(r,\chi\right), \tag{2-14}$$

where the axial velocity component, w_z, induced by the N helical tip vortices, may be determined by the following expression, derived by Okulov [35]:

$$w_z\left(r,\chi\right) \cong \frac{\Gamma N}{2\pi l}\begin{Bmatrix}1\\0\end{Bmatrix} + \frac{\Gamma}{2\pi l}\frac{\sqrt[4]{l^2+a^2}}{\sqrt[4]{l^2+r^2}}\,\mathrm{Re}\sum_{n:=1}^{N}\left[\frac{\{\pm\}e^{i(\chi-2\pi n/N)}}{e^{\{\mp\}\xi}-e^{i(\chi-2\pi n/N)}}\right.$$
$$\left. + \frac{l}{24}\left(\frac{3r^2-2l^2}{\left(l^2+r^2\right)^{3/2}} + \frac{9a^2+2l^2}{\left(l^2+a^2\right)^{3/2}}\right)\ln\left(1-e^{\xi+i(\chi-2\pi n/N)}\right)\right]. \tag{2-15}$$

The azimuthal velocity component, w_θ, is accordingly given by

$$w_\theta\left(r,\chi\right) = \left(\Gamma N/2\pi r\right) - \left(l w_z\left(r,\chi\right)/r\right). \tag{2-16}$$

In formulas (2-15) and (2-16), the terms in the braces are defined such that the upper one corresponds to $r < a$ and the lower one to $r > a$. The helical vortex parameters a, l, Γ are introduced in Figure 2-9, where Γ_T refers to the circulation of a tip vortex and Γ_0 refers to the circulation of the inner (hub) vortex, and

$$e^{\xi} = \left[r\left(l+\sqrt{l^2+a^2}\right)\exp\left(\sqrt{l^2+r^2}\right)\right] \Big/ \left[a\left(l+\sqrt{l^2+r^2}\right)\exp\left(\sqrt{l^2+a^2}\right)\right].$$

From equation (2-15) it is seen that the azimuthally averaged axial velocity is *constant* in the wake. This is a direct implication of one of the basic assumptions of Joukowski, that the circulation along each rotor blade is constant ($\equiv \Gamma$), and that the total circulation is zero. If we look at experimental data, however, a constant axial velocity profile is rarely seen. This is the basic motivation for the formulation of the O-model.

In order to develop a model (i.e. the O-model) that is capable of reproducing measured velocity distributions, we extend the model of Joukowski by assuming the tip vortices to be embedded in an axi-symmetric helical vortex field formed from the circulation Γ_0 of the rotor blades and the hub (see Figure 2-9-b). The resulting axial- and azimuthal velocity components are described by the following formulas [21] proposing a simple linear correction to the wake field described by the J-model:

$$u_z = V_0 - w_z + \frac{\Gamma_0 f}{2\pi l},\; u_\theta = w_\theta - \frac{\Gamma_0 f}{2\pi r},\quad f = \frac{1}{\delta^2}\begin{Bmatrix} \delta^2 - r^2, r < \delta \\ 0, \quad r \geq \delta \end{Bmatrix}, \tag{2-17}$$

where δ is defined in Figure 2-9-b.

In fact, several possibilities for appropriate velocity distributions exist. Basically, they have to be a solution of the Euler equations, and at the same time they need to fit to experimental observations. The proposed model obeys both properties.

To validate the O-model expressed in (2-17) we compare it to the experimental laboratory results of Medici and Alfredsson [36]; see Figure 2-10. A very good agreement between modeled and measured velocity distributions are seen for both the axial- and azimuthal velocity components. In contrast to this, the J-model results in an unrealistic 1/r behavior for the azimuthal velocity and a constant for the axial velocity.

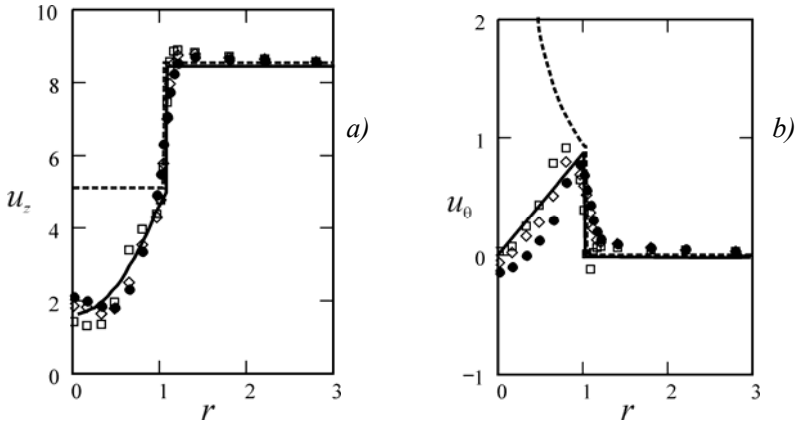

Figure 2-10 Average axial (a) and azimuthal (b) velocity profiles calculated by extended model (———) and by the Joukowski model (– – –). The symbols are experimental data measured by Medici and Alfredsson [36] in different cross-sections downstream from the rotor plane: z/a = 2.8 (□); 3.8 (◊) and 4.8 (•).

An additional interesting finding in the laboratory measurements [36] is the appearance of a low frequency in the wake. The frequency is an order of magnitude smaller than that of the rotational frequency of the tip vortices. Medici and Alfredsson attributed the phenomenon to be similar to the vortex shedding occurring in the wake behind a solid disc determined from the Strouhal number. We will utilize their experimental results for a further validation the O-model.

In Figure 2-11-a, we depict a wake subjected to low-frequency oscillations.

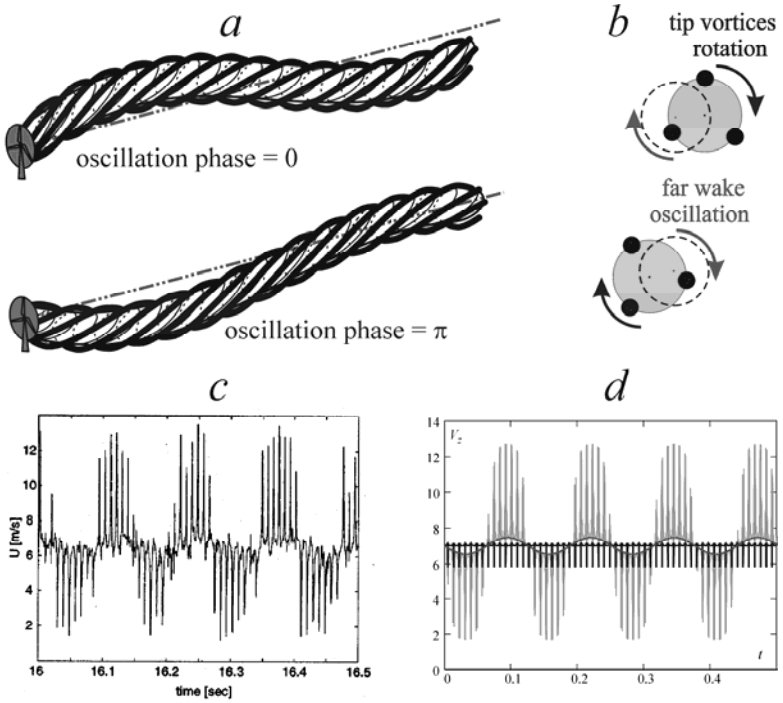

Figure 2-11 Sketch of low-frequency meandering of the wake behind a wind turbine: (a) in space and (b) in the Treffitz plane. Time histories of the axial velocity: (c) measured (Medici and Alfredsson, [36]) and (d) computed using the new analytical model.

The measured time signal of the axial velocity (Figure 2-11-c) near the boundary of the wake is dominated by two frequencies with very high peaks superposed the highest frequency. By prescribing the amplitude of the *low frequency part* to the measurements we compute a time signal of the velocity (Figure 2-11-d) by de-centering the O-model described by (2-17) as shown in Figure 2-11-b. The resemblance of the two time histories is striking, and the O-model thus has the capacity also to capture such unsteady effects.

Tip vortex stability

The derived analytical wake models forms, as noted, the basis for the work on stability of the tip vortices in the wake behind a wind turbine reported in [7] for the J-model and in [5] for the O-model.

As the more elaborate stability model formulated in [5] (based on the O-model) is mathematically substantially more complicated than the model [7] (based on the J-model), the present description will, for the sake of clarity, be based on the J-model. In either case a *linear* stability analysis is conducted, and the applied principles are basically identical.

The first linear stability analysis of the wake generated by a rotor was carried out by Gupta and Loewy [69] who represented the tip vortices by a multiple of helical vortices, neglecting the influence of the root vortex. Employing a numerical "cut off" approximation of the vortices, they extended the stability analysis by Levy and Forsdyke [70] and Widnall [71] for centerline perturbations of a single helical vortex. It should be noted, however, that most

of the results of Gupta and Loewy were calculated at a pitch value $\tau = 0.1$ and a vortex core of radius $\sigma = 0.1$, with some few additional cases for τ in the range from 0.05 to 0.2 and a core radius 0.33. For all analyzed cases they found that the tip vortices are unstable and subject to a large range of possible instability modes. In contrast to their results, the first analytically obtained solution by Okulov [68] showed that this vortex system is stable at large pitch values.

The present analysis is a generalization of the wake model derived in [68] and [69] that also includes the influence of the hub vortex (Figure 2-9-a), as in the J-model. The aim of the analysis is to determine the influence of the hub vortex on the stability of a multiple of *N* helical vortices located in a rotor wake described by Joukowski's wake model.

We consider the stability of a system of *N* helical vortices of circulation Γ and a rectilinear center vortex of circulation Γ_0 with respect to small displacements from their equilibrium position (see Figure 2-9-a). The axes of the helical vortices in this *N*-plet are lying azimuthally along a circle of radius a with an angular shift of $2\pi/N$. The helical vortices are determined by the dimensionless core size $\varepsilon = \sigma/a$, the dimensionless pitch $\tau = l/a$, and circulation Γ. As additional model parameter we introduce the circulation ratio $\gamma = \Gamma_0/N\Gamma$, the strength of the hub vortex divided by the total circulation of the multiple. Thus, putting $\gamma = -1$ corresponds to the J-model. As noted earlier the wake models analyzed in [68], [69] correspond to $\gamma = 0$.

We assume a first-order perturbation of the position of the $k-$ helical vortex of the form,

$$\delta\mathbf{r}_k = \delta\tilde{\mathbf{r}}_k \exp\left(\alpha t + 2\pi i \frac{ks}{N}\right),$$

where $\delta\tilde{\mathbf{r}}_k$ is the amplitude vector of the perturbations, s is the sub-harmonic wave number that takes values within the range $[1, N-1]$, corresponding to $N-1$ independent eigenfunctions, and α is the amplification rate. An analysis of the stability using the technique described in [68] (slightly modified so as to take into account the induced velocity of the hub vortex and the additional self-induced velocity caused by small deviations of the helix axes from their equilibrium) leads to the following analytical solution for the non-dimension amplification rate

$$\alpha\left(4\pi a^2/\Gamma\right) = \sqrt{AB}\,, \tag{2-18}$$

where

$$A = s\left(N-s\right)\frac{\sqrt{1+\tau^2}}{\tau} - \frac{\tau}{4}\frac{4\tau^2-3}{\left(1+\tau^2\right)^{5/2}}\left(\frac{N}{s} - E - \psi\left(-\frac{s}{N}\right)\right);$$

$$B = -4N\gamma + s\left(N-s\right)\frac{\left(1+\tau^2\right)^{3/2}}{\tau^3} - 2N + 2\frac{N-2}{\tau^2} + \frac{1+2\tau^2}{\tau\left(1+\tau^2\right)^{1/2}}$$

$$+\frac{1}{\tau\left(1+\tau^2\right)^{3/2}}\left[\left(\tau^2-\frac{1}{4}\right)\left(E+\psi\left(-\frac{s}{N}\right)-\frac{N}{s}+\frac{3}{4}-2\tau^2-\ln\left(N\delta\frac{\left(1+\tau^2\right)^{3/2}}{\tau}\right)\right)\right]$$

$$+\frac{\tau^3}{\left(1+\tau^2\right)^{9/2}}\left(2\tau^4-6\tau^2+\frac{3}{4}\right)\frac{\varsigma(3)}{N^2};$$

and where $E = 0.577215\ldots$ is the Euler constant, $\varsigma(3) = 1.20206\ldots$ is the Riemann zeta function, and $\psi(\cdot)$ is the psi function. The first term of B describes the effect of the hub vortex. Therefore, a system consisting of N helical vortices is unstable if $AB \geq 0$ for any combination of s, τ, ε, γ. Note that in the limit $\tau \to \infty$, A and B tend to the point vortex solution given by

$$4\pi aA/\Gamma = s\left(N-s\right) \tag{2-19}$$

and

$$4\pi a^2 B/\Gamma = -4N\gamma + s\left(N-s\right) - 2\left(N-1\right), \tag{2-20}$$

as described by Havelock [72]. Analyzing the asymptotic solution given by (2-19) and (2-20) helps to define the absolute maximum amplification rate, α, for s by taking the value closest to $N/2$, i.e. $s^* = N/2$ for even N and $s^* = \left(N \pm 1\right)/2$ for odd N.

As noted in [69] the amplification rate varies with the pitch of the helical vortices controlled by the rotor tip speed ratio. As an illustration, in Figure 2-12 we plot the absolute maximum amplification rate as function of helical pitch and number of tip vortices *n* for a wake model without hub vortex ($\gamma = 0$). In the plot, results from our analytical model are compared to the numerical calculations presented in [69].

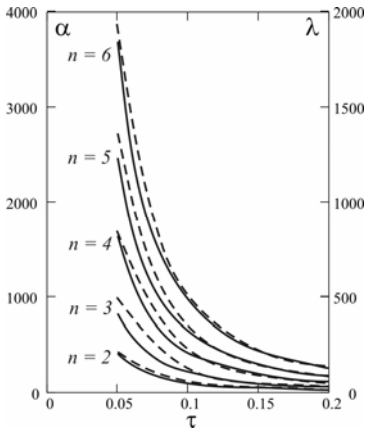

Figure 2-12 Comparison of maximum amplification rate calculated by analytical solution (2-18) with numerical simulation [69]. From [7].

Next, we consider the influence of different values of the circulation ratio γ on the equilibrium properties of the helical multiple.

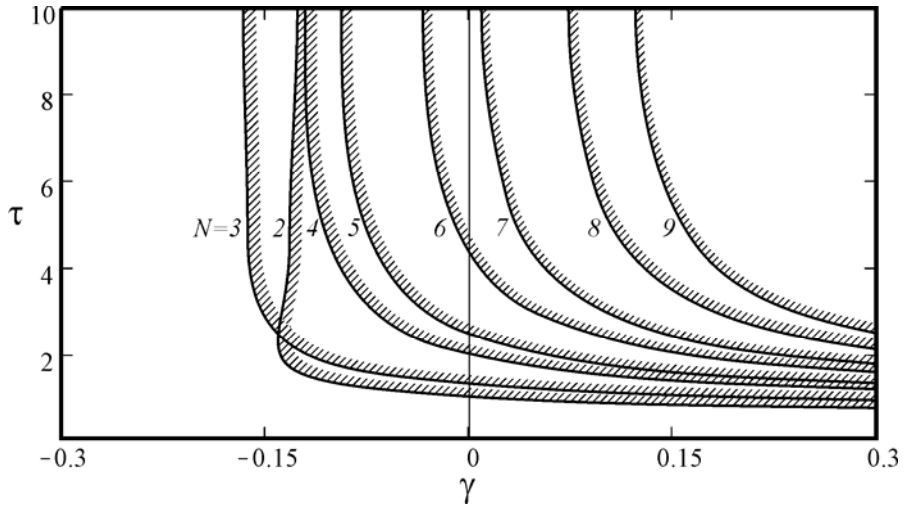

Figure 2-13 Neutral stability curves for helical tip vortices behind a N-bladed rotor as function of the circulation ratio γ. Stable regions are located on the dashed side of the curves. From [7].

Figure 2-13 shows neutral stability curves of the most unstable mode, when $\alpha\left(N, s^*, \gamma, \tau\right) = 0$, for different *N*-plets as function of the circulation ratio γ and helical pitch τ. From the data we can conclude that for $N < 7$ stable states may exist for $0 > \gamma > -1$, i.e. the circulation of the hub and the tip vortices have different signs. For $\tau \to \infty$ the stability limit is given as

$$\gamma_\infty = \left[s\left(N - s\right) - 2\left(N - 1\right)\right] / 4N \,. \tag{2-21}$$

These values are given explicitly in Table 2-1.

Table 2-1 Stability limits of circulation ratio for helical pitch tending to infinity.

N	2	3	4	5	6	7	8	9	10	11	12	13	14	15
γ_∞	$-\frac{1}{8}$	$-\frac{1}{6}$	$-\frac{1}{8}$	$-\frac{1}{10}$	$-\frac{1}{24}$	0	$\frac{1}{16}$	$\frac{1}{9}$	$\frac{7}{40}$	$\frac{5}{22}$	$\frac{7}{24}$	$\frac{9}{26}$	$\frac{23}{56}$	$\frac{7}{15}$

Note that (2-21) is identical to the stability limit of Morikawa and Swenson [73] for a system consisting of N point vortices in a circular array and a centre vortex. For some reason, however, they mistakenly wrote that the stability limit becomes infinite for $N = 2$ and 3.

Please note that the vortex configuration is unstable for small values of the helical pitch τ and for most part of the negative regime of γ. From Figure 2-13 it is further seen that the wake behind a 3-bladed rotor is the *least unstable*. For the important case $\gamma = -1$, where the total circulation of the vortex configuration is zero, the wake described by the J-model is

unconditionally unstable for all pitch values. It may be noted that this important conclusion is the result of an exact analysis, involving all dominant terms, whereas our previous conclusion about the possibility of conditional stability for the J-model [74] was based on an approximate approach in which we neglected the derivatives of the self-induced motion of the tip vortices.

Most experiments on rotor wakes support this conclusion. As an example, Landgrebe [75], by means of flow visualizations, noted that the wake seemed to be stable in the immediate vicinity of the rotor plane, whereas it clearly became unstable at some distance downstream from the rotor. Some investigations, however, indicate that the wake under some conditions may be stable. The review article by Vermeer, Sørensen and Crespo [76] shows several examples from the pertinent literature on visualizations of stable vortex behavior.

It is possible that various factors in near wake (e.g. variations in the helical pitch and tip vortex core) can affect vortex stability. In fact, flow visualizations [75] as well as numerical simulations [77] have revealed that the geometry of rotor wakes may differ significantly from a pure helical shape. Another explanation for this apparent contradiction is that the J-model is too simple to describe the general behavior of rotor flows.

Indeed, the J-model is based on the assumption that the circulation is constant over the blade span, and that the wake consists only of a hub vortex and trailing tip vortices. Considering the non-constant circulation that usually characterizes the operating range of a rotor, trailing vortices are created behind the rotor blades. These vortices form helical vortex sheets or screw surfaces along with the tip vortices. After the vortex sheet and the tip vortices are formed behind the rotor, a complicated roll-up process starts to take place due to the mutual influence between the vortices. It is likely that this process eventually will divide the flow field into strong, distinct helical tip vortices and a more or less compact center vortex with a core size of up to a rotor radius. Such a behavior is of course not included in the somewhat simplistic J-model, and this fact has motivated a stability analysis based on the O-model which, besides the tip vortices, includes the vortex sheets formed by the blade trailing vortices.

A detailed description of the refined stability analysis based on the O-model can be found in [5]. The most significant difference between the stability analyses based on the J-model and the O-model, respectively, is that whereas the simple approach predicts *unconditionally unstable* performance of the tip vortices for all pitch values (i.e. tip speed ratios), the more detailed model predicts a more diversified situation, with the included vortex sheet being able stabilize the tip vortices for certain choices of the parameters that describes strength and size of the vortex sheet.

2.3.2 Characterization of wake turbulence based on CFD

The combined effects of the blade bound circulation and the mechanically generated turbulence contribution arising from the wake shear have been analyzed by intensive CFD simulations, with the wind turbine being modeled using a vortex line approach. Various wake situations has been treated applying a periodic boundary approach.

Whereas the analytical approach presented in Section 2.3.1 is restricted to the *intermediate wake region*, where the effect of the individual wind turbine blades (except for the tip vortices) can be considered azimuth averaged by the physics of the wake flow, and the vortex pattern consequently approximated by an azimuth homogeneous vortex structure superimposed by distinct tip vortices, the present CFD approach accounts for the trailing vortices that are created behind the *individual* rotor blades as well as for the generated tip

vortices. The CFD approach thus applies in the entire wake regime, including the transient regime in which the individual vortex sheets and tip vortices, by means of a complicated roll-up process driven by mutual influence between vortices, transform to an azimuth homogeneous continuous vortex structure superimposed by distinct tip vortices.

The basic idea behind the present CFD approach is to embed the rotor loading, represented by body forces, in a model the gross flow field (i.e. the ambient flow field) around the rotor, simulated by the Navier-Stokes equations using direction or Large Eddy Simulation (LES) techniques. This technique enables to study wake dynamics without having to resolve in detail the viscous boundary layer of the individual rotor blades.

Three different wake situations have been considered – the wake behind a *single rotor*, the wake behind *three rotors* in a row, and the wake behind *"infinitely" many rotors* in a row. The considered scenarios are, however, quite idealized, mainly because the effects of the ambient atmospheric turbulence are neglected. The primary effect of this simplification is that the dynamic rotor inflow conditions, caused by the large scale turbulence structures of the atmospheric boundary layer (i.e. wake meandering), are not accounted for. Consequently, the results must be interpreted with some care. Nevertheless, they show good qualitative agreement with full-scale experimental investigations of low turbulence flow conditions (cf. Section 3.2.5).

The numerical model

The computations were carried out using the 3-D flow solver *EllipSys3D*, developed in collaboration between DTU (Michelsen [37], [38]) and Risø (N.N. Sørensen, [39]). This code solves the discretized incompressible Navier-Stokes equations in general curvilinear coordinates using a block structured finite volume approach. *EllipSys3D* is formulated in primitive variables (pressure-velocity) in a non-staggered grid arrangement. In the present work, the pressure correction equation is solved using the PISO algorithm, and pressure decoupling is avoided using the Rhie/Chow interpolation technique [40]. The convective terms are discretized using a hybrid scheme combining the third order accurate QUICK scheme and the fourth order CDS scheme. This technique was employed as a compromise between avoiding unphysical numerical wiggles, occurring when using a pure fourth order scheme, and limiting numerical diffusion due to the upwind biasing nature of the QUICK scheme. The time discretization was specified such that the tip of a rotor blade during a time step moved less than a half cell size.

The flow field around the wind turbine rotor is simulated using the so-called actuator line technique developed by Sørensen and Shen [41]. In this model the three-dimensional Navier-Stokes equations are solved with body forces distributed along rotating lines representing the blades of the wind turbine. The flow field is thus determined by solving the three-dimensional Navier-Stokes equations using LES, whereas the loading on each blade is computed by calculating the local angle of attack to determine the local forces from tabulated airfoil data. The method was originally formulated in vorticity-velocity variables, but was later reformulated in primitive variables (pressure-velocity) by Mikkelsen [42] in order to combine it with *EllipSys3D*.

The advantage of representing the individual blades by line-distributed loadings is that much fewer grid points are needed to capture the influence of the blades, as compared to what would be needed for simulating the actual geometry of the blades. Therefore, the actuator line model allows for a detailed study of the dynamics of the different wake structures, such as the tip- and root vortices, using a reasonably number of grid points. Furthermore, the model benefits from being applicable with simple structured grids, and therefore issues

connected to grid generation do not occur. The drawback of the method, on the other hand, is that it relies on the quality of tabulated airfoil data.

The computations were conducted using airfoil data from the Tjæreborg wind turbine. The blade radius, R, of this turbine is 30.56 m, and it rotates at 22.1 RPM corresponding to a tip speed of 70.7 m/s. The blade sections consist of NACA 44xx airfoils with a chord length of 0.9 m at the tip, increasing linearly to 3.3 m at hub radius 6 m. The blades are linearly twisted 1° per 3 m. The technical details of the rotor can be found in Øye [43].

The wake behind a single turbine

In the following some of the results obtained from three simulations of the stand-alone wind turbine are presented. Computations were carried out for the rotor operating at tip-speed ratios of 11.78, 7.07 and 5.05, corresponding to the free stream wind speed, U_0, being equal to 6, 10 and 14 m/s, respectively, in order to study the effect on the wake when changing the thrust on the rotor.

Figure 2-14 shows the contours of the instantaneous absolute vorticity, in the vertical symmetry plane, for each of the three tested cases. Regions of high vorticity appear as light colours. Note, that the rotor is located to the left in the plots and that only the downstream development of the wake is shown. The bound vorticity of the blades is seen to be shed downstream from the rotor in individual vortex tubes. A closer inspection of the vorticity contours at U_0 = 6 m/s revealed that the distinct tip-vortex pattern is preserved about 0.5 rotor radii downstream, after which they smear into a continuous vorticity sheet. In the case where the free stream velocity is U_0 = 10 m/s and U_0 = 14 m/s, distinct tip vortices can be observed approximately 1.5 rotor radii and 7 rotor radii downstream, respectively. In all cases the structures might have been preserved even further if a finer grid had been used, or if a less diffusive scheme than the QUICK was applied. Moreover, it should be noted that using the absolute value of the vorticity as a mean of identifying vortices is limited by its strong dependence on the chosen contour levels, and therefore vortex structures might very well be present even though they are not immediately visible in the plots.

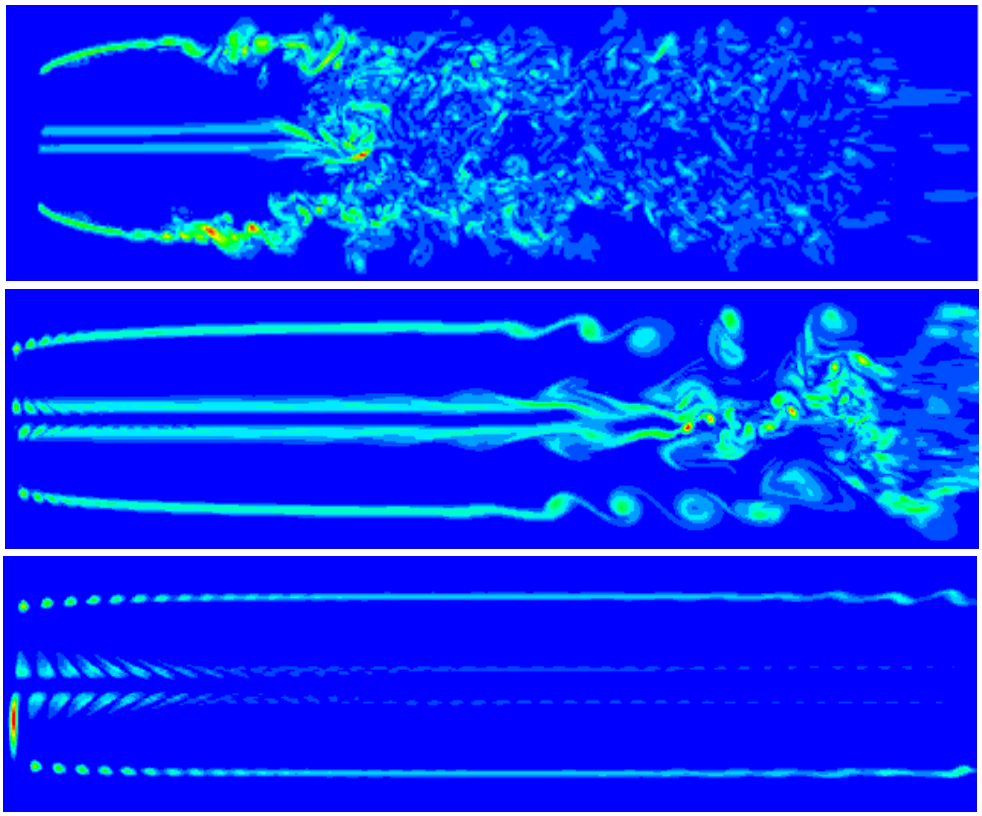

Figure 2-14 Downstream development of wake behind a wind turbine. Upper Figure: U_0 = 6 m/s; Middle Figure: U_0 = 10 m/s; Lower Figure: U_0 = 14 m/s. In all figures the rotor is located to the left.

For the rotor operating at the highest tip-speed ratio instability of the tip vortices is observed only 2 rotor radii downstream, and 5 rotor radii downstream the entire wake completely breaks up. In the case where U_0 = 10 m/s the tip vortices are observed to undergo a Kelvin-Helmholz instability approximately 7 rotor radii downstream. The root vortex also becomes unstable at this position. Further downstream the root and tip vortices interact in a complicated pattern, which causes the wake to become fully turbulent.

Instability of the tip vortices is also observed in the last case where U_0 = 14 m/s, but as expected it takes place even further downstream (approximately 10 rotor radii downstream) and is not as strong as observed for the former two cases. This is due to the generally higher stability and persistence of the tip vortices when the tip-speed ratio, and thus also the trust, is low.

Figure 2-15 shows the computed mean wake deficits as a function of downstream position for each tested free stream velocity as indicated in the figure. Close to the rotor, the deficit correlates directly with the load distribution of the rotor. In normal operation the highest loading is located around 2/3 radius, while the loading close to the hub is low. Further downstream the deficit develops due to the turbulent mixing and, close to the rotor, also due to the pressure field behind the rotor. Moreover, Figure 2-15 reveals that the wake development significantly depends on the loading of the rotor.

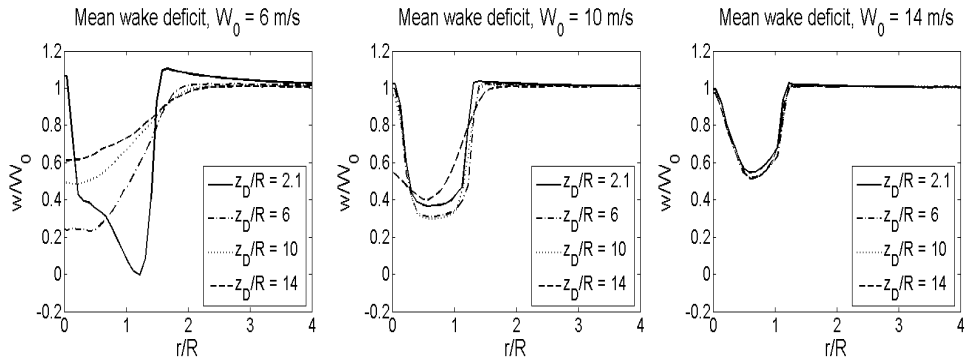

Figure 2-15 Velocity distributions in the wake behind a wind turbine. Upper Figure: U_0= 6 m/s; Middle Figure: U_0 = 10 m/s; Lower Figure: U_0 = 14 m/s.

The wake behind three turbines in a row

The development of the wake is studied for the case of three rotors in a row, where the distance between the rotors is 6 rotor radii. The rather close spacing was chosen as a compromise of on one hand being able to preserve the generated flow structures and on the other hand keeping the computer costs at a reasonably level.

In Figure 2-16 we show iso-vorticity contours in a cross-section along the axis of the rotors. When the incoming wind is in line with the row, the wake behind the first turbine is seen to be dominated by organized tip and root vortices, whereas the flow is seen to undergo massive separation over the second rotor, causing the third rotor to operate in a completely separated flow. It should though be mentioned that the highly separated flow is partly a result of the rotors being forced to operate at the same tip speed ratio, whereby the tip-speed ratio and, thus also, the drag gets very high for the downstream rotors.

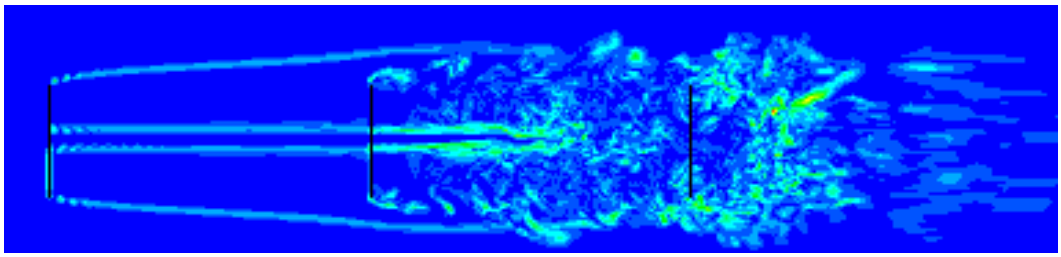

Figure 2-16 Development of the wake behind three rotors in a row. The wind speed is equal to 10 m/s, corresponding to a tip speed ratio of 7; Turbine spacing corresponds to 6 rotor radii.

To quantify the structure of the flow field we compute the azimuthally averaged axial velocities in the wake behind the three rotors. The results are shown in Figure 2-17, Figure 2-18, and in Figure 2-19, which show the averaged velocities as function of radius at, respectively, 1, 3 and 5 radii behind the rotor planes.

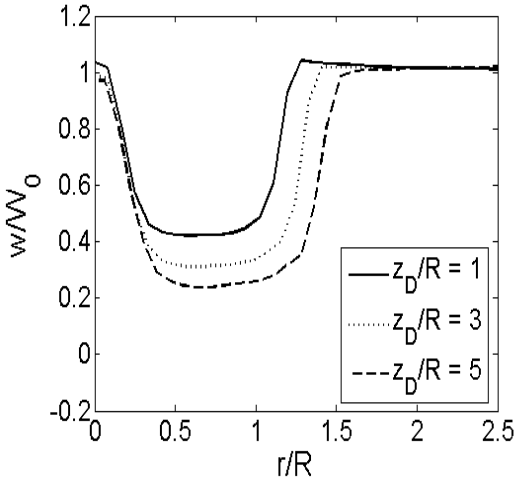

Figure 2-17 Averaged axial velocity between the first and the second rotor.

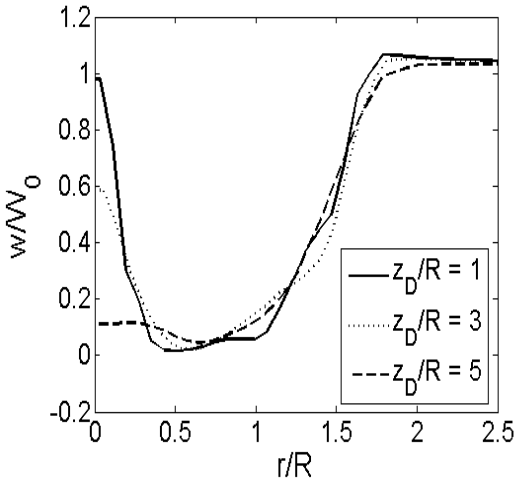

Figure 2-18 Averaged axial velocity between the second and the third rotor.

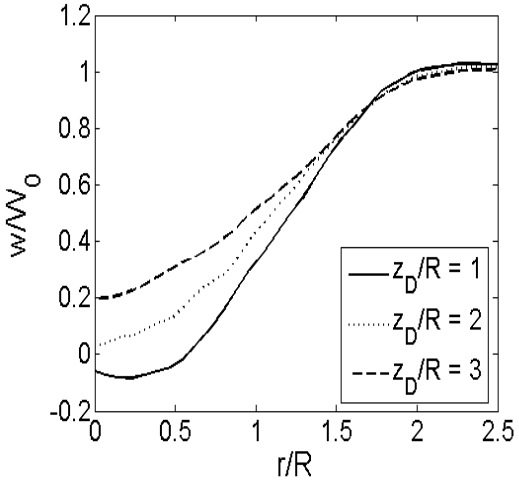

Figure 2-19 Averaged axial velocity behind the third rotor.

From Figure 2-17 the azimuthally averaged axial velocity profiles are, for all the three considered cross-sections, seen to be nearly constant over most of the radial distance, i.e. from r/R=0.3 to r/R=1.0. This is a clear indication that the wake is dominated by the induction of distinct root and tip vortices. From Figure 2-19, on the other hand, we observe a bell-shaped wake deficit, indicating that the flow here is dominated by small-scale turbulence. From theoretical considerations it is known that the axial velocity in the far field of a turbulent wake is described by a Gaussian distribution, if the turbulent viscosity is assumed constant in the wake region, and if the wake deficit is assumed axi-symmetric and self-similar [83]. In between the second and the third rotor (see Figure 2-18) the flow is seen to undergo a transition from a flow field described by organized vortex structures to a flow field that is dominated by small-scale turbulence.

The wake between "infinitely" many turbines in a row

To study the generation of turbulence in the interior of a wind farm we here consider a row of turbines subject to periodic in- and outflow conditions. The introduction of periodic boundary conditions in the flow direction is a technique that has been largely used to study the generation of turbulence in boundary layers in channels. In the present case the turbulence is generated by the *'mixing effect'* of the rotor itself. In the following we will present some results from the simulations. In Section 2.3.3 we will demonstrate how these results can be employed to derive low-dimensional turbulence models for later use in e.g. Blade-Element Momentum (BEM) codes.

Figure 2-20 - Figure 2-24 show iso-vorticity contours illustrating how the flow develops as a function of time. As a time indicator we employ the 'turn-around' time that is defined as the time it takes for a flow structure to pass through the domain once.

Designating the mean convective axial velocity in the wake as U_0, the approximate time it takes for a flow structure to be advected through the domain is $T = L / U_0$, where L is the length of the flow domain. From the figures it is seen that the 'start-up' phase is associated with the development of distinct tip vortices and an inner vortex structure, corresponding to the usual transient for a single wind turbine starting up. After one 'turn-around' time the wake, which was developed in the initial phase, goes through the rotor and creates a wake consisting of coherent tip vortices superposed a turbulent spot in the interior of the wake (cf. Figure 2-22).

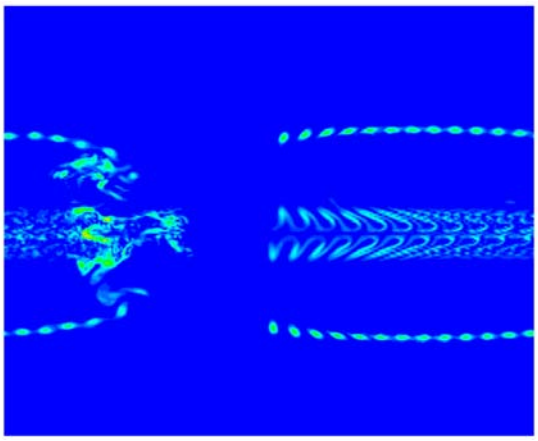

Figure 2-20 Iso-vorticity contours of the initial stage of the transient.

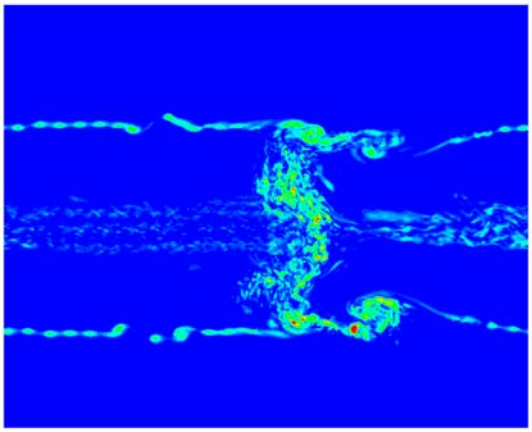

Figure 2-21 Iso-vorticity contours after one 'turn-around' time.

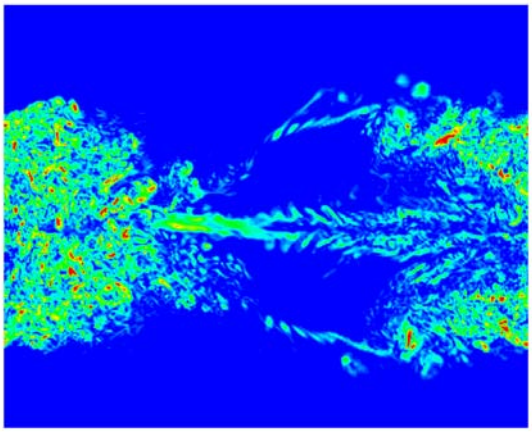

Figure 2-22 Iso-vorticity contours just before the second 'turn-around' time.

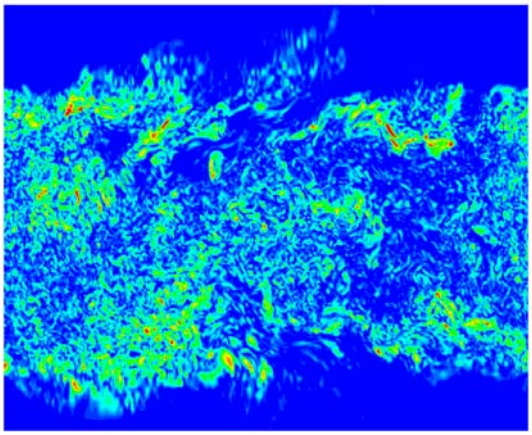

Figure 2-23 Iso-vorticity contours after the second 'turn-around' time.

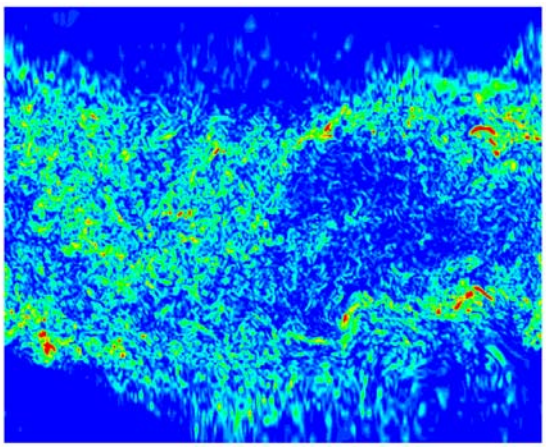

Figure 2-24 Iso-vorticity contours in the final stage.

When the wake flow passes through the rotor the second time (cf. Figure 2-23), it starts to develop broad-banded turbulence superposed organized vortex structures. In the final stage it is difficult to distinguish the various structures (cf. Figure 2-24), although the influence of the rotor on the wake immediately downstream is still visible. The smallest length scales are here determined by the size of the computational grid, whereas the largest length scales are determined partly by the diameter of the rotor and partly by the length of the computational domain, corresponding to the distance between the turbines.

After the transients have died out, the flow becomes dominated by the development of turbulence. Due to the mixing by the rotor, turbulent kinetic energy is continuously added to the flow, and statistics can be performed when the production of turbulence is in balance with the dissipation. When this happens the flow is *statistically stationary*, and usual statistical tools can be applied. In the following we compute Reynolds stresses and turbulence intensities in a cross-section located one diameter upstream the "last" rotor in the final stage situation (cf. Figure 2-24), where the turbulence is considered fully developed. To illustrate the results, we depict iso-surfaces of the temporal correlation tensor

$$R_{ij} = \frac{1}{n}\sum_{k=1}^{n}\left(u_i(t_k)-\overline{u}_i\right)\left(u_j(t_k)-\overline{u}_j\right), \tag{2-22}$$

corresponding to (a normalized version of) the Reynolds stress tensor. Strictly speaking, the Reynolds tensor is defined as $R_{ij} = -\rho\overline{u_i'u_j'}$, but for convenience we omit the minus, and the density ρ in the expression. In equation (2-22) n denotes the number of snapshots used for the time-averaging, u_1 denotes the along wind turbulence component in a Cartesian coordinate system (in the succeeding also denoted u), u_2 denotes the transversal turbulence component (in the succeeding also denoted v), and u_3 denotes the vertical turbulence component (in the succeeding also denoted w). In the present work n = 750.

In Figure 2-25 - Figure 2-30 we show iso-surfaces of the Reynolds stresses. It is seen that the normal stress in the main flow direction is the dominant component, attaining approximately twice as large values as those in the plane perpendicular to the main flow

direction. The shear stresses (cf. Figure 2-28 - Figure 2-30) are even smaller, taking values in the order of 1% for in-plane components and 4% for the values correlating in- and out-plane shear stresses. It is also important to note that the shear stresses are very small inside the wake, whereas big values are to be found in an annular domain surrounding the blade tips in agreement with the experimental observations in Section 3.2.5. This indicates that when the rotors are located on a common axis, the main mechanism for generating turbulence is provided by the mixing caused by large wake shear gradients and by the development of the tip vortices.

In Figure 2-31 and Figure 2-32 we show the normalized time-averaged axial- and azimuthal velocity fields, respectively. A distinct wake structure is seen with a shear layer in a ring enclosing the tips. The mean normalized axial velocity attains a value of about 0.4 at the hub height, corresponding to 40% of the ambient velocity.

Defining the along-wind standard deviation of the turbulent wind speed fluctuations as

$$\sigma_{uu} = \sqrt{R_{11}} \ , \tag{2-23}$$

the turbulence intensity is defined as

$$I_{wake} = \sigma_{uu} / U_h \ , \tag{2-24}$$

where U_h denotes the mean wind speed at hub height. In Figure 2-33 we depict the turbulence intensity as it is usually defined for wind loadings on stand-alone wind turbines, i.e. with the denominator referring to the ambient wind speed. However, inside a wind farm this should be referred to the local wind speed at hub height. With a mean axial velocity at hub height of 40% of the ambient velocity, the turbulence intensity values are to be multiplied by 2.5 in order to compare it to measured values within a wind farm. Thus, the turbulence intensity is found to vary from zero to 45%, with an average value of 20-25%. Based on measurements and analytical considerations, and depending on operating conditions, Frandsen [44] reports comparable values for a wind farm with a rotor spacing of 3 diameters.

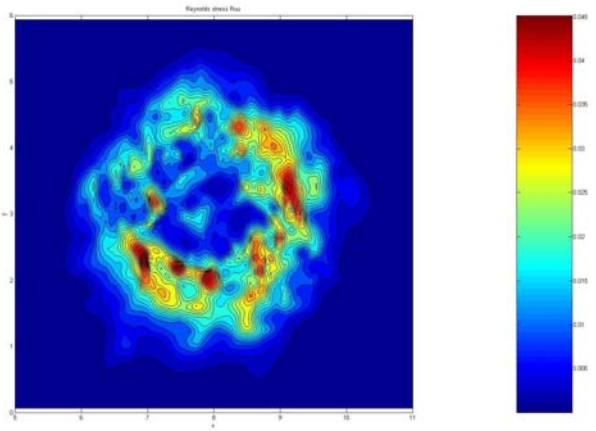

Figure 2-25 Reynolds stresses R(v,v). Minimum value equal to 0; Maximum value equal to 4.5%.

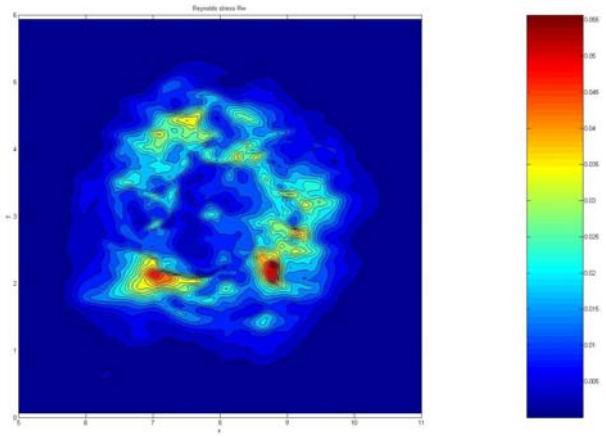

Figure 2-26 Reynolds stresses R(w,w). Minimum value equal to 0; Maximum value equal to 5.5%.

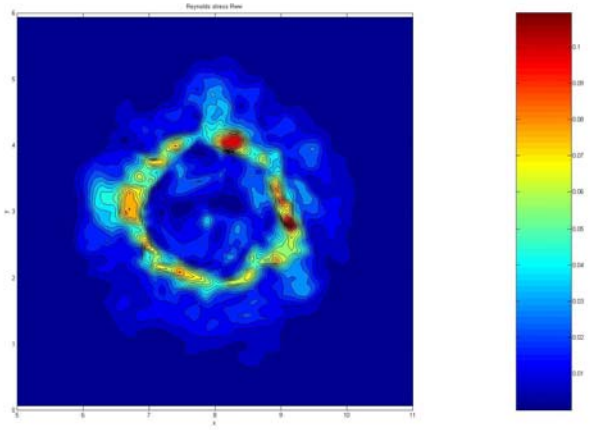

Figure 2-27 Reynolds stresses R(u,u). Minimum value equal to 0; Maximum value equal to 11%.

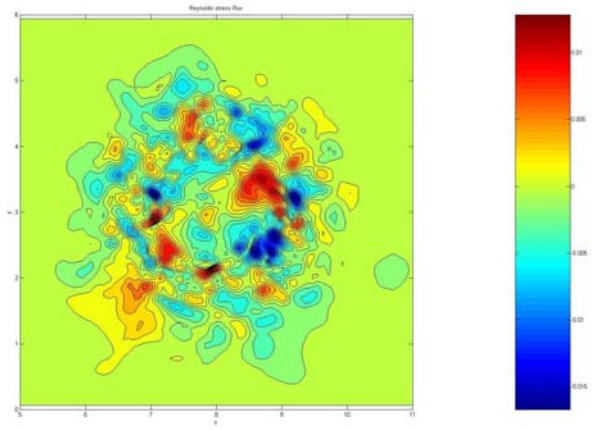

Figure 2-28 Reynolds stresses R(v,w). Minimum value equal to -1.6%; Max. value equal to 1.2%.

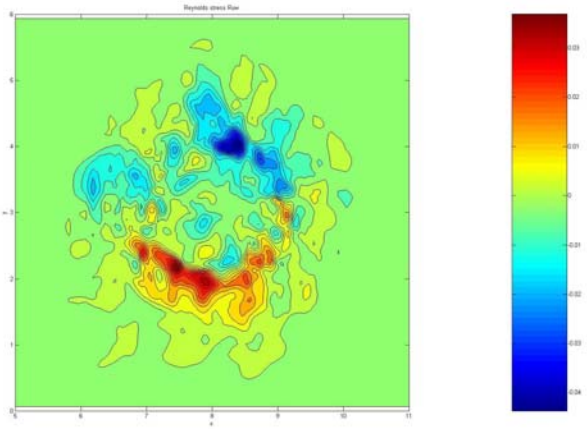

Figure 2-29 Reynolds stresses R(v,u). Minimum value equal to -4.3%; Max. value equal to 3.6%.

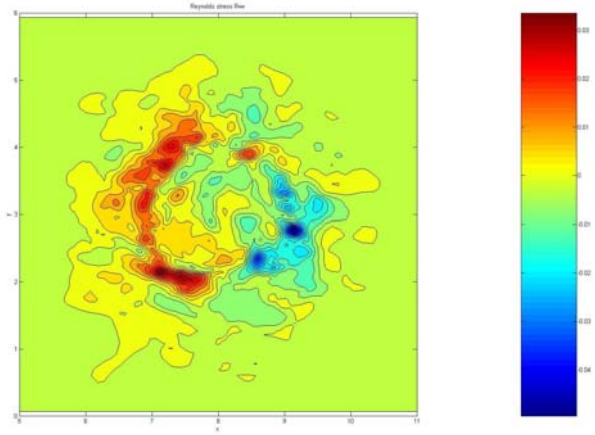

Figure 2-30 Reynolds stresses R(w,u). Minimum value equal to -4.9%; Max. value equal to 3.2%.

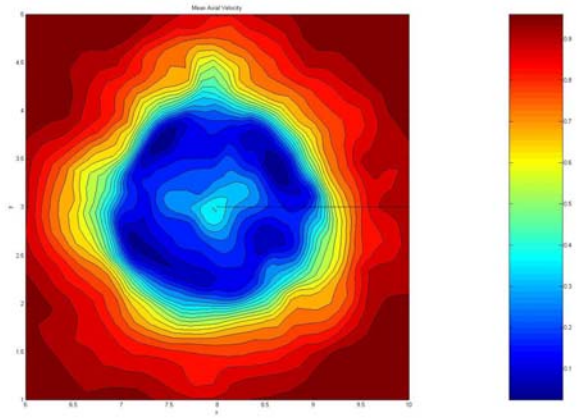

Figure 2-31 Mean axial velocity component. Min. value equal to 0; Max. value equal to 1.

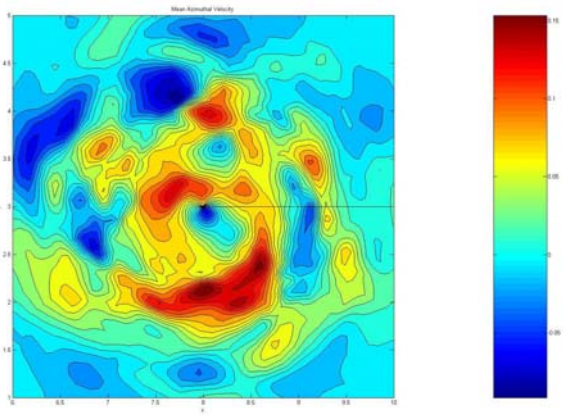

Figure 2-32 Mean azimuthal velocity component. Min. value equal to -0.1; Max. value equal to 0.15.

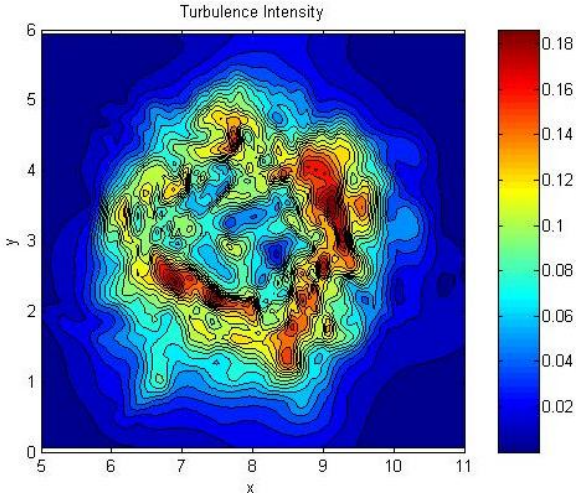

Figure 2-33 Turbulence intensity made dimensionless by ambient velocity. Min. value equal to 0; Max. value equal to 0.18. All values are to be multiplied by 2.5 when referring to the wind speed at hub height.

Apart from the turbulence intensity, an essential characteristic of turbulent flows is the turbulence spectrum. Whereas the turbulence intensity describes the "strength" of the turbulence, the turbulence spectrum quantify the structure of the turbulence. Both characteristics are significant for wind turbine loading. The turbulence spectrum is defined as the Fourier transform of the correlation function given in equation (2-22), and thus expresses the turbulence energy distribution on frequencies.

In an attempt to roughly quantify the structure of the wake generated turbulence, caused by the combined effect of blade bound circulation and the mechanically generated turbulence contribution arising from the wake shear, we have computed selected turbulence spectra in the flow regime behind a *single* turbine. The spectra have been determined using *spectral averaging* in the azimuthal direction for a given flow radii specification. This is possible because the rotor is symmetric, and the inflow is uniform. The highest time scale that can be resolved corresponds to the smallest length scale resolved (i.e. the grid cell size). Spectra of the *axial turbulence component*, associated with seven different radii (i.e. r/R = i×0.25, i = 0,…, 6; with r being the radial coordinate) have been computed for U_0 equal to 6 and 10 m/s, respectively.

Figure 2-34 - Figure 2-36 show the computed normalised spectra for the 6 m/s case at three different downstream distances from the wake generating turbine. The considered downstream distances are 7, 10 and 13 rotor radii, respectively.

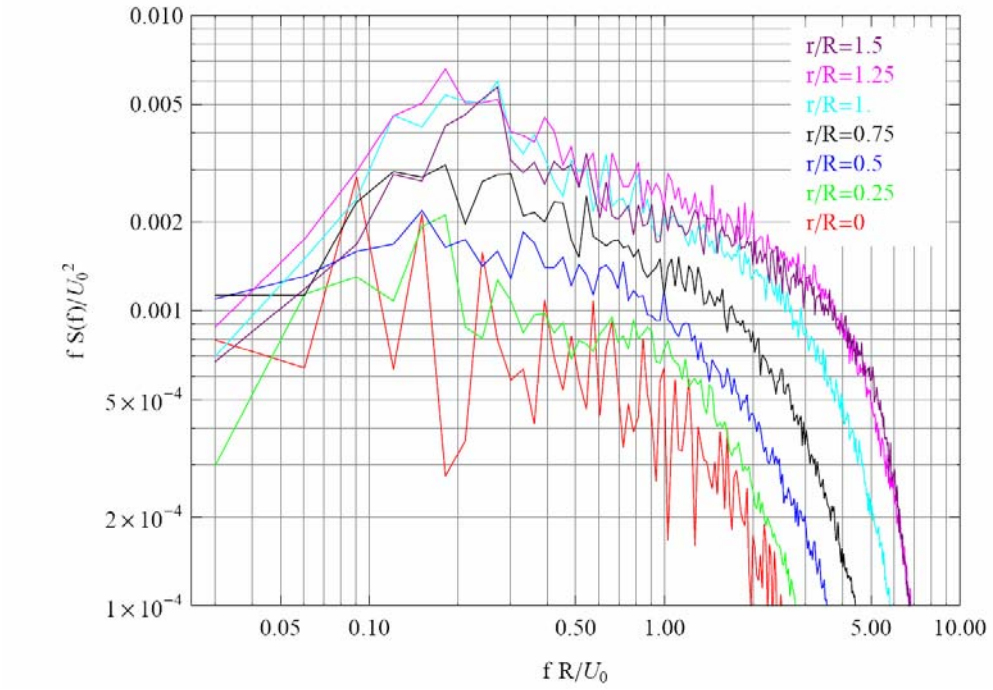

Figure 2-34 Spectra of the axial velocity component 7 rotor radii downstream the turbine operating in a uniform inflow. The different radial positions are indicated in the figure legend.

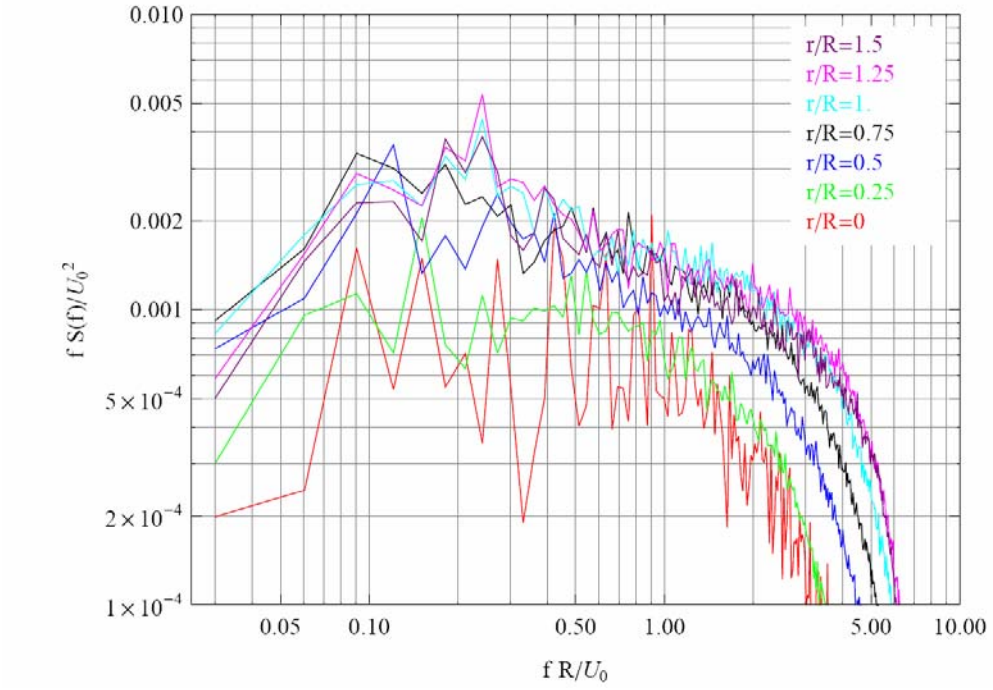

Figure 2-35 Spectra of the axial velocity component 10 rotor radii downstream the turbine operating in a uniform inflow. The different radial positions are indicated in the figure legend.

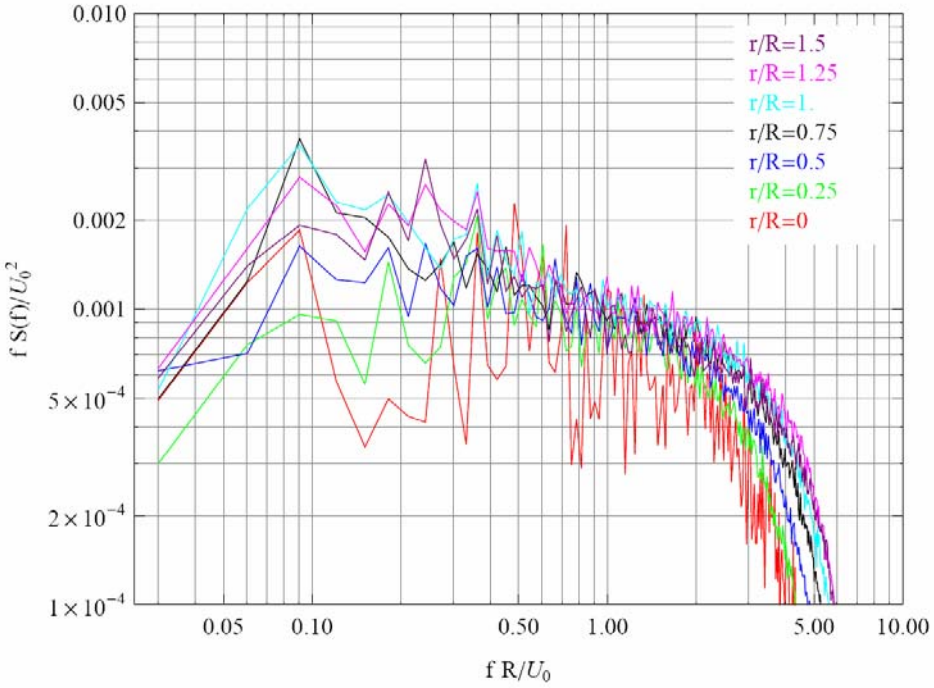

Figure 2-36 Spectra of the axial velocity component 13 rotor radii downstream the turbine operating in a uniform inflow. The different radial positions are indicated in the figure legend.

The spectra is typically composed of an *energy-containing sub-range* characterized by low frequency components of limited statistical significance, an *inertial sub-range* with a spectral gradient close to –2/3 in agreement with the theoretical expectation[2], and a *dissipation sub-range* which, in the case of these numerically based spectra, is resulting from the limited spatial resolution as well as from numerical diffusion. Another general feature of the spectra is, that the spectral estimates associated with the radial position r/R = 0 is somewhat more "noisy" that the spectra associated with the other investigated radial positions. This is due to the applied azimuthal spectral averaging, resulting in no spectral averaging for the radial position r/R = 0.

Comparing spectra, associated with the various investigated radial positions in Figure 2-34 - Figure 2-36, it is characteristic that the turbulence has the largest content of energy in the wake region associated with the highest gradient of the wake deficit (in agreement with the results presented in Figure 2-27 and Figure 2-33 for the multiple wake situation). It is furthermore characteristic that the wake turbulence attenuates and tend to be more spatial homogeneous with increasing downstream distance as expected. Finally, it can be noted that, at the investigated downstream stations, no traces of organised rhythmic flow structures are observed (cf. also Figure 2-14).

Turning to 10 m/s load case, Figure 2-37 and Figure 2-38 show the computed spectra 10 and 13 rotor radii downstream the wake generating turbine.

2 In the *inertial sub-range*, the spectrum decays linearly with a gradient equal to -5/3 in a double logarithmic depiction – the spectrum multiplied by frequency thus decays with a gradient equal to -2/3.

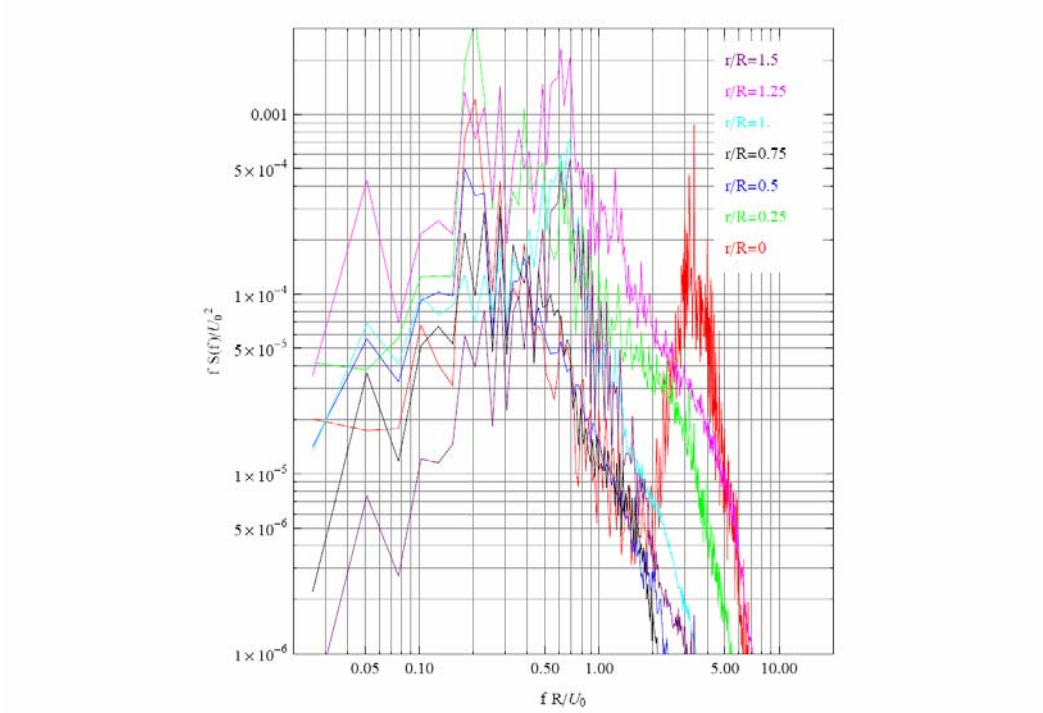

Figure 2-37 Spectra of the axial velocity component 10 rotor radii downstream the turbine operating in a uniform inflow. The different radial positions are indicated in the figure legend.

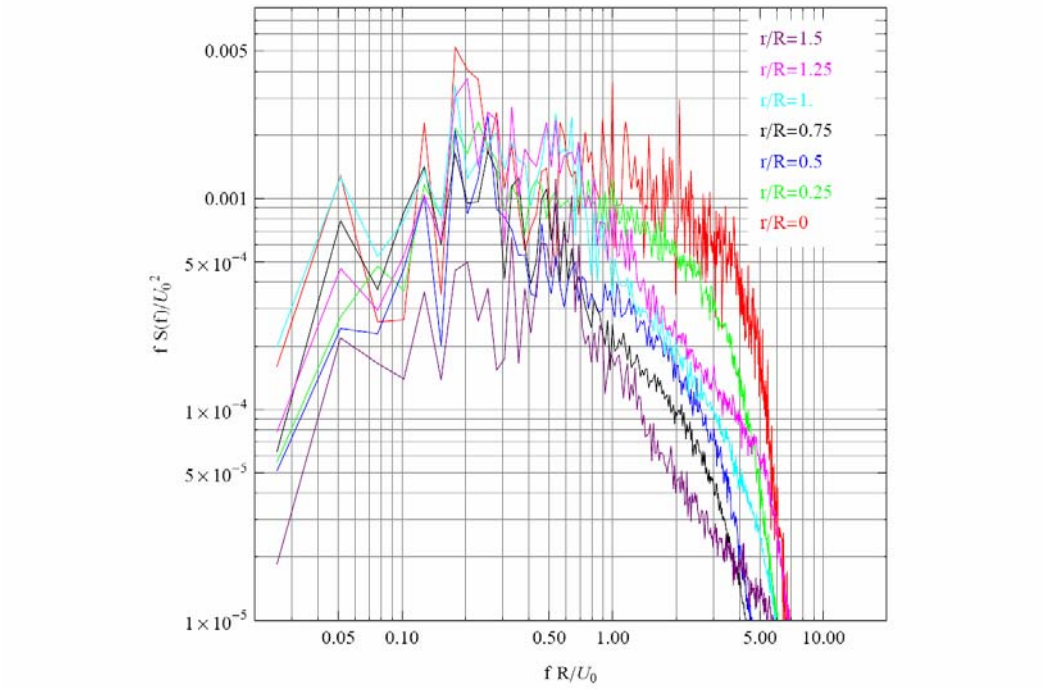

Figure 2-38 Spectra of the axial velocity component 13 rotor radii downstream the turbine operating in a uniform inflow. The different radial positions are indicated in the figure legend

Because of the higher inflow velocity, the break down of rhythmic flow structures, and subsequent formation of the turbulence, is somewhat retarded for the 10 m/s case compared to the 6 m/s load case when referred to downstream distance. It is moreover notable that the spectral energy content, when normalised with the inflow velocity squared, is less than observed for the 6 m/s load case. This is due to the turbine being aerodynamically more "transparent" for larger inflow velocities.

The spectrum shown in Figure 2-37 illustrates a situation where the wake turbulence is yet not fully developed (cf. Figure 2-14). This manifest itself in the lack of an inertial sub-range regime as well as in the presence of a narrow banded energy peak in the normalized frequency range 2-5 for the radial position r/R = 0, which reflects the presence of rhythmic hub vortex flow structures.

Figure 2-38 illustrates a situation where the wake turbulence is somewhat more developed. An inertial sub-range can be identified in the spectrum – at least for the inner radial stations defined by r/R = 0 and r/R = 0.25 – and the no traces of rhythmic flow structures is observed. In analogy with the observations for the 6 m/s case, the wake turbulence field has an inhomogeneous character but, contrary to the 6 m/s case, with the bulk of energy concentrated in the spatial regime close to the wake centre. This is presumably related to the turbulence not yet being fully developed – the inertial sub-range is e.g. only partly formed and practically not existing in case of the outer radial stations.

Both the spatial distribution of the turbulent energy over the wake regime and the distribution of the turbulent energy on the various turbulence eddy sizes are of interest from a wake loading point of view. The *turbulence length* scale is a convenient scalar parameter for characterization of the "dominating" turbulent eddy sizes. In the following we will analyze the turbulence length scales associated with the spectra resulting from the 6 m/s case, where the wake turbulence is considered fully developed.

For this purpose, we will use the (one-sided) Kaimal spectrum as the generic spectrum to which the observed spectra will be fitted. The Kaimal spectrum, $S_k(f)$, is defined in a number of different, but equivalent, ways in the literature, and here the definition adopted in the IEC code [51] is used, i.e.

$$S_k(f) = 4\sigma^2 \frac{L_k / U_0}{\left(1 + 6fL_k / U_0\right)^{5/3}}, \tag{2-25}$$

where σ is the standard deviation of the turbulence component in question, U_0 is the mean free-stream velocity, f is the frequency in Hz, and L_k is the turbulence length-scale.

Expression (2-25) has been fitted to each of the available wake spectra by adjusting the standard deviation as well as the length scale to obtain the least possible deviation between generic- and observed spectra in the frequency range excluding the dissipation sub-range. An example of a fit is shown in Figure 2-39, where the vertical green line indicates the estimated transition between the inertial sub-range and the "numerical dissipation" sub-range that have been used in the fitting procedure.

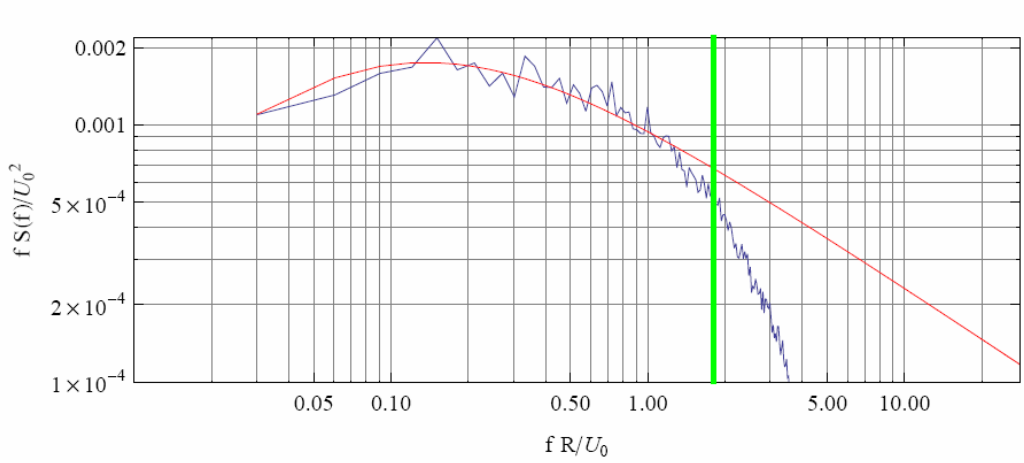

Figure 2-39 Kaimal spectrum fitted to the observed spectrum associated with radial position r/R = 0.5 at downstream distance 7D.

The results from these fits are summarized in Figure 2-40 and Figure 2-41 showing the normalized wake generated variance and the normalized Kaimal length scale, respectively, as function of radial position and downstream distance.

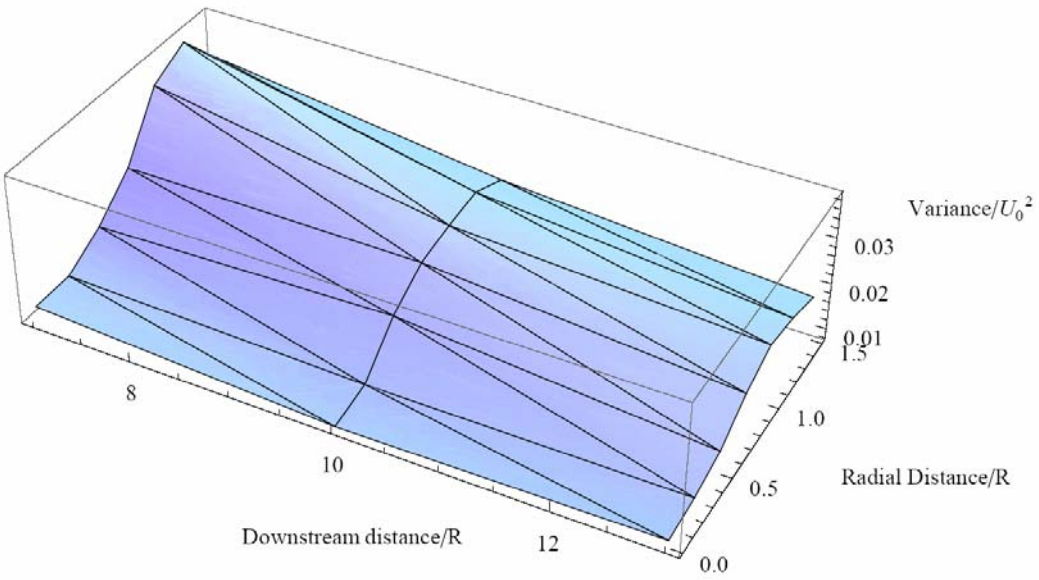

Figure 2-40 Normalised wake generated variance as function of radial position and downstream distance.

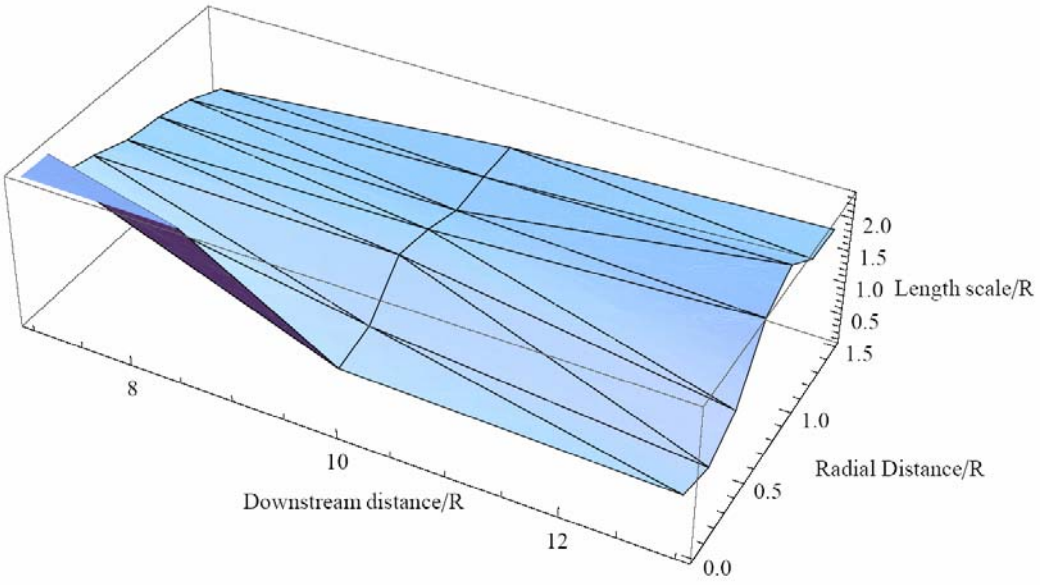

Figure 2-41 Normalized wake generated variance as function of radial position and downstream distance.

Figure 2-40 displays the previously noted features - i.e. that the wake generated turbulence has the largest content of energy in the wake region associated with the highest gradient of the wake deficit (in agreement with the full-scale experimental observations shown in Figure 3-14), and that the wake turbulence attenuates and tend to be more spatial homogeneous with increasing downstream distance.

The variation of the turbulence length scale with downstream distance and radial position, as shown in Figure 2-41, is modest and without a clear trend. A characteristic size of the estimated wake turbulence length scale is 1.5R, with the length scale associated with radial position r/R = 0 at downstream distance 7R being the only exception. This length scale is approximately twice as large as the estimated characteristic size which, however, is believed to be related to the particular realization of the low frequency spectral regime of this spectrum. In this respect it is noted, that contrary to other radial positions, the statistical significance of the spectral estimates associated the radial position r/R = 0 is suffering from the lack of spectral averaging.

We will finally use the above analysis to give a qualitative indication of the size of the wake generated turbulence length scale compared to a characteristic turbulent length scale associated with atmospheric boundary layer. For this purpose we take the characteristic length scale, associated with atmospheric turbulence, as the (Kaimal) length scale specified in the IEC code [51] as

$$L_k = 8.1L \; ; \; L = \begin{cases} 0.7 \cdot y & y \le 30m \\ 21m & y > 30m \end{cases} \tag{2-26}$$

with y denoting height above ground level. For a large modern wind turbine, with a rotor diameter of 100 m, the length scale of the atmospheric turbulence will thus be of the order 2.5 times the length scale of the wake generated turbulence. For smaller turbines, the difference in atmospheric- and wake length scales will be even more pronounced.

2.3.3 Wake turbulence simulation

For wind turbine design purposes full 3-D CFD computations of design wind fields, consisting of wake generated turbulence contributions superimposed on the ambient atmospheric turbulence field, is yet not a feasible approach. This is basically due to computational limitations. Whereas work is progressing on CFD modeling of the atmospheric boundary layer [78], inclusion of a wind turbine rotor in such computations is hindered because an extreme number of cells in the computational domain is required – even when based on the actuator line approximation described in Section 2.3.2, where a detailed resolution of the viscous boundary layer around of the individual rotor blades is avoided.

This is because of the eddy-diffusivity approximation used in most CFD computations (RANS as well as LES closures) to model the atmospheric turbulence. For high Reynolds number flows, such as atmospheric boundary layer flows, the eddy-viscosity is correspondingly high. This level of eddy-viscosity is, however, too high compared to the level required for the lower Reynolds number rotor flow, and incompatible flow conditions thus results. Basically, the problem of simulating the full atmospheric wind field with a wind turbine rotor embedded is due to the difference in Reynolds numbers which, however, can be solved using a huge number of grid points. The situation is further complicated by the fact that rotor and wake flow interacts through the wind turbine control system. As a consequence of the above considerations, alternative CFD methods, that are less dependent on the eddy-diffusivity closure, are necessary.

As a consequence of the above considerations, presently alternative more engineering types of algorithms for generation of design wind fields has to be exploded. The first step in approaching simulation of wake generated turbulence, based on such a strategy, is to characterize the turbulence fields in question. Basically, this characterization can be performed using experimental- and/or numerical investigations (cf. Section 2.3.2 and Section 3.2.5). As for the numerical approach it is noted that a simplifying *decomposition* of the wake generated turbulence and the turbulence associated with the atmospheric boundary layer is required for the aforementioned reasons.

Having gained insight in the character of the wake turbulence it is obvious that this turbulence field is neither stationary, nor homogeneous. In addition, the turbulent flow may even, to some extend, be characterized by organized motions caused by e.g. tip vortices. Therefore, the conventional models [33], [45] for generation of ambient turbulent flow fields in a wind turbine context are not directly applicable for wake turbulence generation. Two possible alternatives are discussed in the following. The *first* alternative is based on Proper Orthogonal Decomposition (POD), where the dominant structures are extracted from a flow, and subsequently used to construct low-dimensional models that are able to describe the principal flow dynamics with a limited number of modes. The *second* alternative is a spectral approach that, based on prescribed wake turbulence characteristics, is able to generate second-order-consistent spatially inhomogeneous and in-stationary turbulence fields.

Whereas the POD approach in principle can be used to extrapolate available flow field information, by projecting Navier-Stokes equations on the extracted POD-modes, cautiousness should be observed in this respect, and presently only an *interpolation* application can be recommended with this method. For the spectral approach, the limitations are primary associated with lack of thorough information on the characteristics of wake generated turbulence fields, including the influence of tip vortices in the wake near field.

Proper Orthogonal Decomposition

POD has mostly been used to analyze experimental data, but with the rapid development of computer technology, it is now also largely used to analyze numerical data. In the present work POD is employed to analyze and model the dynamics of the dominant flow structures in the wake. Several versions of the POD technique exist, and in the present analysis the so-called *snapshot* POD is applied. There exist a vast amount of literature on the theory and the use of POD in fluid mechanics. Here we will only briefly outline the ideas behind POD. For a more thorough introduction we refer to the review article by Berkooz et al. [46] or the text book by Holmes et al. [47].

In the snapshot method data sets consisting of snapshots of the velocity components are arranged in vectors

$$\widetilde{V}^k = \left[u,v,w\right]^k \ , \ k = 1,2,\ldots,n \ ,$$

where n denotes the number of snapshots. Next, subtracting the time-average,

$$\overline{\widetilde{V}} = \frac{1}{n}\sum_{k=1}^{n}\widetilde{V}^k \ ,$$

from $\widetilde{V}^k$, we get vectors, V^k, containing only the fluctuating part of the velocities. From these vectors the covariance matrix is computed as

$$C_{ij} = V^i V^j \ ,$$

which is obviously a $n \times n$ matrix. Solving the eigenvalue problem for C_{ij} results in a set of eigenvectors, ψ^k, from which a normalized orthogonal basis can be determined as follows

$$\phi^k = \frac{\sum_{i=1}^{n}\psi_i^k V^i}{\left\|\sum_{i=1}^{n}\psi_i^k V^i\right\|} \ ,$$

where ψ_i^k denotes the $i'th$ component of the vector ψ^k. This basis of vectors is referred to as *modes*. The eigenvalue λ_k, corresponding to the eigenvector ψ^k, represents the energy contained in the corresponding mode. Therefore, by ordering the eigenvalues as $\lambda_1 > \lambda_2 > \ldots > \lambda_m > 0$, the first modes are the most dominant, and represent the most energetic structures in the flow, and the following modes gradually become less and less significant.

The amplitudes, $a_k(t)$, of the POD modes can be found by projection of the velocity field on the basis modes

$$\underline{\underline{A}} = \underline{\underline{\Phi}}^T \underline{\underline{U}} \ ,$$

where $\underline{\underline{A}}$, $\underline{\underline{\Phi}}$, and $\underline{\underline{U}}$ are matrices containing the a_k, φ^k, and V^k vectors column wise, respectively. Having determined the amplitudes of the modes, a given snapshot can then be reconstructed from

$$\tilde{V}\left(\vec{x},t^n\right) \approx \overline{\tilde{V}}\left(\vec{x}\right) + \sum_{k=1}^{m} a_k\left(t^n\right)\varphi^k\left(\vec{x}\right), \tag{2-27}$$

where m denotes the number of modes included in the reconstruction of the flow, and t^n is the time instant associated with a given snapshot.

There are several ways to determine the velocity field at an arbitrary time instant, t. One is to replace the temporal development of the amplitude functions, a_k, by spline functions, $\tilde{a}_k$, resulting in the following expression for the evolution of the turbulent velocity field:

$$\tilde{V}\left(\vec{x},t\right) \approx \overline{\tilde{V}}\left(\vec{x}\right) + \sum_{k=1}^{m} \tilde{a}_k\left(t\right)\varphi^k\left(\vec{x}\right). \tag{2-28}$$

Another method is to use Galerkin projection to derive a low-dimensional system of ODE's by projecting the equations of motion, i.e. the Navier-Stokes equations, on the modes given by a continuous form of equation (2-27). This result in the following generic form of the low-dimensional model (see [48] and [49]):

$$\frac{\mathrm{d}a_i}{\mathrm{d}t} = \alpha_i + \beta_{ij}a_j + \gamma_{ijk}a_j a_k \ , \tag{2-29}$$

where $i = 1,2,...,m$, and the Einstein summation rule is employed. The coefficients $\alpha_i, \beta_{ij}, \gamma_{ijk}$ are determined either by discretizing the flow equations or by solving the inverse problem using a series of snapshots to determine a_i and the associated derivatives. In the present work both strategies have been followed. However, as the determination of the coefficients in (2-28) results in the solution of an over-determined system of equations, it does not have a unique solution. As a result, the system of equations tends to become very stiff, and rather small time-steps had to be employed. Work is still in progress to ameliorate the technique.

To illustrate the appearance of the POD modes we depict some representative samples in the following. In Figure 2-42 - Figure 2-45 we show the velocity fields of POD modes no. 1, 2, 3, and 8, respectively. These modes represent 20%, 15%, 9%, and 3% of the total turbulent energy, respectively. Using e.g. the first 10 modes results in 90% of the turbulent energy being captured, whereas 98% is captured when increasing the number of modes to 20. This illustrates that only a relatively small number of POD modes are needed to reconstruct the computed turbulent flow field. A future application of this technique is to combine it with engineering BEM codes for obtaining turbulent inflow conditions to aeroelastic computations.

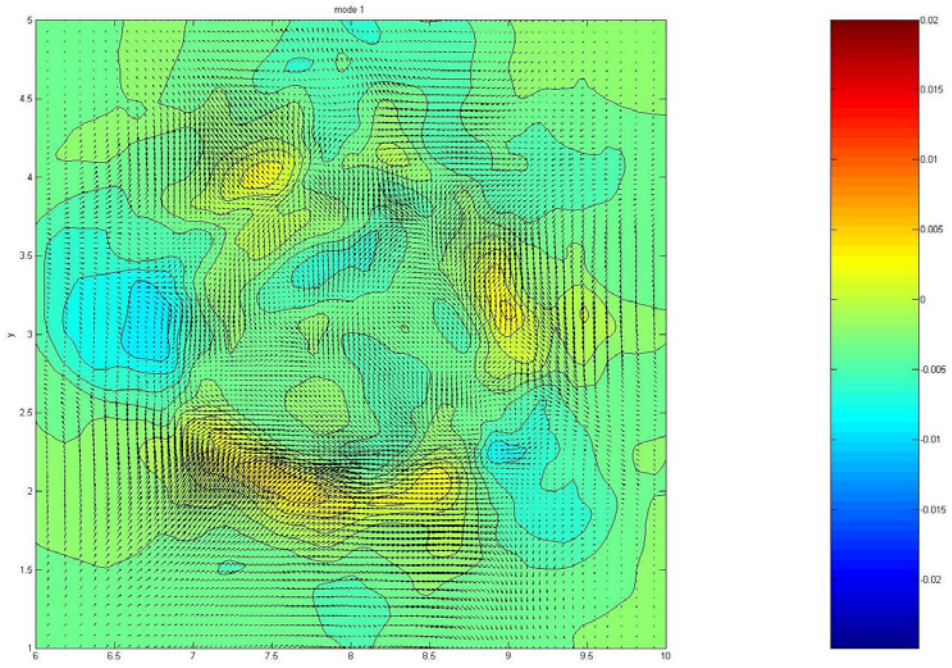

Figure 2-42 Velocity field of POD mode no. 1.

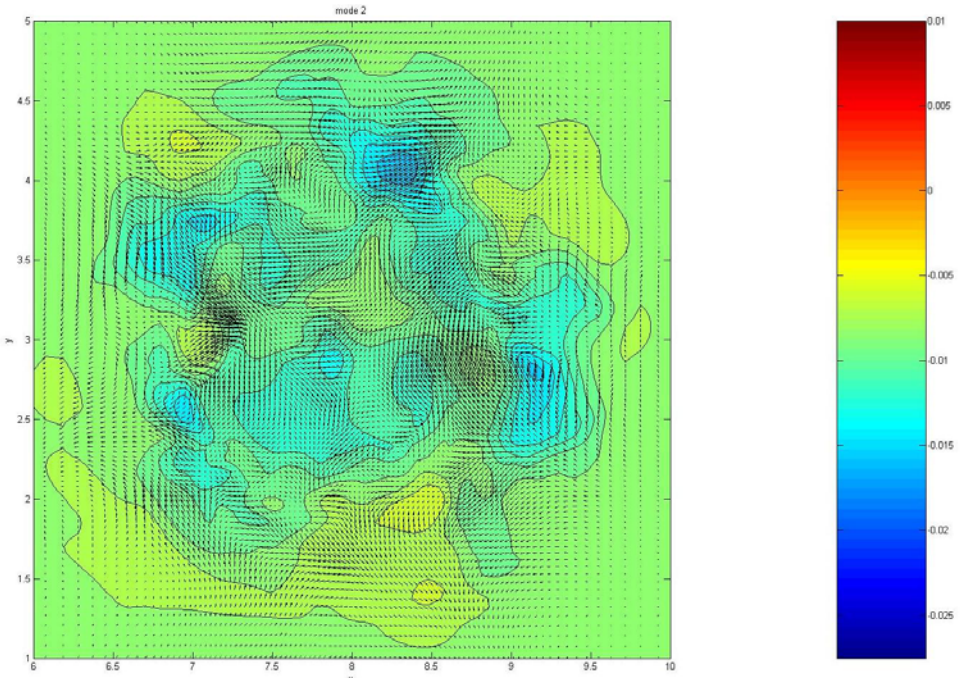

Figure 2-43 Velocity field of POD mode no. 2.

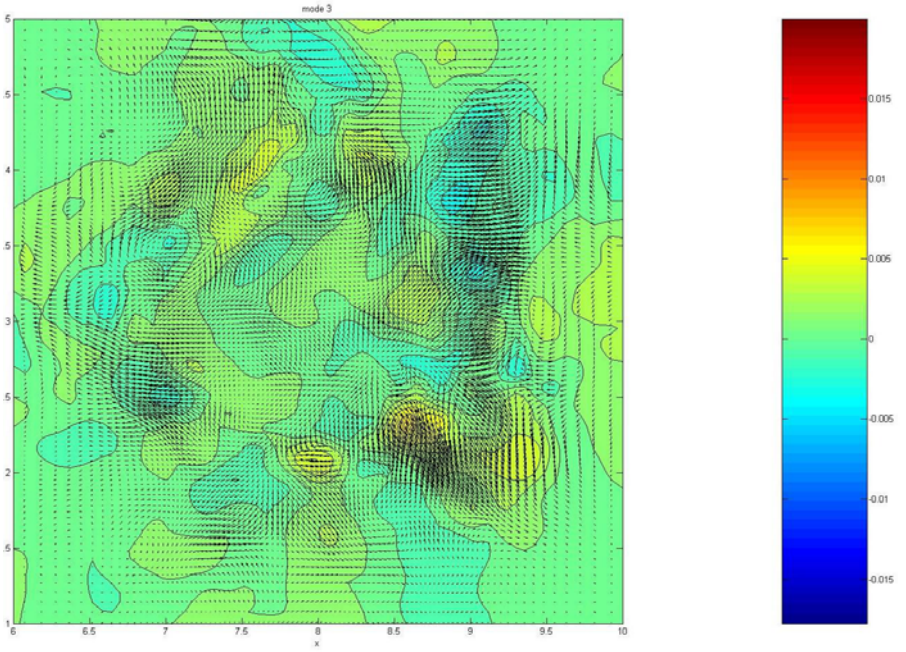

Figure 2-44 Velocity field of POD mode no. 3.

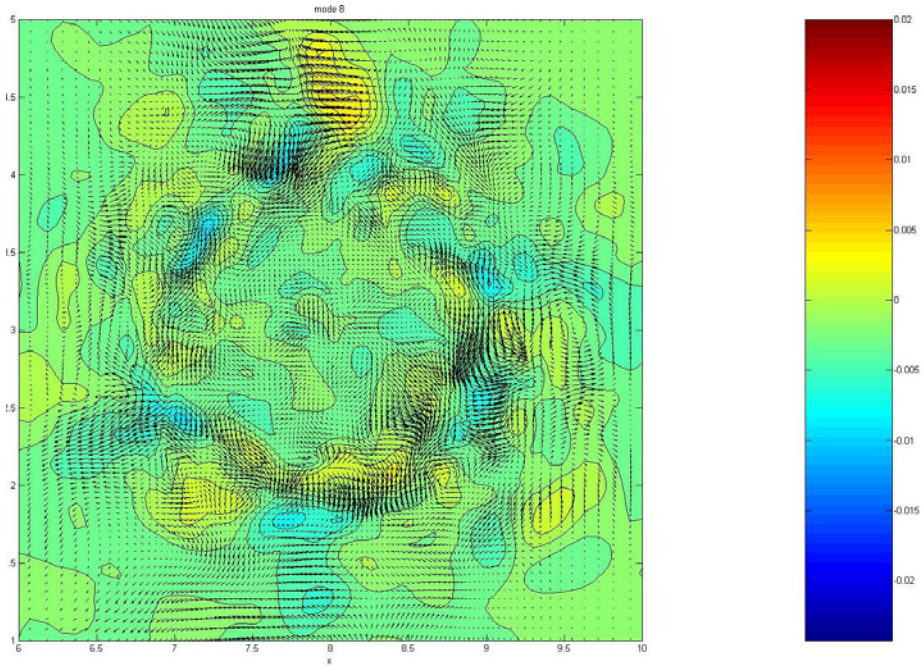

Figure 2-45 Velocity field of POD mode no. 8.

Spectrum based methods

The turbulent wind field on the turbine rotor is needed as input for load simulation programs [50]. This field is difficult to measure with sufficient spatial resolution, and it is usually simulated by a separate simulation tool. The IEC code on turbine safety [51] recommends two methods for this. The most common one [52], which in the context of wind energy often is referred to as Veers' method [53], is to simulate a multitude of correlated time series at points distributed on the area swept by the turbine rotor. The alternative Mann's method [54] simulates only three turbulence components, however in a three-dimensional spatial domain, and time-dependent velocity perturbations are found by advection of the 'frozen-turbulence' field by the mean wind. Mann's method has been extended for flow over real topography with changing surface roughness [55] and coupled with a flow model [56].

Both simulation methods generate homogeneous, stationary, Gaussian turbulence fields, which is unrealistic for wake turbulence. If two turbines are not perfectly aligned after the wind direction, only part of the wake from the upwind turbine hits the downwind one. This introduces cyclic variations of both mean and turbulent load as the blades of the downwind turbine pass in and out of the wake. In the following we discuss extensions of Veers' method [53] suitable for wake turbulence simulation. A more detailed version can be found in [62].

Basic Gaussian simulation

The general idea of multivariate Fourier simulation is first to generate Fourier components with proper statistics and subsequently convert them into time series by inverse FFT. This procedure is actually a *linear* combination of stochastic variables, and the result will remain Gaussian if the input is. The correlation matrices of the Fourier components are known to be Hermite symmetric, which can be 'square-root' factorized by applying Choleski decomposition. Gaussian Fourier components with prescribed correlation is generated from a vector of random independent complex Gaussian variables and multiplied by this 'square-root' matrix. The computational work of the Choleski algorithm is proportional to the cube of the number of time series, which usually is large in turbine-load applications. The frequency dependence is, however, quite smooth, and it is a good approximation to perform the computationally expensive Choleski decomposition at a reduced set of frequencies, say five per decade, and interpolate between the results.

Non-Gaussian simulation

A simple way to simulate non-Gaussian time series is first to simulate auxiliary Gaussian time series, and then to transform each of them by a mapping function defined by their target probability distributions [79]. It is possible to calculate how these transformations distort the correlation of the simulated time series, and this has inspired the algorithm called *correlation distortion* [80]. The procedure is:

- first to find the correlations of the auxiliary processes, which produces the right correlations of the transformed processes;
- then find the cross spectrum of the auxiliary Gaussian processes by FFT;
- then Fourier simulate auxiliary Gaussian series; and
- finally to transform these into non-Gaussian series.

Direct computation of the correlation distortion function is computationally expensive, as it involves evaluation of a double integral for all combinations of time series and all time lags. Considerably improvement is achieved by a serial expansion of the mapping functions based on Hermite polynomials. The trick is that these polynomials are *orthogonal* with the

Gaussian distribution, and once the coefficients of each expansion are evaluated, in general by one-dimensional integrals, all correlation-distortion functions are determined. For a weakly non-Gaussian process the calculations are even faster, as the correlation-distortion coefficients can be determined by the skewness and kurtosis of the target series [57]. A difficulty of the method is that the range of correlation for the non-Gaussian series is limited [80], since we cannot at the same time expect high correlation and very different probability distributions of two processes.

Simulation by the correlation-distortion method produces time series with correct probability distributions and cross-spectral relations, but they may still differ from measurements. The probability of the time-derivative of the simulated series will, for instance, always be symmetric, whereas time derivatives of measurements may be asymmetric. It is possible to simulate a series with non-Gaussian increments by correlation distortion, integration, and adjustment of mean values [59].

Conditional simulation

Conditional Fourier simulation is an extension of the methodology where a subset of the process has been measured, e.g. by a few sensors on a mast, and the rest of them are simulated with prescribed correlation. In contrast to Fourier simulated series, measured time series are rarely cyclic, so a buffer zone with artificial data forcing the input to be cyclic is introduced. Time series of extended duration are simulated, but only the first part matching the duration of the observations is presented. If the system is non-Gaussian, the input series are transformed to Gaussian auxiliary series by the inverse of the usual mapping function. In any case the input is FFT transformed to find the Fourier components of the extended cyclic observations. For each frequency, the equations relating uncorrelated Gaussian input to correlated Fourier components are rearranged for conditional simulation of processes, which have not been measured. Finally, the processes are transformed to time domain by inverse FFT and translated to non-Gaussian series if necessary. With this method, the simulated series are forced toward the measured signals at close distance and low frequency. Conversely, the finer details of the simulated series will be more random and follow the postulated stochastic model far from the measurement points.

Non-stationary simulation

A set of non-stationary time series is described by *time-dependent* probability distributions, spectral relations, correlation-distortion mapping functions, etc. Note, however, that the actual estimation of such time varying statistics, in an ensemble-average sense, is considerably more difficult than for stationary processes, since we cannot rely on ergodicity of the processes and thereby apply time averaging directly in the evaluation of the statistical parameters. The interpolation between the evolving model parameters can be modelled by Bezier splines [60] and, although the interpolation is smooth, it is a *linear* combination of values at Bezier reference states and auxiliary control points. Therefore we can produce a non-stationary simulation by linear combination of steady-state Fourier simulations using parameters for reference states and control points, provided that the uncorrelated Gaussian input vectors for each steady-state simulation are *identical* [59]. The Bezier interpolation parameter could be time, but for a system switching back and forth between well-defined states, it is more efficient to use a control parameter to describe the system.

Wake turbulence simulation

Wake turbulence is a case for multivariate Fourier simulation with the extensions described above. The wind field is non-homogenous with lower mean wind speed and higher turbulence inside the wake, and the vigorous mixing may result in a non-Gaussian probability distributions. It is further anticipated that the extra turbulence production results in more isotropic turbulence with shorter length scale (cf. Section 3.2.5). Wake turbulence is probably both added at frequencies corresponding to the sizes of the tip vortices and eddies produced by radial velocity shear. The high-frequency part of the spectra will probably follow the inertial sub-range law, but with higher dissipation rate than in the ambient case. We still lack precise wake turbulence models and can only guess about spectral coherence inside wakes.

Turbulence meander, as observed behind the Tellus turbine (cf. Section 3.1.6), calls for a non-stationary simulation tool. It seems natural, first to formulate a stochastic model in a moving frame of reference relative to the instantaneous wake centreline, and then prescribe turbulence statistics at the grid points on the turbine rotor depending on centre-line position. With a measured or simulated time series of centre-line positions, we then simulate the inhomogeneous, non-stationary, and perhaps non-Gaussian time series.

It is suggested to simulate random centreline positions by kinematic simulation [63]. With this method large-scaled turbulence fields are simulated by Mann's method [54] simplified to lateral- and vertical dimensions only (cf. Section 2.2) and with moderation of the 'frozen turbulence' approximation introducing evolution of the random Fourier components with time scales depending on wave numbers. The meandering wake is simulated as a trace of wakes continuously released the operating turbine(s), and the momentum deficit is predicted by the thrust-coefficient curve and local wind speed (cf. Section 2.1). The wakes move with the fluctuating large-scale wind field using a spatial filter to remove contributions from ambient eddies smaller than a characteristic wake dimension. The velocity deficit is gradually decreased by wake entrainment. With the adopted kinematic simulation approach it is straight forward to simulate correlated movements of *multiple turbine wakes*.

3 Experimental verification

The aim of the experimental part of the project is to verify the DWM model complex. Two full-scale experimental campaigns have been used for this purpose – the Tellus experiment, and the Tjæreborg experiment. The Tellus campaign is conducted within the frame of the present project, whereas for the Tjæreborg campaign data analyses were conducted based on existing available data.

The primary focus in the Tellus campaign is on the basic conjecture on which the DWM model is founded – i.e. that the wake meandering can be modeled considering the wake to act like a passive traced driven by large-scale turbulence structures. As for the data analyses of the other experimental campaign aspects of wake deficit modeling, wake turbulence modeling, and wind turbine load modeling are treated in addition.

The structure of the experimental part closely reflects the involvement of two different experimental campaigns. These are described in some detail in the succeeding sub-sections.

3.1 Tellus experiment

The full-scale Tellus experiment was designed and conducted with the primary aim of verifying the basic conjecture in the Dynamic Wake Meandering (DWM) model complex – i.e. that the lateral- and vertical wake deficit transport (i.e. meandering) basically act as if the wake (deficit) was a *passive tracer* driven by the large-scale turbulence eddies in the atmospheric boundary layer. However, also the study of the shape, widening and attenuation of the wake deficit are of interest.

In order to achieve the goal put forward above, it has been necessary to develop a measuring technique that allow for an *instantaneous recording* of the wake deficit at a specified downstream position. The key instrument in this respect is a LiDAR (Light Detecting and Ranging) system based on measurement of the Doppler shift between emitted- and reflected laser signals from aerosols assumed to move with the flow in question. However, the available commercial systems had some shortcomings in respect to the present application. First of all, the data *processing time* in the supplied software turned out to have an unacceptable performance. Secondly, the conventional conical scanning mode is designed for measurements of spatial averaged wind characteristics, whereas the requirement here is to record instantaneous *wind speeds in many points*. These shortcomings have required substantial refinements of the available LiDAR equipment.

The presentation is structured as follows: The required LiDAR related modifications are described in the in the first two sections. Subsequently follows a section describing the application of the modified LiDAR system with the Tellus turbine at the Risø test area, a section describing the applied data acquisition philosophy, and a section describing the resulting data set, respectively. Finally, analyses of selected results are presented in the last section.

3.1.1 Improvement of data analysis software

The available commercial data processing software could, at the start of this project, handle up to 15 measurements per second. This performance is insufficient for the present application of the LiDAR, where an acceptable 1-D and 2-D spatial resolution of the wake wind speed recordings requires of the order of 150 measurements pr. second (thus corresponding to *one* wake scan). The specified 1Hz recording frequency is required to

facilitate a fast enough scanning of the wake that the result can be considered an *instantaneous* wake observation.

In order to increase the data processing performance, the data processing software has been rewritten in C using the Fastest Fourier Transform in the West (FFTW - www.fftw.org). These initiatives have increased the processing speed significantly, with the result that the scanning rate has been raised to 136 measurements per second. Details on this implementation may be found in the Master Thesis of Ferhat Bingöl [64].

3.1.2 Adaptation of the LiDAR

In order to facilitate recording of the instantaneous wake position, development of new operational modes of the LiDAR have been necessary. Two different types of operational modes are defined accordingly – a 1-D mode, in which the wind speed is scanned in the direction of the laser beam along a circular arc defined by the specified focus distance of the LiDAR, and a 2-D mode, where the wind speed is scanned in the direction of the laser beam being swept over part of a sphere defined by the specified focus distance.

Figure 3-1 The QinetiQ ZephIR lidar head mounted on the downwind end of the Tellus nacelle. From [15].

In order to achieve the requested features two adjustments have been performed. As for the 1-D scanning mode, the optical wedge, providing the conventional laser beam deflection for conical scanning, has been dismantled, thus making the LiDAR a straight shooter measuring the wind speed in the direction to which it is pointed. Subsequently, the LiDAR has been placed on top of a tilt and pan head originally designed for security cameras. The head can move in the range $\pm 35^{\circ}$ in pan and $\pm 15^{\circ}$ in tilt. However, only the pan movement has been utilized with the present setup, whereas tilt is adjusted to align the laser beam with the surface only. The movement of the head is controlled by a PC, and data defining the

instantaneous pan position has been synchronized with the LiDAR velocity recordings by simply measuring the pan position exactly the same time the wind speed is recorded.

Contrary to the 1-D scanning mode, the 2-D scanning mode makes use of the optical wedge. However, the functionality of the wedge is modified compared to the layout in the commercial LiDAR, in order to obtain a vertical deflection component of the laser beam. This is achieved by designing a special wedge movement mechanism that rotates the wedge in 38° eight to ten times per second. With the wedge properly mounted this mechanism basically results in a vertical-like beam deflection which, together with the mechanically generated horizontal panning movement of the head, results in the requested 2-D scanning pattern.

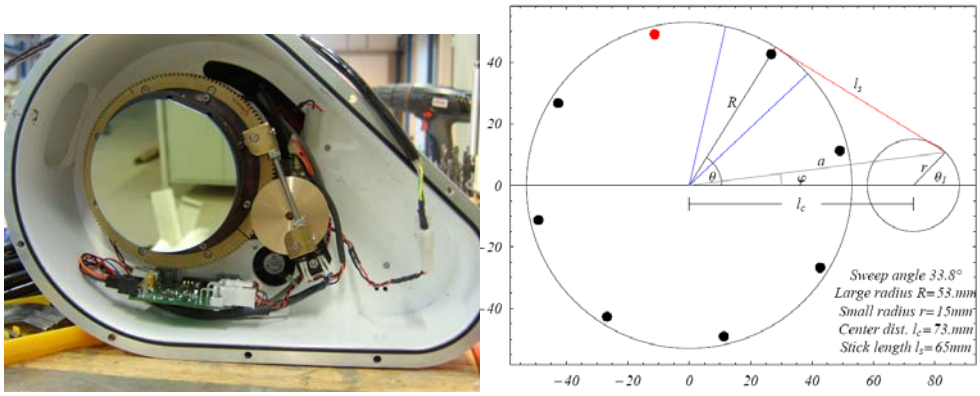

Figure 3-2 The wedge inside the lidar head with a small motor turning it rapidly forth and back. Geometrical description of the mechanism. From [15].

The combined mechanical and optical generated beam deflection will describe a path on a spherical segment defined by the specified LiDAR focus distance. With a pan movement of ±25° and a focus distance equal to 58 m the focus point pattern shown in Figure 3-3 results. Note that *individual* full 2-D patterns, associated with *different* full 38° wedge rotations, in general will result in different focus point paths. They will, however, always be within the same lateral and vertical boundaries.

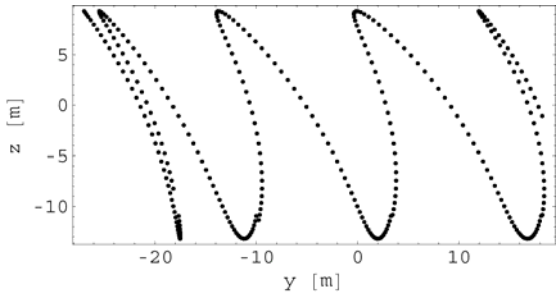

Figure 3-3 A sample of the 2-D Sphere Scan Mode pattern. Horizontal axis is the lateral deflection (in meters) associated with the pan position (±25°), and vertical axis is the vertical deflection (in meters) driven by the wedge rotation (± 19°). Each full 2-D pattern scan might end up with different scan point positions, but they will always be within the same boundaries. From [15].

3.1.3 Experimental setup

The test site is a relatively flat and homogeneous terrain located near Risø National Laboratory/DTU Roskilde, Denmark, and it is being used simultaneously also for other experiments. The site's average yearly wind direction is 289°. The experimental setup consists of the adapted LiDAR system mounted on a test turbine along with two meteorological masts dedicated to wind field reference measurements.

The test turbine is a Tellus 95kW. Hub height is 29.3 m and rotor diameter is 19 m. This size of turbine is ideally suited for wake experiments with the LiDAR system. This is because the LiDAR system has a distance limitation of the order of 200 m, thus roughly covering the wake downstream distances of interest (i.e. 0 - 10 rotor diameters).

The adapted LiDAR head, mounted on the tilt and pan head, was fixed on the nacelle of the Tellus turbine with the LiDAR looking downwind. The LiDAR is thus positioned in hub height corresponding to at 29 m a.g.l.. The data acquisition part of the LiDAR system was located in a shelter at the foot of the turbine and connected to a local area network, thus facilitating remote control of the recording system.

In the experimental campaigns three scanning modes of the LiDAR system have been applied – all based on the developed 1-D and 2-D scanning facilities. The defined scanning modes will in the succeeding be denoted as the line scan mode, the deep line scan mode and the sphere scan mode, respectively.

The *line scan mode* is the most simple of these modes. In this 1-D mode the LiDAR focuses to a single distance, and pans in the range ±30°, thus generating a circular arc scan behind the Tellus turbine. Each line scan takes 1.3 seconds, while the wind speed in this span of time is measured approximately 180 times on different positions along the arc. The line scan mode philosophy is illustrated in Figure 3-4.

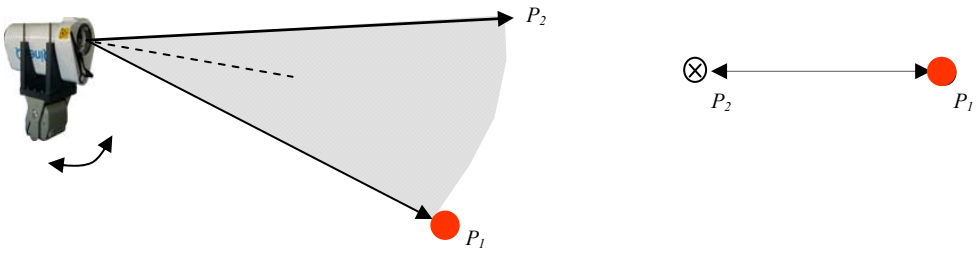

Figure 3-4 Line scan mode. Pan position changes from P1 to P2 continuously and wind speed measurements are made 136 times per second. One movement from P1 to P2 takes 1.3 seconds. From [15].

The *deep line scan mode* is a slightly more advanced version of the 1-D type of scanning. In this scan mode the focus distance is changed every other line scan, thus resulting in approximately instantaneous wind speed measurements for each specified downstream distance. The focus is changed so that the instrument roughly follows the same air parcel downstream, assuming downstream advection with the mean wind speed obtained from the reference mast MM2. When the focus limit of the LiDAR is reached (i.e. 200 m), focus distance is changed to 20 m to start the operation all over again. The deep line scan mode has been operated in a downstream range extending from 1 rotor diameter to 10 rotor

diameters with a “resolution” corresponding to 4-5 stations. The process time for a full cycle is between 18 and 24 seconds, including the time required for focus changes. The principles of the deep line scan mode are illustrated in Figure 3-5.

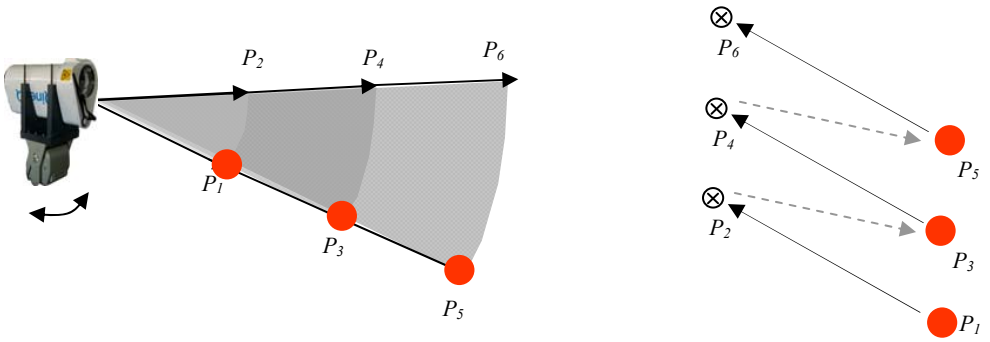

Figure 3-5 Deep line scan mode. After every 2 line scan, the data recording stops, and the LiDAR changes focus to a new distance and then continues to scan. The change-of-focus-operation takes approximately 1 second. From [15].

The *sphere scan mode* is based on the 2-D scanning technique. With the LiDAR focused to a specified downstream distance, the mechanical pan movement is specified in the range ±25°. The recording time for a complete cross sectional scan of the velocity field is determined by the time required for the pan head to cover the angle range ±25°, which is approximately 1 second. One cycle of the optical beam deflection, obtained by the wedge movement, takes approximately one quarter of a second, meaning that each cross section is being resolved with approximately 8 vertical-like “lines” (cf. Figure 3-3).

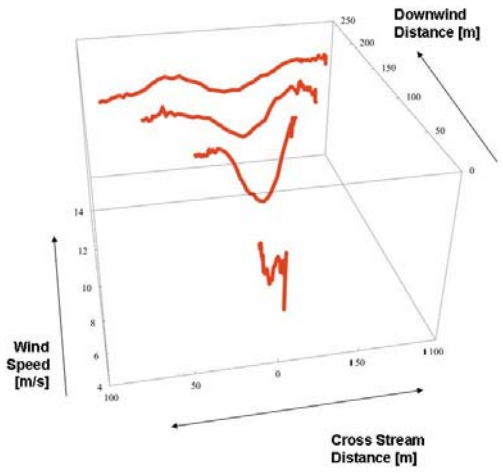

Figure 3-6 Illustration of the deep line scan mode capability. Data are collected from four different focus distances (19 m, 76 m, 130 m and 176 m). The initial wake is of the same size as the rotor and widens gradually downstream. In the closest focus distance all measurements are in the wake, but further downstream the wake as well as the undisturbed wind on the sides of the wake can be seen. From [15].

The primary reference mast (MM2) is situated 36 m from the test turbine in a westerly direction. This mast is 33 m high and equipped with wind speed and wind direction sensors in various heights to supply mean wind speed data as well as wind direction data that can be suitably averaged to filter away that fast fluctuating part of the wind direction signal associated with the small scale turbulence.

The secondary reference mast (MM1) is situated 114 m from the test turbine in a north-western direction. This reference mast is likewise equipped with wind speed- and wind direction sensors in various heights. In addition, it is equipped with temperature, pressure and rain sensors.

A second turbine is situated 70 m approximately north of the test turbine. The turbine is a Nordtank 500 kW turbine with a hub height of 36 m and a rotor diameter of 41 m. This turbine is not a part of the present experiment but excludes, however, wake investigations for mean wind directions from a certain wind sector. The positions of the turbines and meteorological masts at the site are shown in Figure 3-7. Also shown in this figure are various wind direction sectors with relevance for the present wake experiment. The light blue area denotes the selected wind direction sector for the present wake experiments. The selected wind direction sector is 30° wide extending from 274° to 304°. With this choice the MM2 mast is seen to be centered in the wind direction sector of interest. The red area sketched behind the Tellus and Nordtank turbines, respectively, are estimated wake influence regimes in the range up to 70 m downstream the turbine in question for wind direction 289°. Finally, the green sector symbolizes the swept area of a LiDAR 1-D scan measurement.

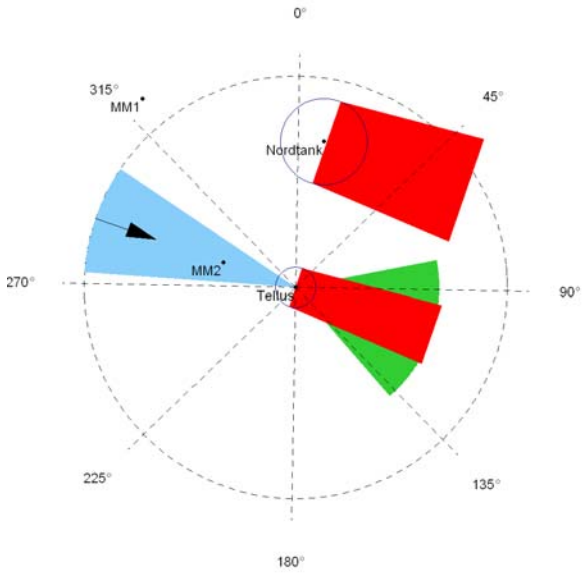

Figure 3-7 Positions of the two masts and two wind turbines and various sectors of relevance for the experiment. From [15].

3.1.4 Data acquisition

The LiDAR data is archived in 10 minutes data blocks as binary files. It includes each averaged Doppler spectrum and additional information according to the working mode. The recording is demanding in terms of storage requirements. One data block occupies nearly

80 MB, and one day of data is approximately 12 GB. The storage problem has been solved with external USB hard disks, and over a half terabyte of data has been collected in this study. Keeping the entire Doppler spectrum, instead of only the computed wind speed, enables us to re-process the data to improve the Doppler spectrum peak finding algorithm, which is essential for obtaining reliable results. The LiDAR wind speed data derived from the Doppler spectra are subsequently added to a MySQL database defined for the additional reference data (c.f. the description below).

The recorded data from turbines and meteorological masts are collected into one single synchronized MySQL database to facilitate data analysis. This combined database includes 17 channels of data originating from three different measuring campaigns in May 2005, November 2005 and February 2006, respectively. The signals are recorded using up to four synchronized measurement PC's. The details of the available sensor signals appear from Table 3-1.

Table 3-1 Available data channels in the database (WS: Wind Speed; WD: Wind Direction; WSN: Wind Speed Nacelle; WDN: Wind Direction Nacelle; YM: Yaw Misalignment).

Turbine/ Met. mast	**Channel**	**Height**
MM1	WS	35 m
	WD	36 m
	Temperature	3 m
	Pressure	3 m
	Rain	-
MM2	WS	29.3 m
	WD	19.7 m
	WD	29.3 m
	WD	35 m
Tellus	WSN	35 m
	WDN	35 m
	Power	-
	YM	-
Nordtank	WSN	29 m
	Power	-
	RPM	-
	Status	-

3.1.5 Data base bank

As it appears from Table 3-2, first phase the measurement campaign is started in the last quarter of 2004. At this time, the reference mast MM2 is not yet erected. The types of LiDAR data recorded are Line Scan data and Deep Line Scanning data, and these data files include only pan position and 256 size Doppler spectra.

Table 3-2 Measurement Calendar

Scanning Mode	Start	End
Line Scan and Deep Line Scan	2004-09-15	2005-05-01
Deep Line Scan	2005-10-14	2005-10-29
Line Scan	2005-10-29	2005-11-21
Sphere Line Scan	2006-04-26	2006-05-11
Sphere Line Scan	2006-06-06	2006-07-12

After erection of the reference mast MM2, the second measuring phase is initiated at the end of 2005. In addition to the reference sensors on MM2, a yaw sensor on the Tellus turbine, as well as various other data from available instruments on the Tellus turbine, are now available. As an introduction, the LiDAR measurements from the first phase are repeated. Subsequently a substantial amount of additional LiDAR recordings are monitored with the Line Scanning mode being the dominating scanning mode. All measurements refer to a time stamp, which enables recordings from the various involved measuring computers to be fully synchronized.

In the second quarter of 2006, the third measuring phase is initiated. The LiDAR is physically updated with a new wedge mechanism, enabling 2-D LiDAR scans to be performed. In addition, the 2-D setup required an update of the measurement PC to facilitate reading of the wedge and pan position at the same time instant. A simple multi thread coding structure has been used to record each Doppler spectrum, the associated wedge- and pan positions, and the requested time stamp for synchronization purposes.

3.1.6 Results

In this subsection an extract of the initial data analysis studies are presented. Based on previous studies [65], we have selected the data from non-rainy days with the wind direction range of $\pm 15^{\circ}$ from the MM2 direction of 289° (cf. Figure 3-7). In this sector wind blows directly from the reference mast MM2 to the Tellus turbine, and the LiDAR measurements are not corrupted by the presence of the Nordtank wind turbine, nor affected by its wake. Only the days where MM2, Tellus and LiDAR data are 100% available has been used. The presented initial analyses will focus on data resulting from the line scan mode and the sphere scan mode only.

As for the *line scan* measurements, blocks consisting of 10 minutes of data are analyzed. Each scanned arc of velocities are included in a plot side-by-side with a gray scale indicating the measured wind speed (cf. Figure 3-8), thus resulting in a depiction of the wake deficit displacement at the particular focus distance as a function of time. The light areas in the figure symbolize high wind speeds, whereas dark areas symbolize low wind speeds. The red lines in Figure 3-8 symbolize model predictions of the wake deficit positions (meandering) based on the spatially averaged (instantaneous) direction evaluated from the three wind vanes on the reference MM2 mast, corrected for the measured yaw position of the Tellus nacelle as well as for the advection time (i.e. the time required for an air parcel to move from MM2 to the downstream focus distance).

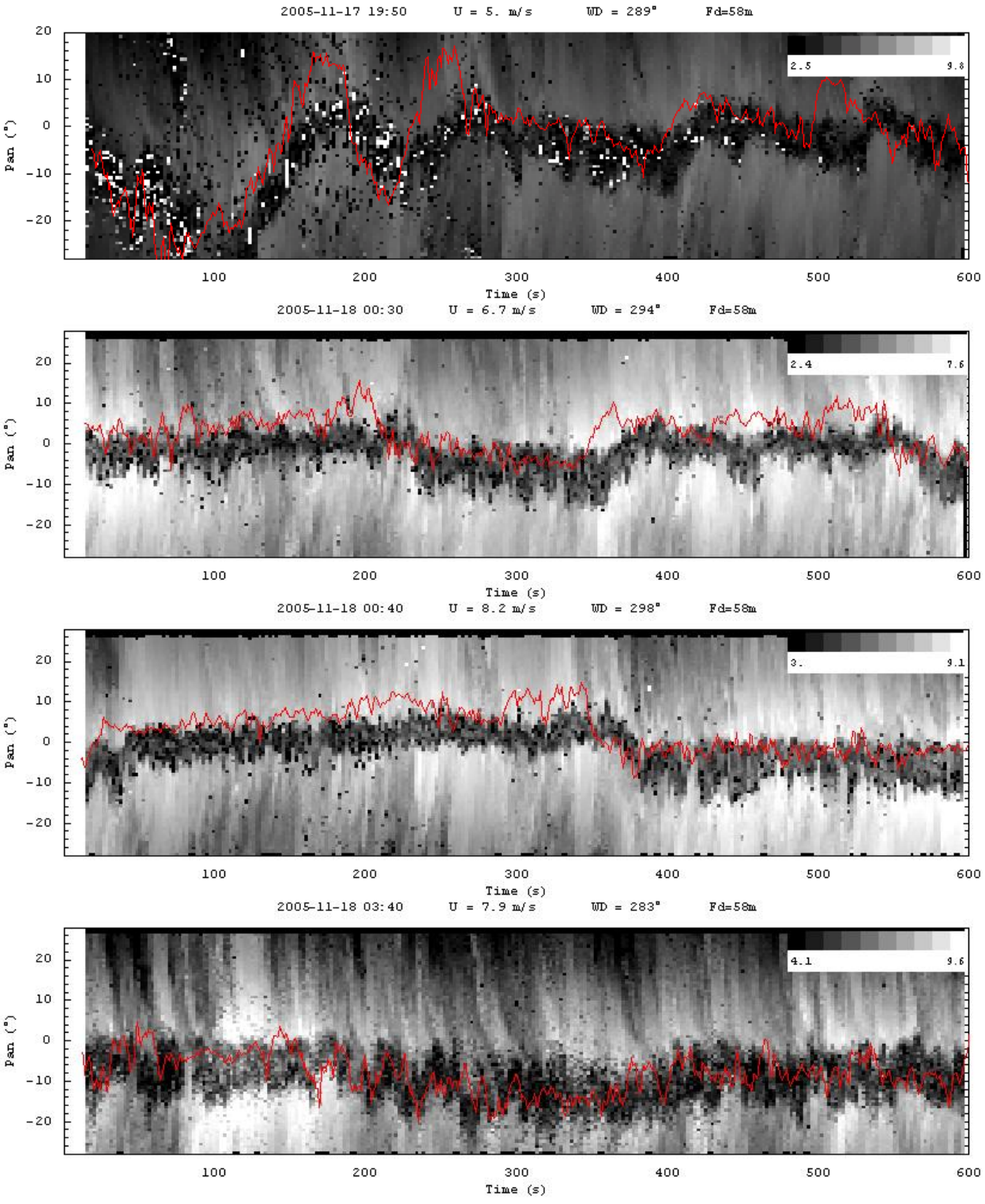

Figure 3-8 Line Scan data plotted in gray scale as function of time. Low wind speed is shown as black and higher wind speed is shown as white. Focus distance is 3 diameters (58 m). From [15].

With the selected representation of data and model, it is easy to identify the measured wake width and wake movements as well as the correlation between the predicted instantaneous

wake position and measured instantaneous wake position. The model of the wake dynamics assumes the wake deficit to be advected in the *mean wind direction* with the mean wind speed and advected in the *lateral direction* with the large scale lateral turbulence component [1]. Assuming Taylor's hypothesis, the "driving" lateral velocities are perfectly correlated with the filtered wind direction measurements at the reference meteorological mast, however, delayed with the transportation time from the mast to the downstream point of interest. Thus for the present case, where the meteorological mast is 36 m upstream the turbine, the requested delay is the time for an air particle to move 36 m plus the focus distance with the mean wind speed. In general, the predicted wake movements show a convincing correlation with the measured wake movements, thus supporting the wake meandering hypothesis stated in the introduction.

In Medici [36] laboratory experiments was conducted indicating that 3-D low frequency vortex shedding might control the wake meandering process. However, the experimental conditions for the reported wind tunnel experiments differ significantly from the experimental conditions for the present full-scale experiments, especially concerning the rotor thrust coefficient. Whereas vortex shedding might control the wake meandering mechanism for high loaded rotors under experimental conditions in a wind tunnel (cf. Section 2.3.1), we believe that *the wake meandering is controlled by the large scale turbulence eddie*s for realistic loaded full-scale rotors operating in the atmospheric boundary layer.

One of the problems in understanding the data in Figure 3-8 is that the wake width is often smaller than anticipated. The Tellus turbine has rotor diameter of 19 m, and focus points are 3 diameters downstream. According to the currently available wake models, the width should be larger. From Figure 3-8 the wake width 3 rotor diameters downstream can be estimated to approximately 12° to 18° in pan, corresponding to a wake diameter of the order 12 m to 18 m, which is even smaller than the rotor diameter. Currently we do not fully understand this discrepancy, which also contradicts the measurements from the first phase of the measuring campaign (c.f. Figure 3-6). However, most likely we cut the wake horizontally not in the middle but closer to the top or the bottom.

The problem with interpretation of the observed wake widths from the line scan measurements can be studied more in detail if based on *sphere scan* recordings, which resolves both the lateral- and the vertical wake position at a prescribed downstream distance.

A provisional example of a 2-D scan of the instantaneous wake deficit is shown in Figure 3-9. In this experiment, corresponding to a focus distance of 58 m, a wake width of approximately 28 m has been observed, which is of the expected order. This result supports our hypothesis of possibly cutting the wake in the upper or lower part in the *line scan* mode. Presuming this being the case, the reasonable explanation would be that the LiDAR is not perfectly horizontally aligned with the surface for the *line scan* recordings but is rather aligned with a small degree in tilt.

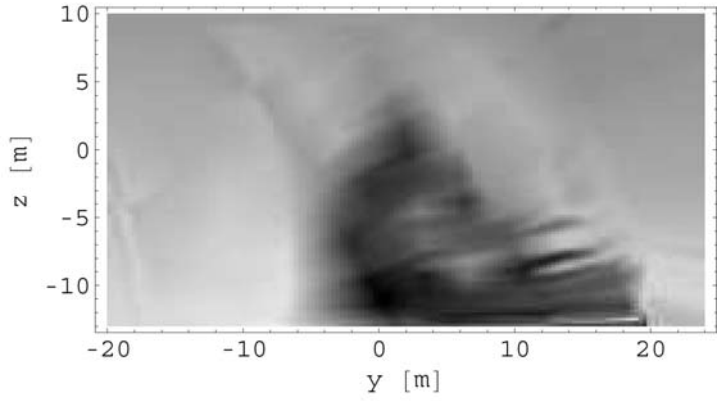

Figure 3-9 Sphere Scan of a downstream wake. Darker areas are lower wind speed, and the LiDAR continuously scans the wake and the velocity regime outside the wake. This plot is based on approximately 1 second of measurements. The focus distance is 58 m. From [15].

3.2 Tjæreborg experiment

The model of the wake meandering process has been verified *directly*, by comparison of measured- and simulated wake wind field characteristics [2], as well as *indirectly*, by comparing load characteristics experienced by a turbine exposed to wake load conditions [3]. The main emphasis will presently be on the first mentioned category of comparisons, and these encompass analyses of *statistical parameters* as well as analyses of *instantaneous observations* (i.e. instantaneous position of the wake in the atmospheric boundary layer).

3.2.1 Experimental setup

The Tjæreborg wind farm is situated on a flat terrain approximately one kilometer from the North Sea coast line (being in a westerly direction). The site is characterized by almost offshore roughness conditions in a westerly sector, and class 1 conditions in the remaining sectors, with the terrain slope being less than 2 deg. in all directions within several kilometers. The layout of the farm is illustrated in Figure 3-10, where the positions of the meteorological mast and the wind turbines are specified in northern- and eastern co-ordinates, respectively.

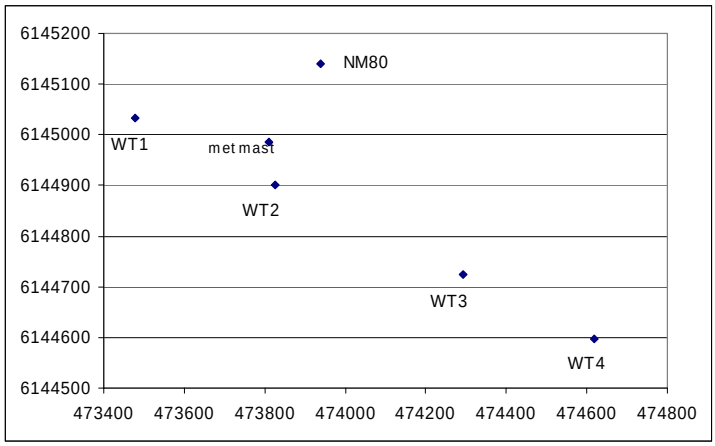

Figure 3-10 Layout of the Tjæreborg wind farm, including the meteorological mast. From [2].

The analyses to follow focus on *single wake situations* caused by the NM80 wind turbine, which is positioned 2.5 rotor diameters from the meteorological mast in direction 40 deg..

The available meteorological mast is instrumented with a variety of sensors in different levels [66]. In addition to the meteorological mast, one of the blades on the NM80 turbine was equipped with a five-hole pitot tube, thus enabling instantaneous measurements of the local angle of attack and the relative velocity on the rotor of this turbine. The NM80 rotor has a diameter of 80 m, and a the pitot tube is mounted on the blade at a radius of 26.2 m and in an angle of 31 deg. relative to the tip chord (cf. Figure 3-11). Further details of the experimental setup can be found in [67]. The pitot tube measurements have been recorded with a sampling frequency equal to 25 Hz, and prior to recording the signals have been passed through a low pass filter with cut-off frequency equal to 25 Hz in order to avoid aliasing.

Figure 3-11 The five hole pitot tube mounted on the leading edge of the blade. (The plate mounted on the blade is used for measurement of the angle of the pitot tube relative to the tip pitch).

Unfortunately, the instruments on the meteorological mast and the pitot tube was not in operation simultaneously, and as a consequence the data from the meteorological mast and the pitot tube data are to be considered as individual measuring campaigns associated with the same experiment.

3.2.2 Horizontal mean wake deficit profile

For the present investigation the wind speed sensor at level 57 m on the meteorological mast (equivalent to the wind turbine hub height) and the wind direction sensor at level 54.7 m have been used.

Basically, a narrow wind direction sector (± 20 deg.) around wind direction 40 deg., corresponding to the directions from the meteorological mast to NM80, has been selected for the analysis. Assuming identical upstream conditions within this sector (i.e. identical ambient turbulence intensity) and further neglecting the small change in downstream distances associated with measured- and simulated results, respectively, the expansion of the *mean wake deficit* in a statistical sense – interpreted as a mean of a meandering deficit along a horizontal line perpendicular to the mean wind direction – can be estimated directly from the mean wind speed statistics recorded at the meteorological mast, provided that the associated undisturbed ambient mean wind speed is available.

The present concept of wake meandering implies that wind conditions, at a given downwind position, are undisturbed for part of the time and interrupted by episodes of intense turbulence and reduced mean velocity as the wake hits the observation point. Thus, the mean wind speed at a given position, associated with a given mean wind direction, will appear as a weighted average of the undisturbed situation and the various wake situations occurring during the considered time span as a result of the wake meandering. Therefore, with the given assumption on the upstream conditions, the observed *mean* wind speed as a function of the wind speed direction (obtained from the meteorological mast) is equivalent to the simulated sum of the *mean* wake deficit and the undisturbed ambient mean wind speed.

Based on the above considerations, a comparison between horizontal measured- and simulated *mean* wake (wind speed) profiles is performed and displayed in Figure 3-12 for an ambient mean wind speed equal to 10 m/s. Note, however, that for the measured data, ambient mean wind speeds in the range [9 m/s; 11 m/s] have been considered, reflecting the usual balance between the amount of available data and the selected bin size.

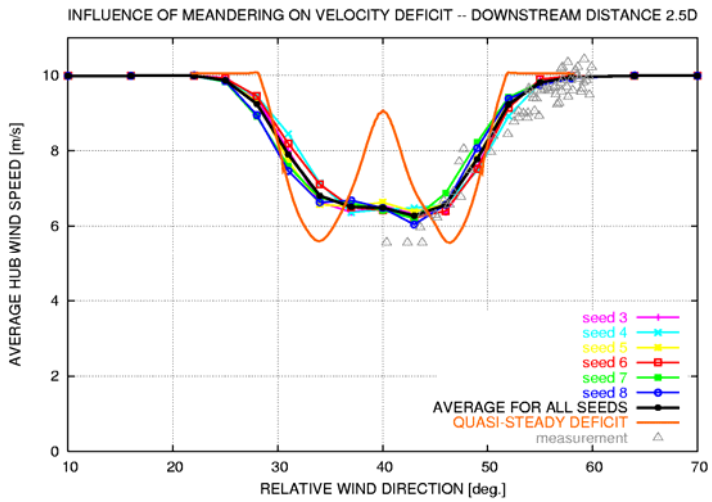

Figure 3-12 Computed and measured 2.5D downstream mean wake profiles corresponding to an ambient mean wind speed equal to 10 m/s and to an ambient turbulence intensity equal to 9%. From [2].

In Figure 3-12 the red curve is the quasi-steady wake deficit, which in a sense is to be considered as input to the wake meandering process. The remaining curves (equipped with labels) are the simulations based on various realizations of the stochastic transportation process, whereas the triangles symbolize the measurements. The characteristic double bell shape of the quasi-steady wake deficit results from the thrust distribution over the wind turbine rotor, and the larger extension of the *mean* wake profiles naturally reflects the wake meandering. As seen the characteristic quasi-steady double-bell shape is transformed into a Gaussian like shape by the meandering process, and the simulated results are seen to agree reasonable with the measured data, both in terms of extension of the *mean* wake profile and in terms of *mean* wake deficit amplitudes. The observed measurement scatter in Figure 3-12 is considered mainly to be due the applied binning. Assuming the proportion between wake deficit magnitude and ambient wind speed to be mean wind speed invariant implies an effect of the prescribed binning of ± 10% on the observed wake deficit values, which roughly corresponds to the observed magnitude of the scatter.

3.2.3 Horizontal turbulence intensity profile

The *measured* horizontal profile of the (horizontal) wind speed turbulence intensity has also been established based on the Tjæreborg data. To improve accuracy, the reference mean wind speed for the turbulence intensity computation is taken as the measured undisturbed ambient mean wind speed, rather than the average of the mean wind speed bin considered. The applied analysis method is analogues with the method described for the analysis of the mean wind speed profile in the previous section, and the presumptions are consequently identical. The resulting turbulence intensity profiles include contributions from the undisturbed atmospheric turbulence field superimposed by contributions originating from meandering of the wake mean wind speed deficit as well as from meandering of the turbulence shed from the upstream turbine in the form of trailed vorticity consisting mainly of tip and root vortices.

As for the *simulated* wake characteristics, the wake shear generated turbulence is accounted for in the simulation of the quasi-steady wake deficit expansion as function of transportation time. Further the influence of the ambient turbulence field on the wake meandering process, and thereby on the turbulence contribution caused by wake meandering, is included. On the other hand the turbulence caused by the vortices shed by the upstream turbine has not been taken into account in the model. This subject was considered in a recent paper [8], and it was found that for the *lateral turbulence* components the meandering process of the wake deficit does not create any notable turbulence, whereas a considerable additional longitudinal turbulence contribution from the wake could be seen in the experimental data. This observation is also in agreement with the analysis of the wake turbulence characteristics to follow.

Figure 3-13 shows the resulting comparison of simulated and measured horizontal wake turbulence intensity profiles associated with the downstream distance 2.5D.

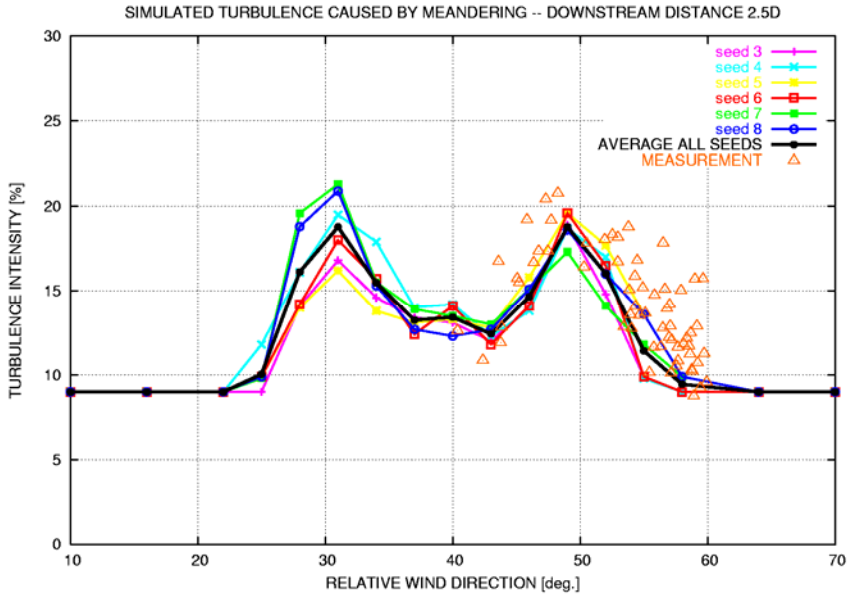

Figure 3-13 Computed and measured 2.5D downstream mean wake turbulence intensity profiles corresponding to an ambient mean wind speed equal to 10 m/s and to an ambient turbulence intensity equal to 9%. From [2].

The triangles symbolize measurements, whereas the curves are simulations associated with five different realizations of the stochastic transportation process. A comparison of simulated- and measured wake turbulence intensity profiles shows reasonably agreement in terms of both *shape*, *expansion* and *magnitude*, which is a quantitative indication of the validity of the proposed wake meandering model. However, as expected, there is a tendency of higher measured turbulence intensity levels, because the modification of the turbulence field in the wake region – as described in the moving frame of reference – has been neglected in the simulations. Contrary to the situation for the measurement scatter on the wake deficit profiles in Section 3.2.2, binning of the measured signals in Figure 3-13 will *not* influence the scatter on the measured turbulence intensities, as these are normalized with respect to the actually observed mean wind speed. The observed measurement scatter is therefore most likely associated with varying atmospheric stability conditions. Note finally the qualitative agreement of the results shown in Figure 3-13 with the CFD based results shown in Figure 2-33.

3.2.4 Wake deficit meandering

The pitot tube measurements can also be used to extract information *directly* on the vertical and transversal wake meandering displacement as function of time in an approximate manner. The basic idea is based on the recognition that the *extend* of the wake can be roughly estimated from the standard deviation of the azimuthally binned local inflow angle as measured by the rotation pitot tube. Contrary to the azimuthally binned angle of attack itself, the standard deviation turn out to be relatively insensitive to azimuthally changes in mean flow conditions caused by tower flow effects and the (mean) wind speed shear caused by the presence of the ground, thus isolating the flow effects caused by the presence of the wake. The details of the method can be found in [2].

The measured wake deflections have subsequently been compared with simulations emulating, as close as possible, the experimental conditions. As both estimated- and simulated displacements are to be considered as arbitrary realizations of stochastic processes, no one-to-one correspondence is a priory expected between these. However, their statistics can be compared.

The analysis has revealed that both the lateral- and the vertical displacement ranges were very similar for the estimated and the simulated displacements, respectively. The deviation between estimated- and simulated results, in terms of standard deviation of the respective displacements, is of the order of 10%. This is considered acceptable considering the required approximate estimation of the ambient turbulence conditions caused by lack of direct ambient wind field measurements. Details can be found in [2].

However, the uncertainty, associated with the approximate estimation of the ambient turbulence conditions, can to some degree (discharging possible differences in the turbulence length scales) be eliminated by considering the proportion between the lateral- and the vertical wake displacement standard deviations. For the estimated quantities, this proportion is 1.50, whereas it is 1.52 for the simulated quantities and thus almost identical. This is again a strong indicia/evidence for the validity of the basic assumptions in the proposed model – i.e. that the wake meandering is driven by the large-scale turbulence structures.

3.2.5 Wake turbulence characteristics

The wake turbulence is in the present context understood as the turbulence in the wake regime expressed in the *meandering frame of reference* – or put differently – the modified turbulence in the wake regime associated with the quasi-steady wake deficit profile. This turbulence is spatially inhomogeneous as its characteristics at the limit of the wake region obviously differ from its characteristics in the central part of the wake regime (cf. Figure 3-13). It is furthermore in-stationary, as it evolves with (wake transportation) time because the wake regime limits expand with time due to turbulent mixing that in turn causes successive modifications of the wake turbulence.

The wake turbulence may, as conventional turbulence, be characterized by its turbulence length scale, its turbulence intensity, and its coherence properties. In the present context, we have analyzed the *turbulence intensity* and the *turbulence length scale*. These quantities have not been directly observed in the Tjæreborg experiment. However, analysis of the rotor inflow angle of attack, provided by the pitot tube recording, may enlighten qualitatively the features of the turbulent energy distribution over the wake regime as well as on the size distribution of turbulence eddies. The term qualitatively will, in the present context, mean

relative to the energy of the ambient turbulence, provided that the effect of the aerodynamic induction is invariant with respect to the turbulence intensity level.

The method applied to extract the wake turbulence information is to exploit the close relationship between the inflow angle of attack and the inflow conditions perpendicular to the rotor plane for a rotor rotating with constant speed. Thus, assuming the turbulence intensity to be approximately proportional to the standard deviation of the measured angle of attack, we have investigated half wake operational conditions under very low ambient turbulence intensity conditions. The very low ambient turbulence intensity level, together with the modest downstream distance (2.5D), ensures a modest effect of wake meandering for the investigated wake situation[3].

The result is a profile proportional to the turbulence intensity along a circular arc cutting through the approximately stationary wake deficit at the investigated 2.5D downstream position. An example of such a profile is shown in Figure 3-14.

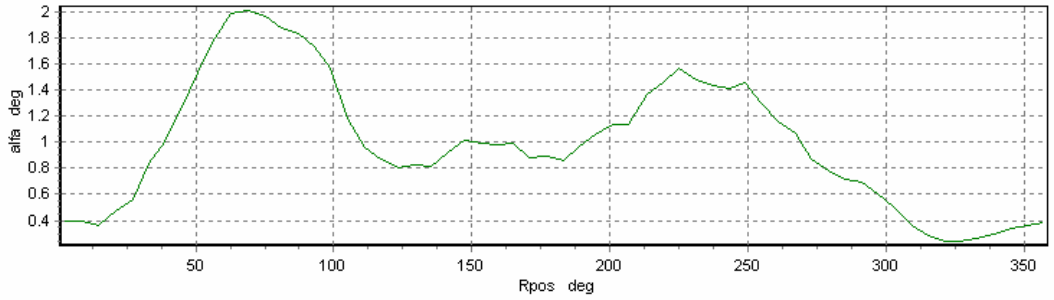

Figure 3-14 Binned standard deviation of the angle of attack associated with a low ambient turbulence situation. From [2].

The figure illustrates the turbulence intensity conditions associated with a wake regime extending from rotor positions in the range [25deg.; 320deg]. It is characteristic that the turbulence intensity at the edge of the wake regime is increased significantly compared to the ambient turbulence intensity, whereas the turbulence intensity, associated with the central part of the wake regime, is somewhat less amplified than the wake edge turbulence.

Although the effect of wake meandering on the wake turbulence is considered modest, it does contribute to the turbulence profile shown in Figure 3-14. This effect is studied in more detail in the following, where an approximate attempt to distinguish between the contribution to the total wake turbulence from the so-called *apparent turbulence*, caused by the meandering, and the *added wake turbulence*, generated directly by the up-stream turbine in the form of shed and trailed vorticity, is described. In this terminology, the added turbulence is equivalent with the wake turbulence described in the meandering frame of reference, but excluding the turbulence contribution constituted by the ambient turbulence.

In analogy with the initial investigation, we adopt the fundamental assumption in the DWM model (i.e. that the wake meandering is due to the large scale lateral- and vertical turbulence components), with the consequence that measurements recorded at very low ambient turbulence intensity conditions will be the data with the least possible influence from the wake meandering on the total wake turbulence when observed in a frame fixed to the ground. Such data, characterized by low ambient turbulence intensity conditions (i.e.

3 The effect of wake meandering is primary determined by the turbulence intensity of the ambient turbulence together with the transportation time (i.e. the downstream distance) of a wake cascade element (cf. the description of the meandering model).

turbulence intensity of about 3%), were identified in the measurement database and subsequently used for a study of the added wake turbulence characteristics in [8].

Three 10 minutes series were selected and used for the analysis; one with free inflow, one with about 1/3 wake operation (i.e. approximately 1/3 of the investigated rotor was affected by the wake from the upstream turbine) and one with approximately 2/3-wake operation (i.e. approximately 2/3 of the investigated rotor was embedded in the wake from the upstream turbine). It should be noted that these 3 series were measured within a time span of about 1½ hour, where the wind direction slowly changed and thus caused a variation in the type of wake operation.

Apart from the low ambient turbulence condition, the selected data are characterized by providing inflow information (in terms of pitot tube measurements) as well as structural response information (in terms of blade root bending moments). Both types of information are exploited in the analysis. As for the inflow recordings, the focus is on the *local inflow angle* and the *local relative velocity* at the position of the pitot tube. The strategy for this qualitative study is to model the selected measured time series, using the DWM model complex, and subsequently to compare measurements with model predictions. To provide a *reference* for the total wake turbulence, *excluding* the contribution attributed to the added wake turbulence, DWM simulations are conducted with only the ambient turbulence and the (modest) wake meandering contributing to the predicted turbulence in the wake regime.

In order to resolve the effects on the local inflow characteristics, arising from the spatial inhomogeneous turbulence, the measured- and simulated inflow characteristics have been binned with respect to the azimuthal sensor position. For each bin, the mean and the standard deviation are subsequently determined. The comparisons between measurements and simulations are presented in sets of figures where, for each figure, the measurement is shown in the left hand figure, whereas the right hand figure presents the associated DWM prediction.

Figure 3-15 shows the results for the *local inflow angle* associated with each of the three types of investigated wake situations, and Figure 3-16 shows the analog results for the *local relative velocity*. Comparing the free inflow situation with the two types of wake inflow, the effect of the total wake turbulence on the local inflow angle is clearly visible in the measured standard deviation of the local inflow angle and in particular in the analog measured standard deviations of the local relative velocity. As for the model predictions, it is seen that the standard deviation of the computed inflow angle is less than the measured, as expected. This difference is an approximate/indirect measure of the added wake turbulence in the meandering frame of reference. The standard deviation of the simulated relative velocity is almost zero. This is a consequence of the meandering mainly influencing the standard deviation of the inflow angle, and that no added wake turbulence has been included in the simulations.

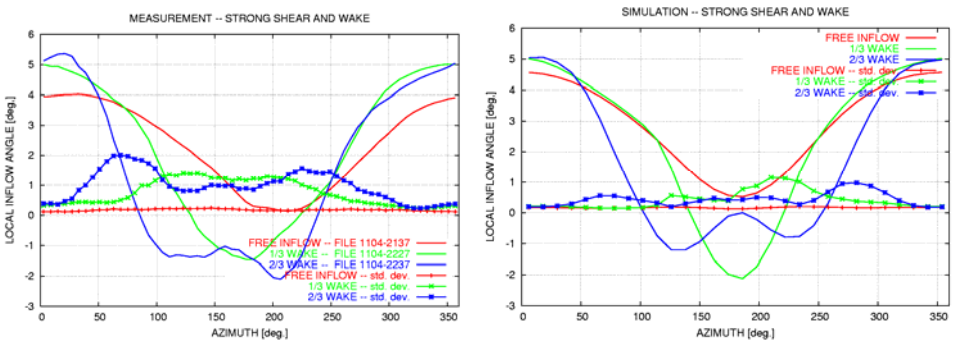

Figure 3-15 Measured and simulated local inflow angle binned on sensor azimuth positions. From [32].

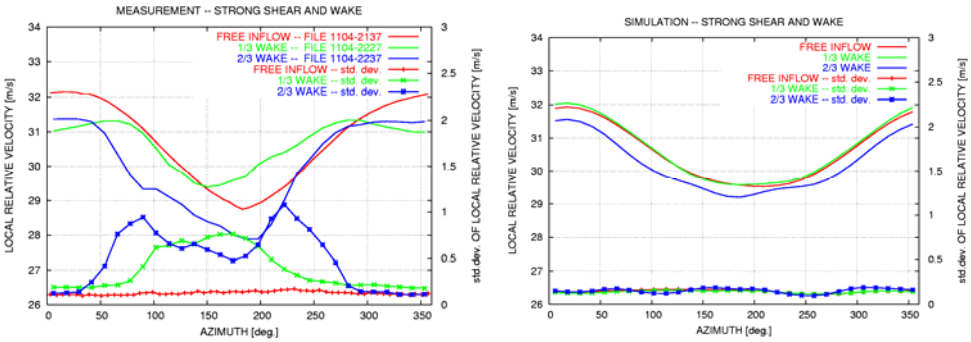

Figure 3-16 Measured and simulated local relative velocity binned on sensor azimuth positions. From [32].

A first crude attempt to quantify the added wake turbulence was performed by including artificial added wake turbulence in DWM predictions [8]. Although violating the true second order statistics of the wake turbulence, the added turbulence was prescribed simply by increasing the (ambient) turbulence in the wake region with a factor corresponding to an increase in wake turbulence intensity from 3% to 9% and 15%, respectively. The consequences, quantified in terms standard deviation of the local inflow angle and the local relative velocity, respectively, are shown in Figure 3-17 for the 2/3 type of wake situation. Shown on the same figure are the analyzed measurements corresponding to the wake situation in question as well as the similar results corresponding to the free flow condition.

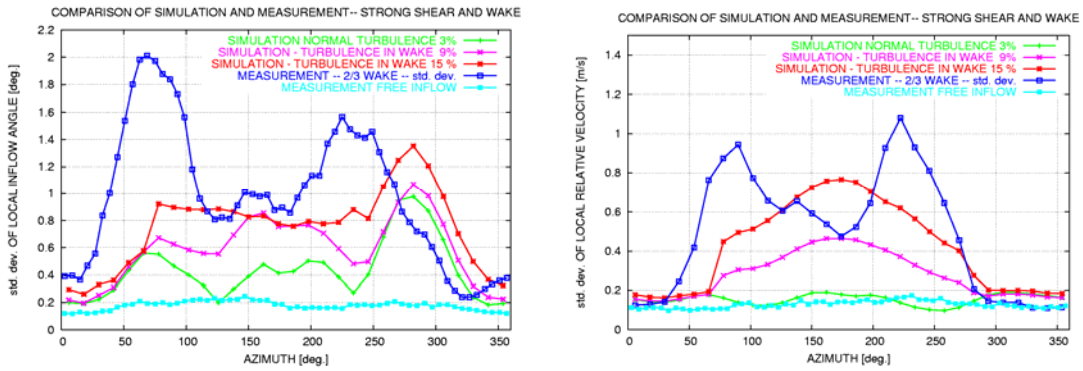

Figure 3-17 The effect of adding wake turbulence in the DWM model. The added turbulence has the same length scale as the ambient turbulence. From [8].

It is seen that by increasing the wake turbulence intensity to 15%, the standard deviation of the relative velocity approach the level of the experimental values, although it is quite clear, that the wake turbulence should *not* be increased with a constant factor over the whole wake width but on the contrary be strongest at the outer parts of the wake to approach the true inhomogeneous nature of the added turbulence. Nevertheless the investigation indicates the order of the magnitude of the requested added turbulence to reflect the measured magnitudes of the inflow standard deviations.

In addition to the spatial distribution of the turbulent energy over the wake regime, the distribution of the turbulent energy on the various turbulence eddy sizes (or equally distributed on frequencies) is of interest, as noted previously. The turbulence *length scale* is a simple scalar measure of this frequency distribution, when a specific generic spectral shape is assumed. In analogy with the turbulence intensity characterization, the analysis of the length scale, associated with the added wake turbulence, will also be pursued in a qualitative manner. For this purpose, we analyze the fatigue blade root bending loading expressed in terms of rainflow countings of measurements and DWM simulations, respectively. The selected wake situation is again the 2/3 scenario, and the free inflow condition is also included for reference purposes. The results are shown in Figure 3-18.

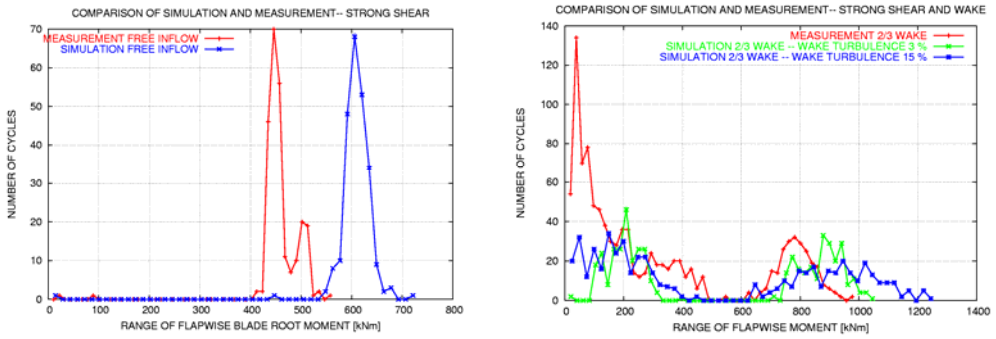

Figure 3-18 Rainflow counting on the flapwise moment. To the left the free inflow situation is shown, and to the right is shown the 2/3 wake case and the influence of increasing the wake turbulence.

The left hand side of Figure 3-18 corresponds to free inflow conditions and reflects mainly the cyclic loading caused by the vertical mean wind shear and the tower shadow. It appears that the specified vertical mean wind shear is somewhat overestimated, and, more importantly, that virtually no fatigue cycles is present in the low cycle range [0 kNm; 300 kNm].

The right hand side of Figure 3-18 corresponds to the investigated wake situation. It includes the measured results along with results from two predictions – one completely excluding the effect of added wake turbulence, and the second including added wake turbulence in the crude manner described previously (with the wake turbulence intensity equal to 15%). By comparing the measured results with the DWM predictions completely excluding the effects of added wake turbulence, we draw the conclusion that the added wake turbulence primary affects the low cycle range. The low cycle range primary relates to small turbulent eddies, which in turn is characterized by a small turbulence length scale and relatively high frequencies. The predictions, including the effect of added wake turbulence in the described crude manner, assumes that the added wake turbulence has a length scale similar to the ambient turbulence. Therefore, considerable difference between measurements

and these predictions should be expected, and this exactly what is seen when comparing the measured results with the predictions including the approximate inclusion of the wake added turbulence. Contrary to the measurements, the included added wake turbulence increases the number of big cycles and hardly affects the number of small cycles. The comparison thus indirectly shows, that the added wake turbulence should have a length scale *considerable less* than the one corresponding to the ambient turbulence.

The above conclusion is confirmed by comparing the power spectra of the local inflow angle and the relative velocity, respectively, as shown in Figure 3-19.

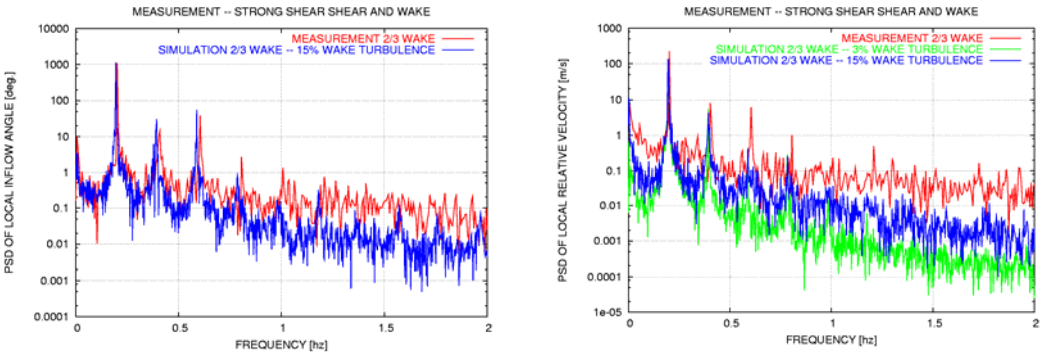

Figure 3-19 Comparison of simulated and measured power spectra of local inflow angle and local relative velocity, respectively. The latter comparison includes the effect of increasing the wake turbulence to 15%.

As it appears, there is pronounced lack energy content on the high frequencies for the simulations when compared to the measurements – again reflecting the lack of turbulence input on the small scales from the added wake turbulence. This observation is qualitatively in agreement with outcome of the CFD based investigation of the length scale of the wake generated turbulence conducted in Section 2.3.2.

3.2.6 Wake load characteristics

The DWM model complex has been used to predict turbine load during wake operations in [3], and the predictions have subsequently been compared to measurements. The investigated loads encompass blade flap loads as well as yaw loads, and both mean- and extreme loads under operation have been considered.

The analysis demonstrated good qualitative agreement between simulation and measurements for the flap- and yaw loads, respectively. This is again a strong evidence for the validity and universality of the model philosophy, as these loads exhibits significant differences in their character – yaw loads being an integrated rotor load and flap loading being a blade load.

4 Summary of conclusions

We have developed a consistent, physically based theory for the dynamic wake meandering phenomenon. The model is at present confined to wake situations, where the wake in question does not interact with other wakes. The model philosophy does, however, have the potential to include also mutual wake interaction phenomenons, and presently a simple heuristic description of wake interaction with a reflecting surface is formulated.

The basic conjecture behind the dynamic wake meandering model is that wake transportation in the atmospheric boundary layer is driven by the large scale lateral- and vertical turbulence components. Based on this conjecture a stochastic model of the downstream *wake meandering* is formulated. In addition to this kinematic formulation of the dynamics of the "meandering frame of reference", models characterizing the *mean wake deficit* as well as the *added wake turbulence*, described in the meandering frame of reference, are required to complete the wake meandering formulation.

As for the stochastic modeling of the wake meandering, we consider a *cascade* of wake deficit releases to be "emitted" in agreement with the assumed passive tracer analogy. We then subsequently describe the propagation of each instantaneously "emitted" wake deficit. Adopting Taylor's hypothesis, the downstream advection of these is prescribed/controlled by the mean wind speed. As for the dynamics in the lateral- and vertical directions, each considered wake cascade-element is displaced according to the large scale lateral- and vertical turbulence velocities in the rotor plane at the time instant where the considered element is emitted.

For design application of the dynamic wake meandering methodology, computational efficiency of quasi-steady wake deficit prediction is a key issue. The quasi-steady wake deficit is the wake deficit formulated in the meandering frame of reference, including effects of the wake expansion as function of downstream transportation time caused partly by turbulence diffusion and partly by the rotor pressure field. For this purpose two computationally low cost models are developed – one based on the boundary layer equations, and the other based on a vorticity formulation. The models have been verified by comparisons with actuator disc- and actuator line CFD models, respectively, and good agreement has been demonstrated.

The character of the added wake turbulence, generated directly by the up-stream turbine in the form of shed and trailed vorticity, has been approached by analytical as well as by numerical studies. As for the analytical approach, the classical vortex model of Joukowski has been extended by specifying an inner vortex structure enabling us to calculate induced velocities in very good agreement with measurements. The model may further explain the very high peaks appearing in the time signal of the axial velocity measured near the centre of the tip vortices of unsteady far wakes. Based on this wake model, a *linear* stability analysis of the tip vortex instability is performed. Contrary to similar analysis based on the Joukowski model, that predicts unconditionally unstable performance of the tip vortices, the extended analysis shows that the inner vortex sheet is able *stabilize the tip vortices* for certain choices of the parameters that describes strength and size of the vortex sheet. As for the numerical approach, we have simulated the turbulent flow field, generated in the wake region behind turbines, by combining large eddy simulations with the actuator line technique. The results are employed to derive Reynolds stresses, turbulence intensities as

well as turbulence power spectra of the added wake turbulence. The outcome of the analyses can be used to develop low-dimensional turbulence models for wind turbine design computations. For this purpose, we have exploited the POD technique to reconstruct and model the turbulent flow field, as well as a spectral approach that is able to generate second-order-consistent spatially inhomogeneous and in-stationary turbulence fields.

The concept of dynamic wake meandering has be verified by comparisons with extensive full-scale experiments. Basically these comparisons refer to two measurement campaigns – the Tellus and the Tjæreborg campaigns. Whereas the Tjæreborg data were made available from previous investigations, the Tellus experiment is designed and conducted within the framework of the present project. The experimental verification have encompassed the downstream wake meandering, the wake deficit and the wake turbulence characteristics.

The main purpose of the Tellus experiment is to verify the basic assumption of the dynamic wake meandering model – i.e. that the wake is advected passively by the large scale turbulence eddies in the inflow. This is accomplished by developing a measuring technique that, based on a LiDAR sensor, allows for high frequency resolution of the *instantaneous* downstream wake position. The measurements have been compared with model predictions of the instantaneous downstream wake deficit position at a given downstream distance. In order to capture the actual realization of the large scale turbulence components, the predictions were based on simultaneously recorded turbulence characteristics from a wind field reference mast positioned immediately in front of the wake generating turbine. The comparisons display a very convincing correlation between measurements and prediction, and are as such a strong evidence of the validity of the basic conjecture behind the dynamic wake meandering modeling.

The Tjæreborg data has been used to verify various consequences following from the dynamic wake modeling presumption. These encompasses horizontal mean velocity profiles, horizontal turbulence intensity profiles including the effect of wake meandering, and approximate qualitative analyses of the characteristics of the added wake turbulence. As for the horizontal mean velocity profile, it is demonstrated that the characteristic quasi-steady double-bell shape (caused by the rotor thrust distribution) is transformed into a Gaussian like shape by the meandering process, and the simulated results is seen to agree with the measured data, both in terms of extension of the mean wake profile and in terms of mean wake deficit amplitudes. Similar results are achieved by comparisons of simulated- and measured wake turbulence intensity profiles. Good agreement in terms of both shape and expansion is demonstrated, however, with an expected tendency of higher measured turbulence intensity levels. This is because the modification of the turbulence field in the wake region – as described in the moving frame of reference – has been neglected in the simulations. The approximate qualitative characterization of the added wake turbulence field has revealed this to be spatial inhomogeneous with a non neglectable intensity – especially in the outer wake region where the gradient of the wake deficit is largest – and with a length scale considerable less than the one characterizing the ambient atmospheric turbulence.

Whereas traditional approaches for description of wake loading and wake production typically are of a fragmental character, in the sense that the focus is *either* on power production *or* on turbine (fatigue) loading, the present theory is *unifying* – describing the physical processes that takes place – and thus includes both turbine power- and load aspects. The unifying property of the new wake meandering simulation philosophy allows, contrary to traditional approaches, thus potentially for optimization of wind farm topology and wind

farm operation, or other applications where both production and loads aspects are required simultaneously as e.g. development of advanced control strategies for the individual turbine, in order to reduce the blade- and turbine fatigue loading during wake operation.

The application of the dynamic wake meandering philosophy with existing aeroelatistic codes is straight forward and does not involve any code modifications. The strategy is simply to embed the combined effect of atmospheric turbulence, added wake turbulence and the intermittent “turbulence contribution”, caused by wake meandering, in files replacing the traditional turbulence file input to aeroelastic computations. In a future perspective, the present wake meandering description will be extended to allow for mutual interaction of two or more wakes, and the added wake turbulence will be characterized in more details.

5 Publications and references

The project has resulted in a considerable number of publications. These are listed below – organized in subsections reflecting type of publication. The "residual" references, which can not be attributed to the reported project, are listed in a separate final subsection.

5.1 Journal contributions

[1] Larsen, G.C., Madsen, H. Aa., Thomsen, K. and Larsen, T.J.. Wake meandering - a pragmatic approach. Part 1: Theory. Submitted for publication in Wind Energy.

[2] Larsen, G.C., Madsen, H. Aa., Thomsen, K. and Larsen, T.J.. Wake meandering - a pragmatic approach. Part 2: Verification. Submitted for publication in Wind Energy.

[3] Thomsen, K., Madsen, H.A. (2005). A New Simulation Method for Turbine in Wakes – Applied to Extreme Response during Operation. Wind Energy, 8, pp. 35-47.

[4] Okulov, V.L., Naumov, I. and Sørensen, J.N. (2006). Vortex Triplet. Doklady Physics, vol. 51, pp. 333-337.

[5] Okulov, V.L. and Sørensen, J.N. (2007). Stability of helical tip vortices in a rotor far wake. Journal of Fluid Mechanics, vol. 576, pp. 1-25.

[6] Okulov, V.L. and Sørensen, J.N. (2004). Instability of a Vortex Wake behind Wind Turbines. Doklady Physics, vol. 49, no. 12, pp. 772-777.

[7] Okulov, V.L. and Sørensen, J.N. (2007). Stability analysis of the far wake model of Joukowski. Submitted for publication in AIAA Journal.

5.2 Conference contributions

[8] Madsen, H.A., Larsen, G.C., and Thomsen, K. (2005). Wake flow charateristics in low ambient turbulence conditions. In: proceedings of Copenhagen Offshore Wind.

[9] Larsen, G.C., Madsen, H.Aa., Thomsen, K., Larsen, T.J. (2006). Wake meandering - a pragmatic approach. International Energy Agency, Annex XXIII: Workshop on wake modelling and benchmarking of models, Billund (DK), 6-7 September. Unpublished.

[10] Mann, J.; Bingöl, F., Jørgensen, H.E., Mikkelsen, T., Larsen, G.C., Coffey, A., Harris, M. (2006). Fast laser Doppler wake measurements. In: Proceedings (online). European Wind Energy Conference and Exhibition, Athens (GR), 27 February - 2 Marts. (European Wind Energy Association, Brussels) 1 p.

[11] Mann, J., Bingöl, F., Larsen, G.C. (2006). Laser Doppler scanning of a wind turbine wake. EGU General Assembly 2006, Vienna (AT), 2-7 April. Geophys. Res. Abstr. (CD-ROM) **8** (no.Abstr. EGU06-A-06888).

[12] Sørensen, J.N. and Okulov, V.L. (2005). Modeling of Far Wake Behind Wind Turbine. In: Wind energy. Proceedings of the Euromech colloquium. EUROMECH colloquium 464b: Wind energy. International colloquium on fluid mechanics and mechanics of wind energy conversion, Oldenburg (DE), 4-7

October. Peinke, J.; Schaumann, P.; Barth, S. (eds.), (Springer, Berlin, 2006) p. 245-248.

[13] Okulov, V.L. and Sørensen, J.N. (2005). Stability of Tip Vortex Equilibrium in Far Wake Behind Wind Turbine. In: Wind energy. Proceedings of the Euromech colloquium. EUROMECH colloquium 464b: Wind energy. International colloquium on fluid mechanics and mechanics of wind energy conversion, Oldenburg (DE), 4-7 October. Peinke, J.; Schaumann, P.; Barth, S. (eds.), (Springer, Berlin, 2006) p. 249-252.

[14] Bingöl, F., Mann, J. and Larsen, G.C. (2007). Laser measurements of wake dynamics. To appear in the proceedings of EWEC, Milan, Italy.

[15] Bingöl, F., Larsen, G.C. and Mann, J. (2007). Wake meandering – an analysis of instantaneous 2-D laser measurements.. To appear in the proceedings of The Second Conference on The Science of making Torque from Wind. 28-31 August, Technical University of Denmark.

[16] Madsen, H.Aa., Larsen, G.C. and Thomsen, K. (2005). Wake flow characteristics in low ambient turbulence conditions. In: Proceedings (CD-ROM). Copenhagen Offshore Wind Conference, Copenhagen (DK), 25-28 September. 10 p.

[17] Ivanell, S., Sørensen, J.N. and Henningson, D. (2006). Numerical Computations of Wind Turbine Wakes. In: Peinke, Schaumann and Barth (Eds.), Proc. of the Euromech Colloquium Wind Energy, Springer, pp. 259-263.

[18] Troldborg, N., Sørensen, J.N. and Mikkelsen, R. (2006). Numerical Simulations of Wakes of Wind Turbines in Wind Farms, EWEC-2006, European Wind Energy Conference, Athens, Greece, 27 February - 2 March.

[19] Sørensen, J.N., Mikkelsen, R. and Troldborg, N. (2007). Simulation and Modeling of Turbulence in Wind Farms. To be presented at the EWEC conference, Milan, May 7-11, 10 pages.

[20] Sørensen, J.N. and Okulov, V.L. (2005). Modeling of the Far Wake Behind Wind Turbine. To appear in Proc. IEA Symposium on the Aerodynamics of Wind Turbines, Athens.

[21] Okulov, V.L. and Sørensen, J.N. (2004). Instability of the Far Wake behind a Wind Turbine. Proc. 21th ICTAM-2004, Warsaw, Poland (http://ictam04.ippt.gov.pl/).

[22] Mann, J., Bingöl, F., Courtney, M., Antonio, I., Larsen, G.C., Mikkelsen, T., Dellwik, E., and Jørgensen, H. (2007). Lidars in Wind Energy. 14th Coherent Laser radar Conference (CLRC), Snowmass, Colorado.

[23] Antoniou, I., Courtney, M., Peña, A., Hasager, C., Bingöl, F., Mann, J., Larsen, G.C., Mikkelsen, T., Jørgensen, H.E., and Petersen, S.M. (2007). Remote sensing measurements for wind energy purposes. Dansk Vindkraftkonference, 25-27 April.

5.3 Reports

[24] Thomsen, K., Madsen, H.Aa., Larsen, G.C., Larsen, T.J. (2006). A simplified approach for simulation of wake meandering. Resultatblad AED-RB-18(EN), 6 p.

[25] Larsen, G.C., Madsen, H.Aa., Bingöl, F., Mann, J., Ott, S., Sørensen, J.N., Okulov, V., Troldborg, N., Mikkelsen, R., Nielsen, M., Thomsen, K., and Larsen, T.J. (2007). Dynamic Wake Meandering Modeling. Risø-R-1607(EN).

[26] Pedersen, B.J. (2007). EFP-2004, Dynamisk wakemodel til detaljeret aeroelastisk simulering af møller i parker – Work and conclusions made by Vestas. Vestas document.

[27] Ott, S. (2007). A vorticity based approach to wind turbine wake modelling. Risø-R-1618(EN).

5.4 Other references

[28] Madsen, H.A. Kobling af HawC til 3D actuator disc model (1999). Chapter 5 in report Risø-R-1129(DA) edited by Helge Aagaard Madsen, Forskningscenter Risø, August. (In Danish).

[29] Ainslie, J.F. (1985). Development of an eddy viscosity model for wind turbine wakes. In: Proceedings of the BWEA conference 1985, pp. 61-66.

[30] Ainslie, J.F. (1986). Wake modeling and the prediction of turbulence properties. Proceedings of the 8th British Wind energy Association Conference, Cambridge 19-21 March. pp. 115-120.

[31] Ainslie, J.F. (1988). Calculating the flow field in the wake of wind turbines. Journal of Wind Engineering and Industrial Aerodynamics, 27, pp. 213-224.

[32] Madsen, H.A., Thomsen, K. and Petersen, S.M. (2003). Wind Turbine Wake Data from Inflow Measurements using a Five Hole Pitot Tube on a NM80 Wind Turbine Rotor in the Tjæreborg Wind Farm. Report Risø-I-2108(DA).

[33] Mann, J. (1994). The Spatial Structure of Neutral Atmospheric Surface-Layer Turbulence. J. of Fluid Mech., 273, 141-168.

[34] Joukowski, N.E. (1912). Vortex theory of a rowing screw. Trudy Otdeleniya Fizicheskikh Nauk Obshchestva Lubitelei Estestvoznaniya,16, 1.

[35] Okulov, V.L. (2004). On the stability of multiple helical vortices. J. Fluid Mech., vol. 521, pp. 319-342.

[36] Medici D. and Alfredsson P.H. (2004). Proc. of The Science of Making Torque from Wind, Delft, the Netherlands.

[37] Michelsen, J.A. (1992). Basis3D – A platform for development of multi-block PDE solvers. Report AFM 92-05, Dept. of Fluid Mechanics, Technical University of Denmark (DTU).

[38] Michelsen, J.A. (1994). Block structured multigrid solution of 2-D and 3-D elliptic PDE's. Report AFM 94-06, Dept. of Fluid Mechanics, Technical University of Denmark (DTU).

[39] Sørensen, N.N. (1995). General purpose flow solver applied to flow over hills. Risø-R-827(EN) ,154 p. PhD thesis, Risø.

[40] W.Z. Shen, J.A. Michelsen and J.N. Sørensen (2001). Improved Rie-Chow Interpolation for Unsteady Flow Computations, AIAA Journal, vol. 39, no. 12, pp. 2406-2409.

[41] Sørensen, J.N. and Shen, W.Z. (2002). Numerical modeling of wind turbine wakes. J Fluids Engineering, vol. 124, no. 2, pp. 393-399.

[42] Mikkelsen, R. (2003). Actuator disc methods applied to wind turbines, PhD dissertation, MEK-FM-PHD 2003-02.

[43] Øye, S. (1992). Wind turbine: Dynamic flow measurements, Department of Fluid Mechanics, Technical University of Denmark (DTU).

[44] Frandsen, S.T. (2005). Turbulence and turbulence-generated structural loading in wind turbine clusters. Risø-R-1188(EN), Risø National Laboratory, Roskilde, Denmark.

[45] Veers, P.S. (1988). Three-dimensional wind simulation. SAND88-0152, Albuqueerque, NM, Sandia National Laboratories.

[46] Berkooz, G., Holmes, P. and Lumley, J. (1993). The proper orthogonal decomposition in the analysis of turbulent flows. Annual Review of Fluid Mechanics, vol. 25, pp. 539-575.

[47] Holmes, P., Lumley, J. and Berkooz, G. (1996). Turbulence, coherent structures, dynamical systems and symmetry. Cambridge University Press, Cambridge, UK.

[48] Christensen, E.A., Brøns, M. and Sørensen, J.N. (2000). Evaluation of POD-based Decomposition Techniques Applied to Parameter-dependent Non-turbulent Flows. SIAM J. of Scientific Computing, vol. 21, no. 4, pp. 1419-1434.

[49] B.H. Jørgensen, J.N. Sørensen and M. Brøns, M. (2003). Low - dimensional Modeling of a Driven Cavity Flow with Two Free Parameters, Theoretical and Comp. Fluid Mechanics, vol. 16, no. 4, p. 299-317.

[50] F. Rasmussen, M. H. Hansen, K. Thomsen, T. J. Larsen, F. Bertagnolio, J. Johansen, H. A. Madsen, and A. M. Hansen C. Bak (2003). Present status of aeroelasticity of wind turbines. Wind Energ., 6:213–228.

[51] IEC 61400-1 Ed. 3 (2005): Wind turbines - Part 1: Design requirements. International Electrotechnical Commission.

[52] M. Shinozuka and C.-M. Jan (1972). Digital simulation of random processes and its applications. J. Sound and Vibration, 25:111–128.

[53] P. S. Veers. Three-dimensional wind simulation (1988). Technical Report SAND88–0152, Sandia National Laboratories.

[54] J. Mann (1998). Wind field simulation. Prob. Engn. Mech., 13:269–282.

[55] J. Mann (1999). Modelling of the spectral velocity tensor in complex terrain. In: A. Larsen, G. L. Larose, and F. M. Livesey, editors, Wind engineering into the 21st century, pages 257–264. Balkema.

[56] J. Mann, B. H. Jørgensen S. Ott, and H. Frank (2002). WAsP Engineering 2000. Technical Report Risø–R–1356(EN), Risø National Laboratory.

[57] S. R. Winterstein (1988). Nonlinear vibration models for extremes and fatigue. J. Engng. Mech. ASCE, 114:1772–1790.

[58] O. Ditlevsen, G. Mohr, and P. Hoffmeyer (1996). Integration of non-Gaussian fields. Prob. Engn. Mech., 11:15–23.

[59] M. Nielsen, G.C. Larsen, J. Mann, S. Ott, K.S. Hansen, and B.J. Pedersen (2003). Wind simulation for extreme and fatigue loads. Technical Report Risø-R-1437(EN), Risø National Laboratory.

[60] M. Grigoriu (1995). Parametric models of nonstationary gaussian processes. Prob. Engn. Mech., 10:95–102.

[61] K. Gurley and A. Kareem (1993). Gust loading factors for tension leg platforms. Appl. Ocean Res., 15:137–154.

[62] M. Nielsen, G. C. Larsen, and K. S. Hansen. Simulation of inhomogeneous, non-stationary and non-Gaussian turbulent winds, J. Phys. Conf. Ser. (submitted).

[63] M. Nielsen, P.C. Chatwin, H.E. Jørgensen, N. Mole, R.J. Munro, S. Ott (2002). Concentration fluctuations in gas releases by industrial accidents. Risø-R-1329(EN) Risø National Laboratory.

[64] Ferhat Bingöl (2005). Adapting a Doppler laser anemometer to wind energy. Master's thesis, Technical University of Denmark.

[65] I. Antoniou, H. E. Jørgensen, T. Mikkelsen, T. F. Pedersen, G. Warmbier, and D. Smith (2004). Comparison of wind speed and power curve measurements using a cup anemometer, a lidar and a sodar. European Wind Energy Conference and Exhibition, pages 47–51.

[66] Antonio, I. (2003). Wind Turbine Test, NEG Micon NM80/2750, Power Curve Measurement IEC 61400-12. Risø-I-1934(EN).

[67] Madsen, H.Aa., Thomsen, K. and Petersen, S.M. (2003). Wind Turbine Wake Data from Inflow Measurements using a Five Hole Pitot Tube on a NM80 Wind Turbine Rotor in the Tjæreborg Wind Farm. Risø-I-2108(EN).

[68] Okulov, V.L. (2004). On the stability of multiple helical vortices. J. Fluid Mech. **521**, 319-342.

[69] Gupta, B.P. and Loewy, R.G.. Theoretical analysis of the aerodynamic stability of multiple, interdigitated helical vortices (1974). AIAA Journal, Vol. **12**, No. 10, pp. 1381-1387.

[70] Levy, H. and Forsdyke, A.G. (1928). The steady motion and stability of a helical vortex. Proc. Roc. Soc. Lond. **A120**, 670-690.

[71] Widnall, S.E. (1972). The stability of helical vortex filament. J. Fluid Mech. **54**, 641 - 663.

[72] Havelock T.H. (1931). The stability of motion of rectilinear vortices in ring formation. Philos.

[73] Morikawa, G.K. and Swenson, E.V. (1971). Interacting motion of rectilinear geostrophic vortices, Phys. Fluids **14**, 1058-1073.

[74] Okulov, V.L. and Sørensen, J.N. (2004). Instability of a vortex wake behind a wind turbine Doklady Physics. **49**, 772-777.

[75] Landgrebe, A. J. (1972). The Wake geometry of a hovering rotor and its influence on rotor performance. Journal of the American Helicopter Society **17**(4), 2-15.

[76] Vermeer, L.J., Sørensen, J.N., and Crespo, A. (2003). Wind Turbine Wake Aerodynamics. Progress in Aerospace Sciences 39, 467-510.

[77] Bhagwat, M.J. and Leishman, J.G. (2000). Stability analysis of helicopter rotor wakes in axial flight. J. Am. Helicopter Ass., **45**, 165-178.

[78] Bechmann, A. (2006). Large-eddy simulation of atmospheric flow over complex terrain. Technical Report Risø-PhD-28(EN), Risø National Laboratory, Roskilde, Denmark.

[79] M. Grigoriu (2000). Non-gaussian models for stochastic mechanics. Prob. Engn. Mech., **15**, 15–23.

[80] M. Gioffrè, V. Gusella, and M. Grigoriu (2000). Simulation of non-gaussian field applied to wind pressure fluctuations. Prob. Engn. Mech., **15**, 309–389.

[81] Stock, M. J. (2002-2007): Summary of Vortex Methods Literature (a living document rife with opinion). Published via the internet.
URL: http://mark.technolope.org/research/vortex_methods_literature.pdf

[82] M. Rasetti, T. Regge (1975). Vortices in He II, current algebras and quantum knots, Physica A , **80**, 217-233.

[83] S.B. Pope (2000). Turbulent Flows. Cambridge University Press.

Risø's research is aimed at solving concrete problems in the society.

Research targets are set through continuous dialogue with business, the political system and researchers.

The effects of our research are sustainable energy supply and new technology for the health sector.